

# UNCLASSIFIED

AD NUMBER
AD877463
NEW LIMITATION CHANGE
TO Approved for public release, distribution unlimited
FROM Distribution authorized to U.S. Gov't. agencies and their contractors; Administrative/Operational Use; SEP 1970. Other requests shall be referred to Army Aviation Materiel Labs., Fort Eustis, VA 23604.
AUTHORITY
USAAMRDL ltr, 30 Jul 1971

THIS PAGE IS UNCLASSIFIED

AD 877463



USAAVLABS TECHNICAL REPORT 70-47

ANALYSIS OF MEASURED HELICOPTER ROTOR  
PRESSURE DISTRIBUTIONS

22  
CB

AD No. \_\_\_\_\_  
DDC FILE COPY

By

C. Tung  
F. A. DuWaldt

September 1970

U. S. ARMY AVIATION MATERIEL LABORATORIES  
FORT EUSTIS, VIRGINIA

CONTRACT DAAJ02-69-C-0076

CORNELL AERONAUTICAL LABORATORY, INC.  
BUFFALO, NEW YORK

This document is subject to special  
export controls, and each transmittal  
to foreign governments or foreign  
nationals may be made only with  
prior approval of U.S. Army Aviation  
Materiel Laboratories, Fort Eustis,  
Virginia 23064.



DDC  
DEC 10 1970  
B

96

### DISCLAIMERS

The findings in this report are not to be construed as an official Department of the Army position unless so designated by other authorized documents.

When Government drawings, specifications, or other data are used for any purpose other than in connection with a definitely related Government procurement operation, the United States Government thereby incurs no responsibility nor any obligation whatsoever; and the fact that the Government may have formulated, furnished, or in any way supplied the said drawings, specifications, or other data is not to be regarded by implications, or otherwise as in any manner licensing the holder or any other person or corporation, or conveying any rights or permission, to manufacture, use, or sell any patented invention that may in any way be related thereto.

### DISPOSITION INSTRUCTIONS

Destroy this report when no longer needed. Do not return it to the originator.

ACCESSION FOR	
CFSTI	WHITE SECTION <input type="checkbox"/>
DDC	BUFF SECTION <input checked="" type="checkbox"/>
UNANNOUNCED	<input type="checkbox"/>
JUSTIFICATION	
BY	
DISTRIBUTION/AVAILABILITY CODES	
DIST.	AVAIL. and/or SPECIAL
2	



DEPARTMENT OF THE ARMY  
HEADQUARTERS US ARMY AVIATION MATERIEL LABORATORIES  
FORT EUSTIS, VIRGINIA 23604

This report has been reviewed by the U. S. Army Aviation Materiel Laboratories and is considered to be technically sound. The report is published for the exchange of information and the stimulation of ideas.

Task 1F162204A14231  
Contract DAAJ02-69-C-0076  
USAAVLABS Technical Report 70-47  
September 1970

**ANALYSIS OF MEASURED HELICOPTER ROTOR  
PRESSURE DISTRIBUTIONS**

**Final Report**

**Cornell Aeronautical Laboratory, Inc. Report No. BB-2803-S-1**

**By  
C. Tung & F.A. DuWaldt**

**Prepared by  
Cornell Aeronautical Laboratory, Inc.  
Buffalo, New York**

**for  
U.S. ARMY AVIATION MATERIEL LABORATORIES  
FORT EUSTIS, VIRGINIA**

This document is subject to special export controls, and each transmittal to foreign governments or foreign nationals may be made only with prior approval of U.S. Army Aviation Materiel Laboratories, Fort Eustis, Virginia 23604.

## SUMMARY

The purpose of this research was to determine a rational basis for interpretation of the aerodynamic force characteristics of helicopter rotors. The approach consisted of three elements. The first was the parallel development of series expressions for: flight measurements of rotor differential pressure distributions; corresponding two-dimensional wind-tunnel pressure distributions for the same airfoil geometry; and theoretical pressure distributions for the two-dimensional airfoil. Second, there was a comparison between pressure differential distribution components determined from flight measurements and pressure distribution components computed by an approximate, unsteady, three-dimensional theory developed previously at CAL for the U. S. Army. Third, the sensitivity of the airfoil drag characteristics to variations in the pressure differential distributions was investigated on the basis of two-dimensional steady boundary layer theory.

The fundamental technique employed was a curve-fitting process based on an expansion of the pressure distributions in terms of Glauert coefficients. Available flight measurements of pressure distributions for the UH-1A rotor at advance ratios of  $\mu = 0$ ,  $\mu = 0.08$ , and  $\mu = 0.26$ , and the H-34 rotor at advance ratios of  $\mu = 0.18$  and  $\mu = 0.29$  were used in the analyses. Corresponding wind-tunnel measurements on two-dimensional NACA 0015 and 0012 airfoils were also reduced to Glauert form. There is only one coefficient in the theoretical representation of the differential pressures because these two-dimensional airfoils are symmetrical. Induced camber effects arising in the available finite span theory were much smaller than the values deduced from measured blade pressure differentials.

Glauert coefficients derived from the measured rotor pressure differentials had many of the characteristics of the Glauert coefficients derived from measured two-dimensional pressure distributions. They also differed, partly because of the lack of a good quantitative measure of angle of attack (which greatly influences the viscous effects). It was found that the viscous effects evident in the two-dimensional data could also be seen in the rotor data. It is postulated that these viscous effects probably account for a large part of the differences observed between the theoretical predictions and experimental measurements of the rotor pressure differential components.

Calculated drag coefficient distributions (based on differential pressure measurements) exhibited a characteristic rise on the retreating side of the rotor disk.

## FOREWORD

The technical effort reported herein was conducted at Cornell Aeronautical Laboratory, Inc., during the period April 1969 to April 1970. Dr. Chee Tung was the project engineer. The program was sponsored by the U.S. Army Aviation Materiel Laboratories and was administered by Messrs. John Shipley and William Yeager. The authority for this effort was Task 1F162204A14231.

**BLANK PAGE**



## TABLE OF CONTENTS

	<u>Page</u>
SUMMARY. . . . .	iii
FOREWORD . . . . .	v
LIST OF ILLUSTRATIONS . . . . .	ix
LIST OF TABLES . . . . .	xii
LIST OF SYMBOLS. . . . .	.xiii
INTRODUCTION . . . . .	1
STATIC ANALYSIS OF PRESSURE DISTRIBUTIONS . . . . .	3
Theoretical Two-Dimensional Pressure Distributions . . . . .	3
Measured Two-Dimensional Pressure Distributions (Wind Tunnel Data for NACA 0012 and NACA 0015 Airfoils). . . . .	6
Measured Rotor Pressure Distributions (Flight Data for H-34 With NACA 0012 Airfoil and UH-1A With NACA 0015 Airfoil). . . . .	9
DYNAMIC ANALYSIS OF PRESSURE DISTRIBUTIONS . . . . .	13
Theoretical Unsteady Rotor Pressure Distributions . . . . .	13
Measured Rotor Pressure Distributions. . . . .	13
COMPARISON AND DISCUSSION OF PRESSURE DISTRIBUTION COMPONENTS. . . . .	16
SERIES REPRESENTATION OF THICKNESS EFFECTS. . . . .	25
Theoretical Values. . . . .	25
Comparison of Theoretical and Experimental Results of Thickness Effects . . . . .	26
PROFILE DRAG ESTIMATES . . . . .	27
Theoretical Analysis . . . . .	27
Comparison of Theoretical and Experimental Results for Two-Dimensional Cases. . . . .	29
Estimates of Rotor Profile Drag Distributions . . . . .	30

## TABLE OF CONTENTS

	<u>Page</u>
CONCLUSIONS. . . . .	31
RECOMMENDATIONS . . . . .	33
LITERATURE CITED. . . . .	34
APPENDIXES	
I. Least-Square Polynomial Approximation . . . . .	76
II. Governing Equations for $\hat{A}_i' \Delta$ . . . . .	79
DISTRIBUTION . . . . .	81

## LIST OF ILLUSTRATIONS

<u>Figure</u>		<u>Page</u>
1	Airfoil Chord Position Representation in Cartesian and Polar Coordinates. . . . .	49
2	Coordinates for Airfoil With a Flap. . . . .	49
3	Comparison of Experimental Pressure Distributions (Reference 4) With Theoretical Results at Mach Numbers 0.3 and 0.4 to Illustrate Thickness Effects. . . . .	50
4	Comparison of Experimental Pressure Distributions (Reference 4) With Theoretical Results at Mach Numbers 0.5 and 0.6 to Illustrate Thickness Effects. . . . .	51
5	Schematic of Upper and Lower Bounds for Measured Pressure Differentials . . . . .	52
6	Effects of Number, $n$ , of Glauert Coefficients on The Difference Between Computed and Measured Pressures for UH-1A Flight Data at $\mu = 0$ , $r/R = 0.85$ , and $\psi = 0$ . . . . .	53
7	Comparison of Theoretical Nondimensional Glauert Coefficients With Flight Data for H-34 at $\mu = 0.18$ , $r/R = 0.40$ . . . . .	54
8	Comparison of Theoretical Nondimensional Glauert Coefficients With Flight Data for H-34 at $\mu = 0.18$ , $r/R = 0.85$ . . . . .	55
9	Comparison of Theoretical Nondimensional Glauert Coefficients With Flight Data for H-34 at $\mu = 0.18$ , $r/R = 0.90$ . . . . .	56
10	Comparison of Theoretical Nondimensional Glauert Coefficients With Flight Data for H-34 at $\mu = 0.29$ , $r/R = 0.40$ . . . . .	57
11	Comparison of Theoretical Nondimensional Glauert Coefficients With Flight Data for H-34 at $\mu = 0.29$ , $r/R = 0.85$ . . . . .	58
12	Comparison of Theoretical Nondimensional Glauert Coefficients With Flight Data for H-34 at $\mu = 0.29$ , $r/R = 0.90$ . . . . .	59

# LIST OF ILLUSTRATIONS (Cont'd)

<u>Figure</u>		<u>Page</u>
13	Comparison of Theoretical Nondimensional Glauert Coefficients With Flight Data for UH-1A at $\mu = 0.08$ , $r/R = 0.40$ . . . . .	60
14	Comparison of Theoretical Nondimensional Glauert Coefficients With Flight Data for UH-1A at $\mu = 0.08$ , $r/R = 0.85$ . . . . .	61
15	Comparison of Theoretical Nondimensional Glauert Coefficients With Flight Data for UH-1A at $\mu = 0.08$ , $r/R = 0.90$ . . . . .	62
16	Comparison of Theoretical Nondimensional Glauert Coefficients With Flight Data for UH-1A at $\mu = 0.26$ , $r/R = 0.40$ . . . . .	63
17	Comparison of Theoretical Nondimensional Glauert Coefficients With Flight Data for UH-1A at $\mu = 0.26$ , $r/R = 0.85$ . . . . .	64
18	Comparison of Theoretical Nondimensional Glauert Coefficients With Flight Data for UH-1A at $\mu = 0.26$ , $r/R = 0.90$ . . . . .	65
19	Airfoil Leading Edge Separation Characteristics (From Reference 13) . . . . .	66
20	Comparison of Measured and Calculated Drag Coefficients for NACA 0012 Airfoil Section at Mach Number 0.3 . . . . .	67
21	Comparison of Measured and Calculated Drag Coefficients for NACA 0012 Airfoil Section at Mach Number 0.4 . . . . .	68
22	Comparison of Measured and Calculated Drag Coefficients for NACA 0012 Airfoil Section at Mach Number 0.5 . . . . .	69
23	Comparison of Measured and Calculated Drag Coefficients for NACA 0012 Airfoil Section at Mach Number 0.6 . . . . .	70

# LIST OF ILLUSTRATIONS (Cont'd)

<u>Figure</u>		<u>Page</u>
24	Comparison of Measured and Calculated Drag Coefficients for NACA 0015 Airfoil Section at Mach Number From 0.3 to 0.88 . . . . .	71
25	Variation of Calculated Drag Coefficients With Azimuthal Angle $\psi$ for H-34 at $r/R = 0.40$ , $\mu = 0.18$ and $0.29$ . . . . .	72
26	Variation of Calculated Drag Coefficients With Azimuthal Angle $\psi$ for H-34 at $r/R = 0.85$ and $0.90$ , $\mu = 0.18$ and $0.29$ . . . . .	73
27	Variation of Calculated Drag Coefficients With Azimuthal Angle $\psi$ for UH-1A at $r/R = 0.40$ , and $\mu = 0.0, 0.08$ , and $0.26$ . . . . .	74
28	Variation of Calculated Drag Coefficients With Azimuthal Angle $\psi$ for UH-1A at $r/R = 0.85$ and $0.90$ and $\mu = 0.0, 0.08$ , and $0.26$ . . . . .	75

# LIST OF TABLES

<u>Table</u>		<u>Page</u>
I	Theoretical Glauert Coefficients for NACA 0012 Airfoil (Compressibility Included). . . . .	36
II	Theoretical Glauert Coefficients for NACA 0012 Airfoil With Trailing Edge Flap (Negative Three Degrees Flap Angle). . . . .	37
III	Theoretical Glauert Coefficients for NACA 0015 Airfoil. . . . .	38
IV	First Three Glauert Coefficients, $A_0$ , $A_1$ , $A_2$ , Obtained From Measured Pressure Differentials on NACA 0012 Airfoil Section. . . . .	39
V	First Three Nondimensional Glauert Coefficients, $\bar{A}_0$ , $\bar{A}_1$ , $\bar{A}_2$ , Obtained From Measured Pressure Differentials on NACA 0012 Airfoil Section . . . . .	40
VI	First Three Glauert Coefficients, $A_0$ , $A_1$ , $A_2$ , Obtained From Measured Pressure Differentials On NACA 0012 Airfoil Section With Trailing Edge Flap (Three Degrees Flap Angle) . . . . .	41
VII	First Three Nondimensional Glauert Coefficients, $\bar{A}_0$ , $\bar{A}_1$ , $\bar{A}_2$ , Obtained From Measured Pressure Differentials on NACA 0012 Airfoil Section With Trailing Edge Flap (Three Degrees Flap Angle). . . . .	42
VIII	First Three Glauert Coefficients, $A_0$ , $A_1$ , $A_2$ And $\bar{A}_0$ , $\bar{A}_1$ , $\bar{A}_2$ , Obtained From Measured Pressure Differentials on NACA 0015 Section . . . . .	43
IX	First Three Nondimensional Glauert Coefficients, $\bar{C}_0$ , $\bar{C}_1$ , $\bar{C}_2$ , Obtained From H-34 Flight Data (0012 Airfoil Section) . . . . .	46
X	First Three Nondimensional Glauert Coefficients, $\bar{C}_0$ , $\bar{C}_1$ , $\bar{C}_2$ , Obtained From UH-1A Flight Data (0015 Airfoil Section) . . . . .	47

## LIST OF SYMBOLS

$A_n$	Unsteady Glauert coefficients (see Equation (1))
$\bar{A}_n$	Nondimensional unsteady Glauert coefficients, $A_n/(A_0 + \frac{1}{2}A_1)$
$b$	Blade semichord, ft
$\bar{b}$	$b/R$
$C_L$	Lift coefficient of airfoil
$C'_L$	Lift coefficient of airfoil with deflected flap
$C_n$	Steady Glauert coefficients (see Equation (12))
$\bar{C}_n$	Nondimensional steady Glauert coefficients, $C_n/(C_0 + \frac{1}{2}C_1)$
$K$	Total number of differential pressure taps
$L$	Blade section lift per span, lb/ft
$L'$	Lift on airfoil with deflected flap, lb/ft
$\ell$	Airfoil leading edge radius/chord
$M$	Blade section pitching moment about midchord, ft/lb
$M_\infty$	Free-stream Mach number
$\Delta p$	Pressure differentials, lb/ft <sup>2</sup>
$\Delta p'$	Pressure differentials computed by Glauert coefficients, lb/ft <sup>2</sup>
$R$	Total blade radius, ft
$R_\ell$	Reynolds number based on airfoil leading edge radius
$R_c$	Reynolds number based on airfoil chord
$r$	Radius to a blade section, ft
$\bar{r}$	$r/R$
$t$	Time, sec
$V_\infty$	Free-stream velocity, ft/sec

LIST OF SYMBOLS (Cont'd)

$w(\chi)$	Weighting function
$\chi$	Chordwise coordinate (positive aft), ft
$y_c$	Camber line distance from chord line, ft
$\alpha$	Angle of attack, deg
$\Gamma$	Total bound vorticity of blade section, ft <sup>2</sup> /sec
$\gamma(\theta, t)$	Chordwise bound vorticity distribution, ft/sec
$\epsilon_{rms}$	Root mean square
$\eta$	The transformed angular position through which the airfoil trailing edge tab is rotated (see Figure 2)
$\theta$	Secondary chordwise coordinate defined by $\chi = -b \cos \theta$
$\mu$	Advance ratio
$\xi$	Angle of deflected trailing edge tabs (positive downward)
$\rho$	Air density, slugs/ft <sup>3</sup>
$\psi$	Azimuth angle, deg
$\omega$	Blade rotational speed, rad/sec



## INTRODUCTION

Expansion of the flight envelope of the helicopter (and of aircraft that are helicopter derivatives) is proceeding at a rapid rate. Nearly all the performance gain, however, has come about through the application of additional power or through configurational changes that minimize the role of the rotor in the high-speed flight range. Dynamic problems (fatigue of rotating components, shaking forces transmitted to the fuselage, etc.) remain. Concurrent with this performance growth have been research efforts devoted to aerodynamic models which retain some part of the rotor wake effects and blade dynamic motion effects on air loadings. However, both performance predictions and blade dynamic response predictions still are based largely on some empirical representation of local airfoil characteristics; in fact, measured two-dimensional section characteristics are often assigned. It is generally believed that the use of two-dimensional airfoil characteristics can introduce sizable errors in the estimation of rotor performance--particularly in the estimate of the power required. Consequently, empirical correction factors derived from performance tests are incorporated.

In recognition of these deficiencies of knowledge, the U. S. Army Aviation Materiel Laboratories (USAAVLABS) initiated a coordinated experimental and theoretical research program on helicopter blade loads (and stresses) several years ago. In-flight measurement of chordwise time-varying blade pressure distributions (using the H-34 and UH-1A) was the major experimental effort; Cornell Aeronautical Laboratory, Inc., (CAL) participated in the overall program as a contractor developing theoretical prediction techniques. A major advance was made in that accurate data were accumulated, and good agreement was obtained between measured and theoretical time histories of section lift (References 1 and 2).

Initially, emphasis in the measurement program was placed on the rotor-blade lift distribution; pressure tap locations and data reduction methods were specifically tailored to minimize the errors in the lift determination. No attempt was made to obtain the aerodynamic pitching moments from the experimental data and, of course, no direct indication of section drag was obtained. Extraction of additional information from the available measured differential pressure distributions was the intent of the effort reported herein.

The specific purposes of the present research are (1) to test in detail the current assumption that the rotor-blade sections experience pressure distributions similar to those measured on an isolated two-dimensional airfoil, with the same cross section, in a steady wind stream; (2) to compare the components of the measured pressure distribution with those predicted by the most refined rotor-blade aerodynamic theory which is readily available; and (3) to estimate the profile drag of rotor-blade elements from the measured differential pressures on rotor-blade sections.

The measurements are used in conjunction with available theoretical techniques to achieve the goals listed above. The central technique is the decomposition of the pressure distribution into components so that quantitative comparisons can be made, for example, between flight measurements on blades and two-dimensional wind-tunnel data. Pressure measurements also were used to estimate local velocity components and these, in turn, were employed to estimate profile drag. Drag is the performance quantity that is most sensitive to the details of the pressure distribution. It must be admitted that the present attack is speculative in the sense that the data available are limited and that one of the items of great interest, the drag, was not measured directly in the rotor blade tests.

There are limitations on the information that can be derived from the measured rotor pressure differentials. For example, the Reynolds numbers and Mach numbers are not independent, these being related to the radial position of the section on the blade. Certain flow phenomena are practically inseparable with respect to their effects on the differential pressure distribution. For example, the induced velocity distribution, compressibility effects, angle of attack, structural distortion, and the distortion of the flow about the blade section due to boundary-layer growth can all affect one or more of the pressure distribution components in the same way and it would, indeed, be difficult to separate these effects.

The discussions that follow are presented in the context of incompressible flow. However, a simple Prandtl-Glauert transformation is introduced where necessary to correct for compressibility. Such a correction (for the static case in which the geometry of the surface is fixed) merely scales all the terms of the pressure distribution expansion by  $(1 - M_\infty^2)^{-1/2}$ .

The accuracy of the experimental data, and the limitation imposed by the number of points at which the differential pressures were measured, influence the accuracy that can be obtained in the decomposition of the pressure differentials. Care has been exercised in an attempt to avoid the assignment of significance to fictitious pressure distribution components. An error analysis was made to determine at what point the experimental errors can introduce a distorted view of the components of the pressure distribution.

The above reservations do not invalidate the present approach. They have been introduced since many of these factors reflect the difficulties inherent in obtaining the measurement per se rather than a lack of understanding of the underlying physical phenomena. Some aspects, however, are still beyond the state of the art; e.g., treatment of dynamic stall and compressibility effects in regions of strong spanwise pressure gradients.

## STATIC ANALYSIS OF PRESSURE DISTRIBUTIONS

### THEORETICAL TWO-DIMENSIONAL PRESSURE DISTRIBUTIONS

In linearized two-dimensional airfoil theory, the pressure distributions due to thickness, angle of attack, and camber can be calculated separately. The lift and the moment arise only from angle of attack and camber because the pressures on the upper and lower surfaces due to the thickness cancel. The relationships between the circulation, lift, moment, angle of attack, and camber effects will be expressed in terms of so-called "Glauert Series" (Reference 3).

Let the airfoil reference chord be located on an axis designated the  $\chi$ -axis, with the leading edge at  $-b$  and the trailing edge at  $+b$ , where  $b$  is the half chord. Let  $\chi = -b \cos \theta$  (Figure 2); then the local bound vorticity strength,  $\gamma(\theta, t)$ , can be expressed in the Glauert Series as

$$\gamma(\theta, t) = 2 \left[ A_0(t) \cot \frac{\theta}{2} + \sum_{n=1}^{\infty} A_n(t) \sin n\theta \right] \quad (1)$$

where, in general, the coefficients are functions of time, and the steady two-dimensional airfoil problem is a special case. The total circulation on the airfoil is given by

$$\Gamma = \int_{-b}^b \gamma(\chi, t) d\chi \quad (2)$$

Thus,

$$\Gamma = 2\pi v \left( A_0 + \frac{1}{2} A_1 \right) \quad (3)$$

The chordwise distribution of the pressure difference is given by the following form of the linearized Bernoulli equation for unsteady flow:

$$\Delta p(\chi, t) = \rho \left[ V_\infty \gamma(\chi, t) + \frac{\partial}{\partial t} \int_{-b}^{\chi} \gamma(\xi, t) d\xi \right] \quad (4)$$

where  $\rho$  = air density,  $V_\infty$  = free-stream velocity at infinity. The pressure differential can be expressed in terms of the Glauert coefficients by substituting (1) into (4). This result is

$$\begin{aligned} \Delta p(\theta, t) = & 2 \rho V_\infty \left[ A_0 \cot \frac{\theta}{2} + \sum_{n=1}^{\infty} A_n \sin n \theta \right] \\ & + 2 \rho b \frac{\partial}{\partial t} \left[ \left( A_0 + \frac{1}{2} A_1 \right) \theta + \left( A_0 + \frac{1}{2} A_2 \right) \sin \theta \right. \\ & \left. + \frac{1}{2} \sum_{n=2}^{\infty} \frac{1}{n} (-A_{n-1} + A_{n+1}) \sin n \theta \right] \end{aligned} \quad (5)$$

The airfoil unsteady lift and pitching moment about the midchord per unit span can also be expressed in terms of Glauert coefficients by the substitution of (5) into the following expressions:

$$L = \int_{-b}^b \Delta p(x) dx$$

$$M = - \int_{-b}^b x \Delta p(x) dx$$

Thus,

$$L = 2 \pi b \rho V_\infty \left[ A_0 + \frac{1}{2} A_1 + \frac{b}{2 V_\infty} \frac{\partial}{\partial t} (3 A_0 + A_1 + \frac{1}{2} A_2) \right] \quad (6)$$

$$M = \pi \rho b^2 V_\infty \left[ A_0 + \frac{1}{2} A_2 - \frac{b}{2 V_\infty} \frac{\partial}{\partial t} \left( A_0 + \frac{3}{4} A_1 - \frac{1}{4} A_3 \right) \right] \quad (7)$$

It is observed that the lift depends only on  $A_0$  and  $A_1$  for the steady case and on  $A_0$ ,  $A_1$ , and  $A_2$  for the unsteady case. The moment depends on  $A_0$  and  $A_2$  for the steady case and  $A_0$ ,  $A_1$ ,  $A_2$ , and  $A_3$  for the unsteady case. The physical meaning of  $A_0$  and  $A_1$  in thin airfoil theory is that the lift contribution from the  $A_0$  term is equivalent to the lift of a flat plate at a given angle of attack, and the  $A_1$  term is equivalent to the lift due to camber where the camber line chord is at zero angle of attack.  $A_2$  corresponds to the pitching moment at zero angle of attack.

It has been shown in Reference 3 that the steady Glauert coefficients  $A_i$  are related to the camber line function  $y_c$  and angle

of attack  $\alpha$ , i. e.,

$$A_o = \alpha + \frac{1}{\pi} \int_0^\pi \frac{dy_c}{dz} d\theta \quad (8)$$

$$A_n = \frac{2}{\pi} \int_0^\pi \frac{dy_c}{dz} \cos n\theta d\theta \quad (9)$$

The effect of the presence of any deflected trailing edge tabs (Figure 2) has also been shown to be (Reference 3)

$$C_L' = C_L + 2\xi(\eta + \sin \eta) \quad (10)$$

where

$$C_L' = \frac{L'}{\frac{1}{2} \rho V_1^2 (2b)} \quad C_L = \frac{L}{\frac{1}{2} \rho V_1^2 (2b)}$$

$\xi$  = angle of deflected trailing edge tabs  
(positive downward)

$\eta$  = the transformed angular position through  
which the tab is rotated.

Equation (10) may be rearranged as

$$C_L' = 2\pi \left( A_o' + \frac{1}{2} A_1' \right) \quad (11)$$

with

$$A_o' = \alpha + \frac{\xi \eta}{\pi}$$

$$A_1' = \frac{2\xi \sin \eta}{\pi}$$

To take into account the compressibility of the air, a simple Prandtl-Glauert transformation can be introduced. Such a correction, for the steady case in which the geometry of the surface is fixed, merely scales all the terms of the pressure distribution by  $1/\sqrt{1-M_\infty^2}$  where  $M_\infty$  is the

Mach number in the free-stream. This transformation will not hold for the unsteady case.

The linearized theory predicts an infinite pressure differential at the leading edge of a flat plate of zero thickness. It can be seen in Equation (5) that as  $\theta$  approaches zero (the leading edge), the first term in the Glauert series approaches infinity. This reflects the inability of the linearized theory to describe the large flow angle change (almost  $360^\circ$ ) at the leading edge of a sharp flat plate (leading edge radius = 0). The NACA 0012 and 0015 airfoils have finite leading edge radii and finite pressure differentials.

Based on the above discussions, the steady Glauert coefficients for the NACA 0012 (Reference 4) and 0015 (Reference 5) airfoils may be computed by using Equations (8), (9), and (11). It is noticed that the NACA 0012 and 0015 airfoils are symmetric and, therefore, the camber line function  $y_c = 0$ . Table I shows the leading coefficient  $A_0$  in the Glauert series for the NACA 0012 airfoil at various angles of attack. Table II shows both  $A_0$  and  $A_1$  for the same airfoil as Table I but with 3 degrees of flap deflection upward at trailing edge. The  $A_0$ 's for the NACA 0015 airfoil at different angles of attack are tabulated in Table III. The effects of compressibility and finite leading edge radius are included in all the tables. The analyses in References 6 and 7 were used to calculate the effects of thickness, finite leading edge radius, and finite trailing edge angle. Zero angle of attack data are shown on Figures 3 and 4 and are discussed in a later section.

#### MEASURED TWO-DIMENSIONAL PRESSURE DIFFERENTIALS (WIND-TUNNEL DATA FOR NACA 0012 AND NACA 0015 AIRFOILS)

The two-dimensional pressure differential measurements for NACA 0012 and 0015 airfoils in a wind tunnel are reported in References 4 and 5, respectively. The ranges of angle of attack and Mach numbers are indicated in Tables I, II, and III. Locations (in percent chord) of the pressure taps aft of the leading edge are tabulated below.

##### NACA 0012 AIRFOIL (REFERENCE 4)

TAP NO.	1	2	3	4	5	6	7	8	9	10	11	12	13	14
POSITION x/c	0.008	0.017	0.043	0.065	0.090	0.130	0.108	0.233	0.335	0.500	0.625	0.769	0.915	0.960

##### NACA 0015 AIRFOIL (REFERENCE 5)

TAP NO.	1	2	3	4	5	6	7	8	9	10	11	12	13	14	15	16
POSITION x/c	0.025	0.05	0.10	0.15	0.20	0.25	0.30	0.35	0.40	0.45	0.50	0.55	0.60	0.70	0.80	0.90

Extraction of the Glauert coefficients from the measurements by means of Equation (5) is subject to limitations such as the following:

1. With a finite number of pressure taps along the chord of the airfoil section, it is impossible to calculate all the Glauert coefficients in Equation (1). The series must be truncated at some finite number,  $N$ , less than or equal to the number of taps.
2. The accuracy of the experimental results and the numerical errors in the procedure for computing the Glauert coefficients should be considered.

It may be reasonable to determine the accuracy of the reading at each pressure tap or the possible percentage error of that tap. Then, the number,  $N$ , of terms to be retained in the series can be determined such that the contribution due to the  $(N+1)^{th}$  term in the Glauert series at a given pressure tap is within the probable error. In other words, the upper and lower bound can be established for each pressure tap depending on the possible percentage error. From the experimental results, a pressure differential curve can be drawn from the readings of the pressure taps along with the upper and lower bounds of this pressure differential curve (see Figure 5). The number  $N$  will be determined in such a fashion that the first  $N$  terms of the Glauert series lie between the curves of the upper and lower bounds.

Unfortunately, the problem of accuracy for each pressure tap has not been discussed in References 4 and 5. However, the pressure differentials at each chordwise location measured at zero angle of attack will provide useful information on the accuracy; for example, see the experimental data given by the first table on page 62 of Reference 5. Theoretically, if the pressure tap measurements on the upper and lower surfaces are all perfect, the measured pressure differentials should be equal to zero at zero angle of attack since the NACA 0015 airfoil is symmetric. The values of the pressure differences provide an estimate of the experimental accuracy. The concept of a so-called "root mean square value" may be borrowed from numerical analysis to define the accuracy instead of the possible percentage error. The concept of possible percentage error will be discussed in detail in the next section.

The root mean square value is defined as

$$\epsilon_{rms} \equiv \sqrt{\frac{\sum_{i=1}^K (\Delta p_i)^2}{K}}$$

where  $\Delta p_i$  is the  $i^{\text{th}}$  pressure differential measured at zero angle of attack, and  $K$  is the total number of differential pressure taps.

The root mean square values for References 4 and 5 at different Mach numbers are tabulated respectively as follows:

NACA 0012 AIRFOIL (REFERENCE 4)

MACH NO.	0.30	0.40	0.50	0.60	0.65	0.70	0.75	0.80
$\epsilon_{rms}$	0.054	0.055	0.068	0.039	0.044	0.040	0.036	0.053

NACA 0015 AIRFOIL (REFERENCE 5)

MACH NO.	0.40	0.55	0.60	0.625	0.650	0.675	0.701	0.751	0.777	0.805	0.831
$\epsilon_{rms}$	0.020	0.030	0.041	0.031	0.040	0.042	0.048	0.058	0.063	0.096	0.090

The  $\epsilon_{rms}$  at Mach numbers other than those listed in the above table may be estimated by interpolation.

Once  $\epsilon_{rms}$  is given, it is required that the error due to numerical computation should be smaller than the given  $\epsilon_{rms}$ . In other words,

$$\epsilon'_{rms} = \sqrt{\frac{\sum_{i=1}^K (\Delta p'_i - \Delta p_i)^2}{K}} \leq \epsilon_{rms}$$

where  $\Delta p'_i$  is the  $i^{\text{th}}$  pressure differential by the Glauert series (see Equation 5).

The method selected for computing the Glauert coefficients was the "least-square polynomial approximation". This method has the advantage of using all the given information from the pressure taps and of providing the required results with a minimum effort in computation. The details of this method are given in Appendix I. The following example is given to demonstrate the method.



Airfoil type      NACA 0015  
Mach number      0.701  
Angle of attack    -2 degrees

Let  $n$  be the number of terms to be calculated in the Glauert series by the method of "least-square polynomial approximation". One obtains

$n$	5	6	7	8	9
$\epsilon'_{rms}$	0.070	0.057	0.037	0.036	0.031

to compare with  $\epsilon_{rms} = 0.0476$  (based on the pressure differentials at zero angle of attack and Mach number 0.701). The implication of this example is that if all the information of the pressure differentials is used to compute the first five coefficients in the Glauert series, the root-mean-square error between  $\Delta p'_z$  and  $\Delta p_z$  is larger than the estimated root-mean-square error due to the experimental errors. When the first seven terms are used, however, the  $\epsilon'_{rms}$  is smaller than  $\epsilon_{rms}$  as expected. Then, the computation may be stopped at  $n = 7$  for the present case, since no useful information will be provided by the extra terms. It should be pointed out that the value of  $n$  depends on  $\epsilon_{rms}$  and will be different for various  $\epsilon_{rms}$ .

The results of the numerical computation for NACA 0012 and 0015 airfoils are presented in Tables IV through VIII. Only  $A_0$ ,  $A_1$ , and  $A_2$  are presented, since lift and moment depend only on those coefficients in steady-state condition.

#### MEASURED ROTOR PRESSURE DISTRIBUTIONS (FLIGHT DATA FOR H-34 WITH NACA 0012 AIRFOIL AND UH-1A WITH NACA 0015 AIRFOIL)

The coefficients of the series representations of the measured differential pressure distributions for the H-34 rotor blade with NACA 0012 airfoil (References 8 and 9) and the UH-1A rotor blade with NACA 0015 airfoil (Reference 10) have been computed for the following cases:

	H-34	UH-1A
ADVANCE RATIO $\mu$	0.18, 0.29	0.0, 0.08, 0.26
RADIAL STATION $\bar{r}$	0.40, 0.85, 0.90	0.40, 0.85, 0.90
AZIMUTHAL ANGLE $\psi$	0°, 30°, 60°, 90° 120°, 150°, 180°, 210° 240°, 270°, 300°, 330°	0°, 30°, 60°, 90° 120°, 150°, 180°, 210° 240°, 270°, 300°, 330°

The positions of the pressure taps along the chord of each airfoil at different radial stations are

1.  $\bar{r} = 0.40$

	TAP LOCATION, $x/c$				
(H-34)	0.042	0.158	0.300	0.600	0.910
(UH-1A)	0.040	0.170	0.340	0.630	0.880

2.  $\bar{r} = 0.85$

	TAP LOCATION, $x/c$										
(H-34)	0.017	0.040	0.090	0.130	0.168	0.233	0.335	0.500	0.625	0.769	0.915
(UH-1A)	0.020	0.040	0.090	0.130	0.170	0.230	0.340	0.630	0.770	0.900	

3.  $\bar{r} = 0.90$

	TAP LOCATION, $x/c$						
(H-34)	0.017	0.090	0.168	0.233	0.335	0.625	0.915
(UH-1A)	0.020	0.090	0.170	0.230	0.340	0.630	0.900

Since the pressure distributions are given at different radial and azimuthal stations at particular instants of time (for periodic motion which has existed for a long time), a Glauert series representation may be written as follows (compare with Equation (5)):

$$\Delta p(\theta, r_z, \psi_k) = 2\rho V_\infty(r_z, \psi_k) \left[ C_0(r_z, \psi_k) \cot \frac{\theta}{2} + \sum_{n=1}^N C_n(r_z, \psi_k) \sin n\theta \right] \quad (12)$$

where the summation is truncated according to the number  $N$  of pressure differential measurement stations, and the subscript  $l$  and  $k$  indicate the  $l^{th}$  and  $k^{th}$  position of  $r$  and  $\psi$ , respectively.

The evaluation of the accuracy in reading the oscillograph records or the pressure transducers has been discussed in References 8, 9, and 10, respectively. In References 8 and 9, the estimated accuracy of each individual data point of the poorest records is  $\pm 5$  percent with 99.7 percent confidence, i. e., 99.7 percent of points have an error less than  $\pm 5$  percent. It is stated in Reference 10 that overall errors in the tabulated data of  $\pm 5$  to  $\pm 7$  percent are to be expected, but a set of figures for pressure transducer calibration curves is also given in Reference 10. The pressure differences between measured and computed data may then be plotted to indicate the accuracy of the computed data.

When the method of "least-square polynomial approximation" is applied to compute the Glauert coefficients in Equation (12), the possible percentage errors of  $\pm 5$  percent are required for References 8 and 9, while  $\pm 5$  to  $\pm 7$  percent are required for Reference 10. An example for each case is given for demonstration.

The first case to be considered is the pressure differentials measured at  $\mu = 0.18$ ,  $\bar{r} = 0.90$ , and  $\psi = 0$  degrees (Reference 8).

$x/c$	$\Delta P$ (lb/in <sup>2</sup> )	$\Delta P'_{n=3}$	$\epsilon_{PP_e}$ (%)	$\Delta P'_{n=4}$	$\epsilon_{PP_e}$ (%)	$\Delta P'_{n=5}$	$\epsilon_{PP_e}$ (%)
0.017	7.715	7.786	0.93	7.744	0.13	7.720	0.68
0.090	3.981	3.739	6.09	3.643	3.47	3.925	1.15
0.168	2.858	2.869	3.77	2.934	2.65	2.950	3.22
0.233	2.455	2.441	0.58	2.443	0.49	2.397	2.35
0.335	1.741	1.920	10.30	1.826	4.89	1.744	1.49
0.625	0.635	0.6425	1.17	0.542	0.473	0.639	0.55
0.915	0.042	-0.515	222.61	0.103	155.24	0.0404	3.87

where  $\Delta P'_{n=3}$  = computed pressure differentials by using first  $n$  ( $= 3$ ) terms of Glauert series, and

$$\epsilon_{PP_e} = \left| \frac{\Delta p' - \Delta p}{\Delta p} \right| = \text{possible percentage error}$$

From this table, the computed pressure differentials fall inside the upper and lower bound of the measured pressure differentials when  $n = 5$ , i. e., the first five terms of the Glauert series give a representation of the measured data consistent with experimental accuracy.

The second case to be considered is the pressure differentials measured at  $\mu = 0.0$ ,  $\bar{r} = 0.85$ , and  $\psi = 0$  degrees (Reference 10). Figure 6 shows the difference between computed pressures and measured pressures for different terms. When  $n = 7$ , the errors between computed and measured pressures fall inside the curves given by  $\pm 7$  percent.

The rest of the measured pressures are treated in the same fashion to yield the first  $n$  terms of the Glauert series. The results of  $C_o/(C_o + \frac{1}{2}C_p)$ ,  $C_p/(C_o + \frac{1}{2}C_p)$ ,  $C_s/(C_o + \frac{1}{2}C_p)$  for NACA 0012 and 0015 airfoils are tabulated in Tables IX and X, respectively. The purpose of using these nondimensional forms will be discussed in the next section.

## DYNAMIC ANALYSIS OF PRESSURE DISTRIBUTIONS

### THEORETICAL UNSTEADY ROTOR PRESSURE DISTRIBUTIONS

The theoretical unsteady Glauert coefficients for the flight conditions to be considered were calculated in Reference 1. The flight conditions are: H-34 rotor blade (NACA 0012 airfoil) at  $\mu = 0.18$  and  $\mu = 0.29$ , and UH-1A rotor blade (NACA 0015 airfoil) at  $\mu = 0.08$  and  $\mu = 0.26$ . Although details of the calculations are given in the cited reference, the basic assumptions are repeated here to assist in the interpretation of the computed unsteady Glauert coefficients. They are

1. The wake configuration can be adequately prescribed.
2. The spanwise blade slopes (e.g., coning, bending), and the section angles of attack below stall are small.
3. The in-plane components of the induced velocities at the tip-path plane are small and can be neglected.
4. Below stall, the lift-curve slope is constant.
5. The blade section circulation is limited to a maximum value for angles of attack at and above stall.
6. For angles of attack above stall, the blade section's normal force is taken as the sum of the stall-limited circulatory force and a cross-flow drag force.
7. The Mach number and Reynolds number effects are assumed to influence only the lift-curve slope.
8. The interference effects of the rotor hub, fuselage, etc., are negligible.

The pressure distributions and Glauert coefficients are related through Equation (5). The computed  $\hat{A}_i$ 's are presented in Figures 7 through 18.

### MEASURED ROTOR PRESSURE DISTRIBUTIONS

The Glauert coefficients,  $C_{\lambda}$ , for the measured rotor pressure differentials have been calculated at a given set of radial and azimuthal stations from Equation (12). The  $C_{\lambda}$ 's cannot be compared directly with the  $\hat{A}_i$ 's obtained from Reference 1. However, the relationships between the  $C_{\lambda}$ 's and  $\hat{A}_i$ 's can be established. First, it is noted that the rate of change of azimuthal station is the shaft speed; i. e.,

$$\frac{d\psi}{dt} = \omega \quad (13)$$

where  $\omega$  = rotational speed of the rotor blade.

If Equation (13) is substituted into Equation (5) with the aid of the identity

$$\theta = 2 \left( \sin \theta - \frac{1}{2} \sin 2\theta + \frac{1}{3} \sin 3\theta - \dots \right) \quad \text{on } -\pi < \theta < \pi$$

Equation (5) reduces to

$$\begin{aligned} \Delta p(\theta, \psi) = & 2\rho V_1 \left( A_0 \cot \frac{\theta}{2} + \sum_{n=1}^{\infty} A_n \sin n\theta \right) \\ & + 2\rho b\omega \frac{\partial}{\partial \psi} \left[ \left( A_0 + \frac{1}{2} A_1 \right) \left( \sum_{n=1}^{\infty} \frac{2(-1)^{n+1}}{n} \sin n\theta \right) + \left( A_0 + \frac{1}{2} A_2 \right) \sin \theta \right. \\ & \left. + \sum_{n=2}^{\infty} \frac{1}{2n} (-A_{n-1} + A_{n+1}) \sin n\theta \right] \end{aligned} \quad (14)$$

If the coefficients of like trigonometric functions are collected, the following set of equations that relate the  $C_i$ 's of Equation (12) to the  $A_i$ 's of Equation (14) is obtained [by assuming  $\Delta p(\theta, t) = \Delta p(\theta, \psi_k)$  for periodic airloads].

$$C_0(\psi) = A_0(\psi)$$

$$C_1(\psi) - A_1(\psi) = \frac{\bar{b}}{\bar{r} + \mu \sin \psi} \frac{d}{d\psi} \left[ 3A_0(\psi) + A_1(\psi) + \frac{1}{2} A_2(\psi) \right] \quad (15)$$

$$C_i(\psi) - A_i(\psi) = \frac{\bar{b}}{\bar{r} + \mu \sin \psi} \frac{d}{d\psi} \left[ \frac{2(-1)^{i+1}}{i} \left( A_0 + \frac{1}{2} A_1 \right) + \frac{1}{2i} (-A_{i-1} + A_{i+1}) \right]$$

for  $i \geq 2$

where

$$\bar{b} = \frac{b}{R}$$

$$V_1 = \omega R (\bar{r} + \mu \sin \psi)$$

Once the  $C_i$ 's are given, then the  $A_i$ 's can be found by solving the set of simultaneous differential equations (Equation (15)). The solution to Equation (15) is straightforward if both  $C_i$ 's and  $A_i$ 's are expanded in Fourier series with respect to azimuthal angle  $\psi$ , i. e.,

$$C_i = C_i^0 + \sum_{n=1}^{\infty} (C_{i1}^n \sin n\psi + C_{i2}^n \cos n\psi)$$

$$A_i = A_i^0 + \sum_{n=1}^{\infty} (A_{i1}^n \sin n\psi + A_{i2}^n \cos n\psi) \quad (16)$$

The number of terms  $n$  has to be truncated at some finite limit for practical computational considerations. In the present analysis,  $n = 5$  is used since the lifts and moments are dependent on the first four Glauert coefficients ( $A_0$ ,  $A_1$ ,  $A_2$ , and  $A_3$ ). The process of substituting Equation (16) into (15) and equating the coefficients of like trigonometric functions again yields a set of algebraic equations (see Appendix II) which can be solved readily on a digital computer.\* The results for the first three  $A_i$ 's are plotted in Figures 7 through 18.

---

\*The Fourier expansion for  $C_i$ 's in  $\psi$  is a standard subroutine in programming.

## COMPARISON AND DISCUSSION OF PRESSURE DISTRIBUTION COMPONENTS

It must be recalled for purposes of this discussion that a particular method of curve fitting was used; namely, least-square fit. Furthermore, it must be noted that the function representing the pressure distributions were not all orthogonal--the angle-of-attack effect being contained in a term  $\cot \frac{\theta}{2}$ , which is not orthogonal with respect to the rest of the Glauert series terms. The important aspect of this observation is that a change of the number of points to be fit or of the number of terms to be retained can produce a new set of coefficients.\*

The Glauert coefficient comparisons that follow will be grouped in accordance with this order:

- Two-dimensional theoretical compared to two-dimensional measured coefficients; effects of viscosity
- H-34 pressure distributions as functions of spanwise station
- Comparison of H-34 data at an advance ratio of  $\mu = 0.18$  with data at  $\mu = 0.29$
- UH-1A pressure distributions as functions of spanwise station
- Comparison of UH-1A data at advance ratios of  $\mu = 0.08$  with data at  $\mu = 0.26$
- Comparison of H-34 data with UH-1A data
- Comparison of two-dimensional data with rotor blade data

### TWO-DIMENSIONAL RESULTS; EFFECTS OF VISCOSITY

Theoretical Glauert coefficients based on linearized analysis for an inviscid fluid (Reference 3) are presented in Tables I, II, and III. These are the coefficients representing the pressure differentials for the steady flow case for the following configurations:

Table I - NACA 0012,  $0^\circ \leq \alpha \leq 16^\circ$ ,  $0.3 \leq M_\infty \leq 0.8$

Table II - NACA 0012,  $3^\circ$  Negative Trailing Edge Flap,  
 $0^\circ \leq \alpha \leq 16^\circ$ ,  $0.3 \leq M_\infty \leq 0.8$

Table III - NACA 0015,  $2^\circ \leq \alpha \leq 12^\circ$ ,  $0.3 \leq M_\infty \leq 0.84$

---

\* Each coefficient of an orthogonal series can be determined independently.



Calculations contained in Table II were carried out for the flap configuration used on the outboard sections of the H-34 blades (Reference 9) and in the two-dimensional wind-tunnel tests reported in Reference 4.

Within the limits of the linearized theory used, the pressure differentials on the NACA 0012 and 0015 sections are the same (for the same angle of attack,  $\alpha$ , and Mach number,  $M_\infty$ ) because they both have zero camber. The corresponding theoretical pressure differentials have only  $A_0$  amplitudes (see Tables I and III). A deflected flap introduces an effective camber and, consequently, an  $A_1$  pressure differential component and a shift in the angle of attack for zero lift. This accounts for the differences between Tables I and II.

Results of least-squares fits to the pressure differential data given in References 4 and 5 are shown in Tables IV through VIII. Comparisons of Table I with Table IV, Table II with Table VI, and Table III with Table VIII immediately establish the lack of agreement between the theoretical and experimental values. One of the more striking differences is the presence of large  $A_2$  components in the experimental data.

The  $A_i$  coefficient data of Tables IV through VIII were normalized with respect to the sum  $(A_0 + \frac{1}{2} A_1)$  since this sum is proportional to the net airfoil circulation, and the results are presented in Tables IV through VIII as normalized quantities,  $\bar{A}_i$ . The lack of consistency noted in the  $\bar{A}_i$  values leads to the tentative conclusion that important viscous and compressibility effects may be present and, possibly, interactions between these. No precise boundary separates the two effects.

It is well known that the viscous effect for a flow over a smooth body will be confined to a very thin layer, the so-called boundary layer. The flow outside the boundary layer is a potential flow over a slightly different body which consists of the original airfoil and an additional thickness distribution due to the viscous effect. The NACA 0012 and NACA 0015 airfoils are symmetric; i.e., they have no geometric camber. However, viscous effects will modify the symmetry of those airfoils. Thus, a camber line due to the viscous effect is induced and contributes to the value of the  $A_1$  and higher Glauert terms observed in the two-dimensional wind-tunnel data. As speed increases, the boundary layer may change from laminar to turbulent. If the flow becomes turbulent, boundary layer displacement will be much thicker than the laminar one. If the flow separates, the boundary layer displacement will also be thicker. Both cases will increase the magnitude of  $A_1$ .

An increase in free-stream velocity increases the local Mach number for the profile until a zone of local supersonic flow has appeared and shock waves occur. As a result of the very large adverse pressure gradients imposed by the shock wave, the boundary layer thickens rapidly, generally becomes turbulent, and often separates from the profile, thus producing a large increase in the thickness of the wake. The change in effective body shape usually acts to decrease the lift and increase the drag. This coupling of the interaction between the shock wave and boundary layer

presents a formidable problem (Reference 11).

Boundary layer separation may develop at the leading edge or progress forward from the trailing edge. Leading edge separation will be emphasized here. Types of leading edge separation occurring on airfoils may be classified roughly as (1) separation with laminar reattachment, (2) separation with turbulent reattachment, and (3) separation without reattachment. As far as NACA 0012 and NACA 0015 airfoils are concerned, the most likely type in the operating lift coefficient range is type (2). The flow over a sharply curved leading edge encounters a strong adverse pressure gradient at high angle of attack. The flow cannot travel around the bend without laminar separation taking place. After separation, transition to turbulence occurs in the boundary layer somewhere downstream of separation. Transport mechanisms associated with the turbulent layer may cause reattachment. In between the separation and attachment points, there is an enclosed bubble of air. The size of the bubble has been found (Reference 12) to vary from a very small fraction of the chord to something comparable with the chord length. Airfoil thickness was found to be a parameter. The tests in Reference 12 show that a thin wing at small angle of attack develops a very small bubble near the leading edge. The size of the bubble increases with angle of attack until it encompasses the whole upper surface. For the moderately thicker wing, the bubble contracted slightly up to a certain angle of attack; beyond this, the bubble suddenly burst and caused an abrupt stall.

The presence of the air bubble and the boundary layer displacement will change the effective shape of the airfoil profile. Size of the air bubble and the thickness of boundary layer displacement depend on the speed of the freestream. With these two points in mind, it is not surprising that in Tables IV and VIII the  $A_1$  terms are dominant. Theoretically,  $A_0$  increases as both angle of attack and Mach number increase. However, the results of using a least-square fit to the experimental data show that the  $A_0$  term of the NACA 0012 airfoil increases with angle of attack but decreases with Mach number (see Table IV). The  $A_0$  term of NACA 0015 airfoil is quite random with respect to angle of attack and Mach number. No easily discernable patterns are apparent in Table VIII.

Lack of trends in the two-dimensional pressure distributions will make the rotor blade data obtained in flight difficult to interpret. It is worthwhile, therefore, to delve further into sources of the trouble. It appears that the source of the scatter might be the method of testing, i. e., changes of speed introduce both Reynolds number and Mach number changes. Further, no wall corrections were made for the 0015 pressure data.

The effects of change in Reynolds number and/or angle of attack on the separation characteristics of a two-dimensional airfoil can be estimated with the aid of a "Ville Plot" (Reference 13) such as that shown in Figure 19.

Figure 19 shows the influence on leading edge separation of the nondimensional leading edge radius,  $\ell$ , angle of attack,  $\alpha$ , and Reynolds number based on leading edge radius,  $R_\ell$ . The effects of compressibility are not displayed. The importance of this plot with regard to the Glauert coefficients is that the effective shape and, hence, the coefficients are changed as the operating point (speed, angle of attack) is changed.

In essence, the study of the two-dimensional airfoil data by the technique of developing Glauert coefficients, by least-squared curve fitting, has revealed several unexpected aspects with respect to the interpretation of the data. It will be seen that a similar situation exists for the rotor data.

#### H-34 DATA AT ADVANCE RATIO OF $\mu = 0.18$

Figures 7, 8, and 9 show the first three nondimensionalized Glauert coefficients for the H-34 flying at an advance ratio of  $\mu = 0.18$  at radial stations  $r/R = 0.40$ ,  $0.85$ , and  $0.90$ , respectively. The theoretical curves identified by the short dashed lines were obtained from Reference 1. The solid line marked "experimental data" corresponds to the determination of the Glauert coefficients from pressure distributions for the unsteady case, that is, the  $\bar{A}_i$  representation (Equation (5)). The  $\bar{C}_i$  coefficients (Equation (12)) are the straightforward fitting of the pressure distributions as though there were no unsteady effects.

The differences between the three curves could also be described in the following manner: The theoretical data are based on the assumption that the behavior of the airfoil sections is predominantly that of a flat plate without boundary-layer growth, whereas the experimental data contained the viscous effects and, of course, reflect the true environment for each section. The difference between the experimental fit for the curve  $\bar{A}_i$  and the curves marked  $\bar{C}_i$  should represent the unsteady effects.

Figure 7 shows the theoretical and two experimental representations of the nondimensional pressure distributions for the H-34 at advance ratio of  $\mu = 0.18$  and at radius  $r/R = 0.40$ . It is immediately evident that the theoretical predictions would indicate very small values for all the coefficients except  $\bar{A}_0$ . This is not, however, borne out by the experimental data. The experimental data show sizable values for on the retreating side of the disc and sizable values of  $\bar{A}_2$  over virtually all azimuthal positions. Furthermore, there appears to be an unsteady effect on  $\bar{A}_0$  and  $\bar{A}_1$  on the retreating side of the disc; that is, for the region  $180^\circ < \psi < 360^\circ$ . There is also an unsteady effect contributing to  $\bar{A}_2$  around the complete azimuth.

Figures 8 and 9 show the azimuthal distribution of the coefficients at nondimensional radial stations  $r/R = 0.85$  and  $0.90$ , respectively, for this same flight condition. Again, the experimental data do not agree

particularly well with the theoretical data for  $\bar{A}_1$  and  $\bar{A}_2$ ; even the  $\bar{A}_0$  coefficients for the experimental data depart from the theoretical coefficient values on the advancing side of the disc.\*

The unsteady effects at these larger radial stations ( $r/R = 0.85$  and  $0.90$ ) appear to be considerably less than at the inboard station  $r/R = 0.4$ , as can be seen by comparing the differences between the experimental  $\bar{A}_i$  coefficients and the experimental  $\bar{C}_i$  coefficients of Figures 8 and 9 and those of Figure 7. The other change that appears to occur with radial station is that  $\bar{A}_1$  and  $\bar{A}_2$  have large values on the advancing side at the larger radial stations (Figures 8 and 9), whereas these coefficients peak on the retreating side, as shown on Figure 7, at the inboard station. This change with radial station may simply be a manifestation of compressibility and tip effects dominating on the advancing side at the outer radial station and the stall effect contributing to the distortions of the pressure distribution at the inboard radii.

#### H-34 AT ADVANCE RATIO $\mu = 0.29$

The data for the H-34 at advance ratio of  $\mu = 0.29$  are shown in Figures 10, 11, and 12. At the most inboard radial station for this flight condition (Figure 10), the excursion of the coefficients on the retreating side is quite large. In fact, it was necessary to change the scale of the ordinate on Figure 10 compared to the others in the set of Figures 7 through 12. The other notable aspect about Figure 10 is the occurrence of quite large negative values for  $\bar{A}_1$  and  $\bar{C}_1$  on the retreating side of the disc. The coefficients  $\bar{A}_2$  and  $\bar{C}_2$  determined from the experiment are also negative for part of the retreating side of the disc. Again the outboard sections exhibit approximately the same characteristics as those observed at the lower advance ratio; namely, unsteady effects are relatively small, and the experimental values deduced for  $\bar{A}_1$  and  $\bar{A}_2$  are considerably larger than the corresponding analytic coefficients.

#### COMPARISON OF H-34 DATA AT AN ADVANCE RATIO OF $\mu = 0.18$ WITH DATA AT $\mu = 0.29$

Strong similarities exist for the outboard sections of the H-34 at the two advance ratios investigated. The inboard section, on the other hand, appears to have notable differences. This is best seen on the retreating side of the azimuth, where the  $\bar{A}_i$  coefficients are of different signs in the two cases and the  $\bar{A}_2$  coefficients also differ in sign over a portion of the retreating side. Obviously, the proximity of the blade

---

\* All three measures of the circulation--that is, theoretical ( $A_0 + \frac{1}{2} A_1$ ), experimental ( $A_0 + \frac{1}{2} A_1$ ), and flight ( $C_0 + \frac{1}{2} C_1$ )--are in reasonable agreement and, hence, the azimuthal variation of lift is similar. This only suggests that the gross flow properties (e.g., local momentum) are relatively insensitive to viscous and unsteady effects.

section to the reverse flow region could introduce the change in observed behavior. The tangential velocity at  $r/R = 0.4$  differs by a factor of two for these advance ratios at  $\psi = 270$  degrees. The low velocities (about 70 ft/sec for  $\mu = 0.29$  and about 140 ft/sec for  $\mu = 0.18$ ) make the section characteristics especially sensitive to inflow velocities that are locally high. Consequently, the local angle of attack and the local variation of the velocity over the chord could introduce the reversal of the camber effect noted in the comparison of these two cases.

#### UH-1A PRESSURE DISTRIBUTIONS AS FUNCTIONS OF SPANWISE STATION

The UH-1A data analyzed are shown in Figures 13, 14, and 15 for the case of  $\mu = 0.08$  and in Figures 16, 17, and 18 for  $\mu = 0.26$ .

Figure 13 displays the data at  $\mu = 0.08$  and  $r/R = 0.4$ . The  $\bar{A}_0$ ,  $\bar{A}_1$ ,  $\bar{A}_2$ , and corresponding  $\bar{C}$  are relatively constant over the azimuth except in the region from about  $\psi = 150$  degrees to about  $\psi = 230$  degrees. That azimuthal region is characterized by a change in sign in  $\bar{A}_1$  and  $\bar{C}_1$  and a sizable change in the value of the  $\bar{A}_0$  coefficient.

At radial stations  $r/R = 0.85$  and  $0.90$  (Figures 14 and 15, respectively), it is seen that the  $\bar{A}_1$  and  $\bar{C}_1$  coefficients representing the experimental data lie very close to each other and, hence, indicate that the unsteady effects are small. The other item of interest in Figures 14 and 15 is that the experimental  $\bar{A}_0$  coefficients are relatively low compared to the theoretical value and the  $\bar{A}_1$  and  $\bar{A}_2$  coefficients are quite sizable, while the theoretical coefficients for  $\bar{A}_1$  and  $\bar{A}_2$  are virtually zero. Returning again to Figure 13, it is noted that the agreement between the theoretical and experimental data is reasonable for  $\bar{A}_0$  but has appreciable errors in the  $\bar{A}_1$  and  $\bar{A}_2$  values. Again, the data at  $r/R = 0.4$  indicate larger unsteady effects than do the data for the outboard stations.

The UH-1A data at  $\mu = 0.26$  are shown in Figures 16, 17, and 18 at radial stations  $r/R = 0.40$ ,  $0.85$ , and  $0.90$ , respectively. Figure 16 shows that the  $\bar{A}_0$  component dominates on the advancing side of the blade; but on the retreating side ( $180^\circ < \psi < 360^\circ$ ), both the  $\bar{A}_1$  and  $\bar{A}_2$  coefficients become sizable. Here, again, the difference between the  $\bar{A}_1$  and  $\bar{C}_1$  coefficients indicates a substantial effect traceable to unsteady aerodynamics. Figures 17 and 18 indicate sizable excursions in all the measured coefficients at the outboard stations. Even the  $\bar{A}_0$  terms vary over a range from about 0.4 to a value somewhat greater than 1.0. Therefore, the theoretical curves which are dominated by  $\bar{A}_0$  are in disagreement with the experimental pressure distribution components. The  $\bar{A}_0$  and  $\bar{A}_1$  coefficients generally behave the same at  $r/R = 0.85$  and  $0.90$ , and similarly the  $\bar{A}_2$  coefficients are of the same type.\*

---

\* Note the change in the scale on Figure 17.

### COMPARISON OF UH-1A DATA AT ADVANCE RATIO $\mu = 0.08$ WITH DATA AT $\mu = 0.26$

Data obtained at an advance ratio of  $\mu = 0.26$  seem to have larger excursions than the data obtained at  $\mu = 0.08$  for the UH-1A rotor. The shapes of the respective curves at  $r/R = 0.85$  and  $0.90$  are roughly similar, but the curves at  $r/R = 0.40$  have some large differences. In particular, for  $240^\circ < \psi < 360^\circ$ , the  $\bar{A}_1$ ,  $\bar{C}_1$ , and  $\bar{A}_2$  Glauert coefficients have different signs for the two advance ratios.

### COMPARISON OF H-34 DATA WITH UH-1A DATA

The outboard sections for the two helicopter blades at the lower advance ratios have certain similarities that can be seen by comparing Figure 9 with Figure 15. However, the more inboard stations become less and less similar, although the excursions remain roughly comparable. At the higher advance ratios, the azimuthal signatures appear to be quite different except for the very low frequency content.

### COMPARISON OF TWO-DIMENSIONAL AIRFOIL DATA WITH ROTOR DATA

It is clear from the previous discussion of the results that the Glauert coefficient representation of pressure differentials is a sensitive indicator of the shape of the distribution. Further, strong azimuthal and radial dependencies are indicated in Figures 7 through 18. This point is further reinforced by the "hovering" data ( $\mu = 0$ ) for the UH-1A shown in Table X where the following ranges are noted:

$$\left. \begin{array}{l} 1.41 > \bar{C}_0 > 1.00 \\ 0.00 > \bar{C}_1 > 0.23 \\ 0.26 > \bar{C}_2 > 0.07 \end{array} \right\} \quad r/R = 0.40$$

$$\left. \begin{array}{l} 0.56 > \bar{C}_0 > 0.48 \\ 1.02 > \bar{C}_1 > 0.89 \\ 1.34 > \bar{C}_2 > 1.20 \end{array} \right\} \quad r/R = 0.85$$

$$\left. \begin{array}{l} 0.77 > \bar{C}_0 > 0.61 \\ 0.77 > \bar{C}_1 > 0.47 \\ 1.26 > \bar{C}_2 > 0.91 \end{array} \right\} \quad r/R = 0.90$$

Evidently, the division of circulation between the  $C_0$  and  $C_1$  distributions in the quantity  $(C_0 + \frac{1}{2}C_1)$  varies strongly with radius. It is of interest to compare these data with the two-dimensional data because this flight condition should have the smallest unsteady effects.

The basis for the comparison was equal normal force coefficients and equal Mach numbers. Test parameters given in Reference 10 were used to generate the following estimates for the UH-1A hovering condition:

$$\begin{array}{ll} \text{at } r/R = 0.40 & M_\infty \approx 0.30 \\ & C_L \approx 1.12 \\ \\ \text{at } r/R = 0.85 & M_\infty \approx 0.55 \\ & C_L \approx 0.78 \\ \\ \text{at } r/R = 0.90 & M_\infty \approx 0.58 \\ & C_L \approx 0.72 \end{array}$$

Section data curves in Reference 5 were entered with these values and corresponding geometric angles of attack were found to be 12 degrees, 7.5 degrees, and 7 degrees for  $r/R = 0.40$ ,  $0.85$ , and  $0.90$ , respectively. These values for  $\alpha$  and  $M_\infty$  were used to obtain Glauert coefficients by interpolation in Table VIII. The following comparison results:

UH-1A Rotor Data; $\mu = 0$			0015 Section Data	
$r/R = 0.40$	$1.41 > \bar{C}_0 > 1.00$	$\bar{C}_0 \approx 1.23$	$M_\infty \approx 0.3$ $\alpha \approx 12^\circ$	
	$0.00 > \bar{C}_1 > 0.23$	$\bar{C}_1 \approx 0.46$		
	$0.26 > \bar{C}_2 > 0.07$	$\bar{C}_2 \approx 0.117$		
$r/R = 0.85$	$0.56 > \bar{C}_0 > 0.48$	$\bar{C}_0 \approx 0.48$	$M_\infty \approx 0.55$ $\alpha \approx 7.5^\circ$	
	$1.02 > \bar{C}_1 > 0.89$	$\bar{C}_1 \approx 1.00$		
	$1.34 > \bar{C}_2 > 1.20$	$\bar{C}_2 \approx 1.30$		
$r/R = 0.90$	$0.77 > \bar{C}_0 > 0.61$	$\bar{C}_0 \approx 0.7$	$M_\infty \approx 0.585$ $\alpha \approx 7^\circ$	
	$0.77 > \bar{C}_1 > 0.47$	$\bar{C}_1 \approx 0.6$		
	$1.26 > \bar{C}_2 > 0.91$	$\bar{C}_2 \approx 1.1$		

The agreement between the Glauert coefficients for the two cases is surprisingly good in view of the various estimates required to make this particular comparison. Of course, the finite span effects must have influenced the results at  $r/R$  of  $0.85$  and  $0.90$ . Nevertheless, the behavior is apparently dominated by the Mach number and angle of attack (the Reynolds numbers in the two cases for the two sets of data were in

the range from one to about four million so that no large Reynolds number effect would be expected). The tentative conclusion to be drawn here is that for rotor stations inboard of 90 percent radius, most of the viscous effects are similar to those encountered with two-dimensional airfoils. There is required, however, an estimate of the angle of attack for such usage of two-dimensional wind-tunnel data.



## SERIES REPRESENTATION OF THICKNESS EFFECTS

### THEORETICAL VALUES

To find the pressure distribution due to the thickness of the NACA 0012 and 0015 airfoils, it is necessary to consider the effect of a round nose and finite trailing edge angles. In Reference 6, it is shown that the pressure due to the thickness of the airfoil is related to the surface slope of the airfoil through the following two equations

$$\frac{dy}{dx} = \frac{t}{2} \cot \frac{\theta}{2} - \frac{\theta_t}{2} \sin^2 \frac{\theta}{2} + \left( \frac{\theta_t}{\pi} - t \right) \sin \theta + \sum_{n=2}^{\infty} B_n \sin n\theta \quad (17)$$

$$\frac{C_p}{\sqrt{1-M_\infty^2}} = 2 \left[ \frac{\theta_t}{\pi} \sin^2 \frac{\theta}{2} \ln \left| \tan \frac{\theta}{2} \right| - \frac{1}{2} \left( \frac{\theta_t}{\pi} + t \right) + \left( \frac{\theta_t}{\pi} - t \right) \cos \theta + \sum_{n=2}^{\infty} B_n \cos n\theta \right] \quad (18)$$

where

- $y$  = the thickness function of the airfoil
- $t$  =  $\sqrt{\rho_n/b}$
- $\rho_n$  = leading edge radius
- $\theta_t$  = trailing edge angle
- $C_p$  = pressure coefficient
- $B_n$  = unknown coefficient to be computed

For NACA four-digit wing sections, the thickness  $y$  is given by (Reference 7)

$$\pm y = 5\tau \left[ .2969\sqrt{\chi} - .126\chi - .3516\chi^2 + .2843\chi^3 - .1015\chi^4 \right] \quad (19)$$

where  $\chi$ ,  $y$ , and  $\tau$  are nondimensionalized by the chord  $2b$ , and  $\tau$  = maximum thickness. The leading edge radius is given by

$$\rho_n = 1.1019 \tau^2$$

Differentiating Equation (19) with respect to  $\chi$ , one obtains

$$z \frac{dy}{dx} = 5\gamma \left[ \frac{.14845}{\sqrt{x}} - .126 - .7032x + .8529x^2 - .406x^3 \right] \quad (20)$$

The coefficient of  $\sin \theta$  in Equation (17) is defined to be  $B_1$  and is given by

$$B_1 = \frac{\theta_t}{\pi} - t$$

The remaining coefficients,  $B_n$ , in Equation (17) are determined by standard Fourier expansion techniques which depend on the orthogonality of the sine (and cosine) functions to give

$$B_n = \frac{2}{\pi} \int_0^\pi \left( \frac{dy}{dx} - \frac{t}{2} \cot \frac{\theta}{2} + \frac{\theta_t}{2} \sin^2 \frac{\theta}{2} \right) \sin n\theta d\theta; \quad n \geq 2 \quad (21)$$

Coefficient values presented below were obtained by numerical integration of Equation (21) after substitution of Equation (20).

	NACA 0012	NACA 0015
$B_1$	-0.0886	-0.1108
$B_2$	-0.0304	-0.0380
$B_3$	-0.0090	-0.0113
$B_4$	-0.0070	-0.0090
$B_5$	-0.0070	-0.0088
$B_6$	-0.0047	-0.0059
$B_7$	-0.0040	-0.0050
$B_8$	-0.0023	-0.0050
$B_9$	-0.0011	-0.0014
$B_{10}$	0	0

#### COMPARISON OF THEORETICAL AND EXPERIMENTAL RESULTS OF THICKNESS EFFECTS

Calculated pressure coefficients,  $C_p$ , due to thickness are compared with experimental results at zero angle of attack but with different Mach numbers. Figures 3 and 4 show good agreement between computed and experimental results.

## PROFILE DRAG ESTIMATES

### THEORETICAL ANALYSIS

A method proposed by Helmbold (Reference 11) is used for estimating profile drag. The profile drag coefficient for each surface of the airfoil of chord length  $c$  has the following form:

$$C_D = \frac{0.074}{R_N^{1/2}} \left[ \int_{\frac{x}{c}}^1 \left( \frac{u}{V_1} \right)^{3.5} d\left(\frac{x}{c}\right) + K_1 \right]^{0.8} \quad (22)$$

where

- $C_D$  = profile drag coefficient
- $R_N$  = Reynolds number based on chord and the free-stream velocity
- $x_t$  = position of boundary-layer transition from laminar to turbulent flow
- $u$  = local tangential velocity at the outer edge of the boundary layer
- $V_1$  = free-stream velocity
- $K_1 = 62.5 R_N^{1/4} \left( \frac{\theta_t}{c} \right)^{5/4} \left( \frac{U_t}{V_1} \right)^{3.75}$
- $\theta_t$  = boundary-layer momentum thickness at the point of transition
- $U_t$  = tangential velocity at the outer edge of the boundary layer at the laminar-to-turbulent transition point

The factor  $K_1$  is determined by the condition that the laminar and turbulent momentum thicknesses are equal at the point of transition. Hence,  $K_1$  is generally not the same on the upper and lower surfaces.

The velocity distribution at the outer edge of the boundary layer is related to the pressure measurements through Bernoulli's equations, i. e.,

$$C_p = \frac{p - p_\infty}{\frac{1}{2} \rho V_1^2} = 1 - \frac{u^2}{V_1^2} \quad (23)$$

or

$$\frac{u}{V_i} = \sqrt{1 - C_p}$$

where  $C_p$  = measured pressure coefficients.

Equation (23) applies to both upper and lower surfaces of the airfoil.

References 4 and 5 provide pressure measurements at both upper and lower surfaces, but only pressure differentials are given in References 8, 9, and 10. Therefore, the pressure coefficients on the upper and lower surfaces,  $C_{pu}$  and  $C_{pl}$ , respectively, are constructed by adding the experimental thickness effects to the experimental lifting effects. Let

$$\left(\frac{u_t}{V_i}\right)^2 = 1 - C_{pt} \quad (24)$$

where

$C_{pt}$  = measured pressure coefficients due to thickness (at zero angle of attack)

$u_t$  = velocity due to thickness

Then again using Bernoulli's equation for the upper and lower surfaces of the airfoil, one obtains

$$C_{pu} = \frac{p_u - p_\infty}{\frac{1}{2} \rho V_i^2} = 1 - \left(1 + \frac{u_t}{V_i} + \frac{u_c}{V_i}\right)^2 \quad (25)$$

$$C_{pl} = \frac{p_l - p_\infty}{\frac{1}{2} \rho V_i^2} = 1 - \left(1 + \frac{u_t}{V_i} - \frac{u_c}{V_i}\right)^2 \quad (26)$$

and

$$C_p = C_{pl} - C_{pu} = 4 \frac{u_c}{V_i} \left(1 + \frac{u_t}{V_i}\right) \quad (27)$$

where

$$\begin{aligned} p_u &= \text{pressure at upper surface} \\ p_l &= \text{pressure at lower surface} \\ u_c &= \text{velocity due to camber} \end{aligned}$$

For a given set of  $C_{p_u}$  and  $C_{p_l}$ , the velocity due to thickness can be computed by Equation (24), while Equation (27) provides the value of  $u_c$ . Then  $C_{p_u}$  and  $C_{p_l}$  can be found by substituting  $u_u$  and  $u_l$  into Equations (25) and (26), respectively. It should be noted that near the stagnation point, the second order effect, namely,  $u_t/V_i \times u_c/V_i$ , has to be included. Away from the stagnation point,  $u_t/V_i$  is small to compare with unity and Equation (27) reduces to a simpler form,

$$\frac{u_c}{V_i} = \frac{C_p}{4}$$

The position of the transition point  $x_t$ , on the upper surface, is assumed to be located at the point of minimum pressure, while the transition point on the lower surface is at the leading edge.

The boundary layer momentum thickness at the point of transition is given by Reference 11 (Equation 37 in Chapter 12):

$$\frac{\theta_t \left( \frac{x_t}{c} \right)}{c} = \left\{ \frac{0.47}{R_u \left[ \frac{u \left( \frac{x_t}{c} \right)}{V_i} \right]^5} \int_0^{\frac{x_t}{c}} \left[ \frac{u \left( \frac{x}{c} \right)}{V_i} \right]^5 d \left( \frac{x}{c} \right) \right\}^{1/2} \quad (28)$$

Equations (22) and (28) were integrated numerically by the trapezoidal rule; results are plotted in Figures 19 through 23.

#### COMPARISON OF THEORETICAL AND EXPERIMENTAL RESULTS FOR TWO-DIMENSIONAL CASES

The experimental data for the NACA 0012 airfoil section presented in Reference 4 were obtained on a section of an H-34 blade, and the drag was measured in two independent ways: (1) by means of a force balance and (2) by means of an integration of a wake survey. These results are indicated by the curves through the data points in Figures 20, 21, 22, and 23. One of the interesting aspects here is that the two methods of measurement give quite different results. The percentage errors

occurring at angles of attack greater than 4 degrees are exceptionally high. In general, there is a tendency to believe that the wake survey data is more representative of the two-dimensional airfoil than is the balance data. This situation occurs because the wake survey can be made near the centerline of the tunnel and can be relatively characteristic of the two-dimensional flow case; whereas, the balance data is influenced by side-wall effects and by the usual difficulties of developing an adequate drag balance. The calculated drag as a function of angle of attack and Mach number was determined from the pressure distributions and was based on the presumption of attached flow. Therefore, the calculated variation cannot exhibit the large changes that occur with flow separation at angle of attack near the stall angle. Nevertheless, it can be observed that the calculation based on the measured pressure distribution agrees well with the wake survey data up to the point of incipient stall.

The corresponding drag coefficients for the 0015 airfoil calculated from Equation (22) are compared with the experimental results from Reference 5 in Figure 24. The theory overpredicts the value of the drag at the lower angles of attack up to the critical Mach number. At an angle of attack of 8 degrees, however, the measured and theoretical values have come into good agreement at Mach numbers below the critical Mach number. The trend of these coefficients with angle of attack was correctly estimated. Again, the theory did not account for separation effects nor did it account for the occurrence of local shock waves.

#### ESTIMATES OF ROTOR PROFILE DRAG DISTRIBUTIONS

Since the drag calculation appeared to have merit, an effort was made to estimate the rotor blade drag characteristics on the basis of the measured pressure distribution. These results are summarized in Figures 25 through 28. In Figure 25 there is presented the azimuthal variation of the calculated drag coefficient for  $r/R = 0.40$ , and advance ratios of  $\mu = 0.18$  and  $\mu = 0.29$  for the H-34 (that is, 0012 airfoil section). The characteristics of the curves on Figure 25 are that the drag coefficients remain relatively constant for  $0 < \psi < 180$  degrees. The primary difference between the two advance ratios was the large increase experienced in the vicinity of  $\psi = 270$  degrees at the inboard section ( $r/R = 0.40$ ) for the higher  $\mu$  case. On Figure 26 there are plotted the variations of drag coefficients at the two outboard stations,  $r/R = 0.85$  and  $0.90$ . The drag coefficients have about the same characteristics as those noted at  $r/R = 0.40$  except that the amplitudes of the outboard variations are somewhat smaller.

The corresponding drag data for the UH-1A are shown in Figures 27 and 28. The characteristics previously pointed out for the H-34 data are also in evidence in the UH-1A data. The levels for the coefficients are very similar for the two rotors, and the variations with advance ratio are also quite similar.

## CONCLUSIONS

Both flight measured rotor and two-dimensional wind-tunnel differential pressure distributions of corresponding airfoil sections were fitted by a Glauert series representation, and the individual terms of the series were assessed for their physical significance. Inspection of these data and corresponding theoretical results lead to the following conclusions:

1. The theoretical result that the symmetric airfoils require only one Glauert coefficient to represent the pressure differential distribution is not supported by the experimental data for the NACA 0012 and 0015 since, for example, appreciable camber terms were found.
2. The Glauert-coefficients representing two-dimensional experimental data experience variations with Mach number and angle of attack which are not readily explainable. These variations may involve an interaction between boundary layer and compressibility phenomena.
3. Pressure distributions measured on rotors in flight as well as measured on airfoils in wind tunnels have strong similarities but also some notable differences. Apparently, the viscous and compressibility effects observed on two-dimensional airfoils are largely carried over when the same section is installed on the rotor blade.
4. The characteristic pressure differential components deduced from UH-1A and H-34 flight data are similar.
5. The magnitude of the higher Glauert components evident in the rotor pressure distributions suggest complex pitching moment variations and concomitant control loads.
6. The pressure distribution analyses indicated that unsteady effects tend to be concentrated at the inboard stations of the blade on the retreating side of the disk. However, no attempt was made to inspect results outboard of  $r/R = 0.90$ .

7. Rotor section drag estimates based on boundary layer theory appear to be useful, at sections where the flow does not separate. Rotor drag distributions have never been measured, so it is necessary to rely on calculation procedures to obtain such estimates analytically.



## RECOMMENDATIONS

Based on the results of this study, it is recommended that:

1. Further attempts be made to extract additional information from the available helicopter rotor blade pressure distribution measurements. Finite span effects and Mach number effects are among these.
2. An attempt be made to design an airfoil which, when operating in the regime of interest to helicopter rotors, will introduce negligibly small control loads. Judicious introduction of geometric camber is recommended. In particular, the camber components of the Glauert series would furnish required characteristics. It is believed that it would be necessary to account for viscous effects in such a design.
3. Attempts be made to relate stalled airfoil data in which rate effects are present to the distributions measured on the retreating side of the disk on helicopter rotors.
4. Transonic airfoil sections be designed to operate in an environment deduced from the available rotor measurements made at high shaft speed and high translational speeds.

### LITERATURE CITED

1. Piziali, R. A., A METHOD FOR PREDICTING THE AERO-DYNAMIC LOADS AND DYNAMIC RESPONSE OF ROTOR BLADES, Cornell Aeronautical Laboratory, Inc., USAAVLABS TR 65-74, U. S. Army Aviation Materiel Laboratories, Fort Eustis, Virginia, January 1966, AD 628583.
2. Daughaday, H., Piziali, R. A., and DuWaldt, F., ROTOR AIRLOADS, Proceedings of CAL/TRECOM Symposium, Cornell Aeronautical Laboratory, Buffalo, New York, 26-28 June 1963.
3. Milne-Thomson, L. M., THEORETICAL AERODYNAMICS, London, MacMillan and Company, Limited, 1948, p. 138.
4. Lizak, A. A., TWO-DIMENSIONAL WIND-TUNNEL TESTS OF AN H-34 MAIN ROTOR AIRFOIL SECTION, United Aircraft Corporation, Sikorsky Aircraft Division, Report SER-58304, TREC Technical Report 60-53, U. S. Army Aviation Materiel Laboratories, Fort Eustis, Virginia, September 1960.
5. Graham, D. J., Nitzberg, G. E., and Olson, R. N., A SYSTEMATIC INVESTIGATION OF PRESSURE DISTRIBUTIONS AT HIGH SPEEDS OVER FIVE REPRESENTATIVE NACA LOW-DRAG AND CONVENTIONAL AIRFOIL SECTIONS, NACA TR 832, 1945.
6. Woods, L. C., THE THEORY OF SUBSONIC PLANE FLOW London, Cambridge University Press, 1961, p. 332.
7. Abbott, I. H., and Von Doenhoff, A. E., THEORY OF WING SECTIONS, Dover Publications, Inc., New York, 1959, p. 113.
8. Scheiman, J., and Ludi, L. H., QUALITATIVE EVALUATION OF EFFECT OF HELICOPTER ROTOR-BLADE TIP VORTEX ON BLADE AIRLOADS, NASA TN D-1637, May 1963.
9. Scheiman, J., A TABULATION OF HELICOPTER ROTOR-BLADE DIFFERENTIAL PRESSURES, STRESSES, AND MOTIONS AS MEASURED IN FLIGHT, NASA TM X-952, March 1964.
10. Burpo, F. B., and Lynn, R. R., MEASUREMENT OF DYNAMIC AIRLOADS ON A FULL-SCALE SEMIRIGID ROTOR, Bell Helicopter Report 525-099-001, TCREC Technical Report 62-42, December 1962.

11. Schlichting, H., BOUNDARY-LAYER THEORY, McGraw-Hill Book Company, Inc., New York, 1960.
12. McCullough, G. B., and Gault, D. E., EXAMPLES OF THREE REPRESENTATIVE TYPES OF AEROFOIL-SECTION STALL AT LOW SPEEDS, NACA TN 502, 1951.
13. Ville, THE EFFECT OF SEPARATIONS AT THE LEADING EDGE ON THE AERODYNAMIC FEATURES OF WINGS NASA TT F-12, 546, September 1969.

TABLE I. THEORETICAL GLAUERT COEFFICIENTS FOR NACA 0012 AIRFOIL (COMPRESSIBILITY INCLUDED)												
$M_{\infty}$	$A_i$	$\alpha^\circ$										
		0	2	4	6	8	10	12	14	16		
0.3	$A_0$	0	.0367	.0734	.1101	.1468	.1834	.2201	.2568	.2935		
0.4	$A_0$	0	.0382	.0764	.1146	.1528	.1909	.2291	.2673	.3055		
0.5	$A_0$	0	.0404	.0808	.1212	.1616	.2021	.2428	.2829	.3233		
0.6	$A_0$	0	.0438	.0875	.1312	.1750	.2187	.2625	.3063	.3500		
0.65	$A_0$	0	.0461	.0921	.1382	.1842	.2303	.2763	.3224	.3684		
0.70	$A_0$	0	.0490	.0980	.1470	.1960	.2451	.2941	.3431	.3921		
0.75	$A_0$	0	.0529	.1058	.1587	.2117	.2645	.3175	.3704	.4233		
0.80	$A_0$	0	.0583	.1166	.1750	.2333	.2917	.3500	.4083	.4666		

TABLE II. THEORETICAL GLAUERT COEFFICIENTS FOR NACA 0012 AIRFOIL WITH TRAILING EDGE FLAP (NEGATIVE THREE DEGREES FLAP ANGLE)												
$M_\infty$	$A_i$	$\alpha^\circ$										
		0	2	4	6	8	10	12	14	16		
0.3	$A_0$	-.00535	.0314	.0680	.1047	.14140	.1780	.2147	.2514	.2881		
	$A_1$	-.01066	-.01066	-.01066	-.01066	-.0106	-.01066	-.01066	-.0106	-.0106		
0.4	$A_0$	-.00556	.0328	.0710	.1082	.1471	.1845	.2235	.2620	.2999		
	$A_1$	-.01101	-.01101	-.01101	-.01101	-.0110	-.01101	-.0110	-.01101	-.0110		
0.5	$A_0$	-.00589	.0350	.0754	.1158	.1557	.1967	.23660	.2775	.3174		
	$A_1$	-.01174	-.01174	-.01174	-.01174	-.0117	-.01174	-.0117	-.01174	-.0117		
0.6	$A_0$	-.00638	.0384	.082	.12487	.1696	.2123	.2571	.3009	.3436		
	$A_1$	-.01271	-.01271	-.01271	-.01271	-.01271	-.0127	-.01271	-.01271	-.0127		
0.7	$A_0$	-.00714	.0436	.0908	.1416	.18890	.2397	.2887	.3377	.3849		
	$A_1$	-.01424	-.01424	-.0142	-.01424	-.0142	-.01424	-.01424	-.01424	-.0142		
0.8	$A_0$	-.00850	.0498	.1081	.1696	.2279	.2863	.3446	.4029	.4612		
	$A_1$	-.01695	-.0169	-.0109	-.01695	-.01695	-.01695	-.01695	-.01695	-.01695		

TABLE III. THEORETICAL GLAUERT COEFFICIENTS FOR NACA 0015 AIRFOIL

$\alpha = 2^\circ$														
$M_\infty$	0.3	0.4	0.5	0.55	0.60	0.625	0.651	0.676	0.701	0.726	0.752	0.779	0.806	0.835
$A_0$	.0367	.0382	.0404	.0415	.0438	.0448	.0461	.0475	.0491	.0509	.0531	.0558	.0591	.0636
$\alpha = 4^\circ$														
$M_\infty$	0.3	0.4	0.5	0.55	0.60	0.625	0.651	0.676	0.702	0.729	0.755	0.782	0.805	0.837
$A_0$	.0734	.0764	.0808	.0831	.0875	.0897	.0922	.095	.0983	.1023	.1075	.1123	.1180	.1279
$\alpha = 6^\circ$														
$M_\infty$	0.3	0.4	0.5	0.55	0.601	0.626	0.652	0.678	0.704	0.731	0.757	0.789	0.811	0.839
$A_0$	.1101	.1146	.1212	.1245	.1314	.1347	.1385	.1429	.1479	.1539	.1607	.1692	.1795	.1930
$\alpha = 8^\circ$														
$M_\infty$	0.3	0.4	0.500	0.526	0.551	0.576	0.602	0.629	0.655	0.682	0.708	0.735	0.762	0.789
$A_0$	.1468	.1528	.1616	.1646	.1678	.1713	.1753	.1801	.1853	.1914	.1982	.2065	.2162	.2279
$\alpha = 10^\circ$														
$M_\infty$	0.3	0.4	0.501	0.527	0.553	0.580	0.606	0.633	0.659	0.689	0.712	0.739	0.766	0.794
$A_0$	.1835	.1910	.2022	.2059	.2100	.2148	.2200	.2261	.2327	.2402	.2492	.2598	.2722	.2879
$\alpha = 12^\circ$														
$M_\infty$	0.3	0.401	0.504	0.530	0.557	0.583	0.609	0.635	0.662	0.689	0.713	0.743	0.771	0.800
$A_0$	.2201	.2292	.2431	.2474	.2529	.2585	.2648	.2718	.2802	.2898	.2995	.3138	.3298	.350
														.3785

TABLE IV. FIRST THREE GLAUERT COEFFICIENTS,  $A_0$ ,  $A_1$ ,  $A_2$ ,  
OBTAINED FROM MEASURED PRESSURE DIFFERENTIALS  
ON NACA 0012 AIRFOIL SECTION

$M_\infty$	$A_i$	$\alpha$							
		2	4	6	8	10	12	14	16
0.30	$A_0$	.0135	.0317	.0511	.0741	.0980	.1109	.1167	.0169
	$A_1$	.0586	.0863	.1008	.1479	.1570	.1641	.1654	.2618
	$A_2$	.0423	.0762	.1177	.1438	.1731	.2008	.2128	.0799
0.40	$A_0$	.0127	.0301	.0508	.0776	.1012	.0739	.0609	.0388
	$A_1$	.0384	.0787	.0973	.1360	.1455	.2117	.2135	.2312
	$A_2$	.0432	.0875	.1338	.1543	.1737	.2201	.1156	.0726
0.50	$A_0$	.0085	.0264	.0385	.0285	.0490	.0578	.0372	.0344
	$A_1$	.0408	.1059	.1542	.2334	.2162	.1923	.2309	.2395
	$A_2$	.0456	.1057	.1643	.2567	.2412	.1458	.1138	.0970
0.60	$A_0$	.0089	.0157	.0279	.0298	.0352	.0476	.0408	.0324
	$A_1$	.0629	.1431	.1947	.2313	.2274	.2056	.2102	.2338
	$A_2$	.0647	.1462	.2101	.2490	.1745	.0979	.0484	.0582
0.65	$A_0$	.0080	.0206	.0255	.0756	.0310	.0401	.0433	.0331
	$A_1$	.0801	.1339	.2193	.2314	.2268	.2027	.2104	.2881
	$A_2$	.0824	.1540	.2363	.2014	.1353	.0696	.0579	.1232
0.70	$A_0$	.0054	.0116	.0172	.0226	.0239	.0323	.0425	.0346
	$A_1$	.0968	.1670	.1974	.2224	.2327	.2120	.1920	.2830
	$A_2$	.1031	.1743	.2011	.1715	.1146	.0615	.1733	.0774
0.75	$A_0$	.0027	.00840			.0168			
	$A_1$	.0948	.1372			.2659			
	$A_2$	.0909	.1024			.1002			
0.80	$A_0$	.0001	.0039						
	$A_1$	.0878	.1063						
	$A_2$	.0192	.0315						

TABLE V. FIRST THREE NONDIMENSIONAL GLAUERT COEFFICIENTS,  
 $\bar{A}_0$ ,  $\bar{A}_1$ ,  $\bar{A}_2$ , OBTAINED FROM MEASURED PRESSURE  
DIFFERENTIALS ON NACA 0012 AIRFOIL SECTION

$M_\infty$	$\bar{A}_i$	$\alpha^\circ$							
		2	4	6	8	10	12	14	16
0.30	$\bar{A}_0$	.3156	.4116	.5037	.5005	.5552	.5748	.5851	.1144
	$\bar{A}_1$	1.3688	1.1768	.9927	.9991	.8895	.8504	.8299	1.7712
	$\bar{A}_2$	.9886	1.0393	1.1590	.9711	.9805	1.0406	1.0673	.5403
0.40	$\bar{A}_0$	.3983	.4331	.5108	.5329	.5819	.4114	.3632	.2513
	$\bar{A}_1$	1.2034	1.1338	.9784	.9341	.8363	1.1773	1.2736	1.4974
	$\bar{A}_2$	1.3545	1.2599	1.3455	1.0600	.9984	1.2236	.6900	.4704
0.50	$\bar{A}_0$	.2927	.3325	.3333	.1961	.3121	.3751	.7437	.2230
	$\bar{A}_1$	1.4147	1.3351	1.3334	1.6079	1.3758	1.2499	1.5126	1.5541
	$\bar{A}_2$	1.5786	1.3320	1.4300	1.7682	1.5349	.9453	.7454	.6290
0.60	$\bar{A}_0$	.2200	.1803	.2228	.2051	.2415	.3166	.2797	.2168
	$\bar{A}_1$	1.5600	1.6394	1.5545	1.5898	1.5169	1.3668	1.4406	1.5664
	$\bar{A}_2$	1.6035	1.6756	1.6775	1.7116	1.1642	.0508	.3317	.3902
0.65	$\bar{A}_0$	.1656	.2355	.1886	.1813	.2146	.2835	.2916	.1867
	$\bar{A}_1$	1.6687	1.5291	1.6228	1.6373	1.5707	1.4331	1.4168	1.6267
	$\bar{A}_2$	1.7157	1.7582	1.7488	1.4250	.9307	.4919	.3898	.0956
0.70	$\bar{A}_0$	.1011	.1228	.1482	0.1689	.1703	.2337	.3066	.1963
	$\bar{A}_1$	1.7978	1.7544	1.7035	1.6623	1.6594	1.5327	1.3868	1.6074
	$\bar{A}_2$	1.3152	1.8310	1.7357	1.2817	.8172	.4448	.1251	.4399
0.75	$\bar{A}_0$	.0539	.1091			.1119			
	$\bar{A}_1$	1.8923	1.7818			1.7761			
	$\bar{A}_2$	1.8137	1.3299			.6695			
0.80	$\bar{A}_0$	.0237	.0679						
	$\bar{A}_1$	1.9953	1.8642						
	$\bar{A}_2$	.0435	.5521						



TABLE VI. FIRST THREE GLAUERT COEFFICIENTS, $A_0$ , $A_1$ , $A_2$ , OBTAINED FROM MEASURED PRESSURE DIFFERENTIALS ON NACA 0012 AIR-FOIL SECTION WITH TRAILING EDGE FLAP (THREE DEGREES FLAP ANGLE)										
$M_\infty$	$A_i$	$\alpha^\circ$								
		0	2	4	6	8	10	12	14	16
0.30	$A_0$	-.0047	.0080	.0270	.0445	.0672	.0884	.1044	.1217	.0794
	$A_1$	-.0072	.0131	.0544	.0926	.1199	.1429	.1556	.1535	.1552
	$A_2$	-.0024	.0408	.0808	.1237	.1550	.1888	.2200	.2226	.0373
0.40	$A_0$	-.0054	.0095	.0268	.0456	.0693	.0969	.0859	.0290	.0446
	$A_1$	-.0084	.0214	.0667	.1053	.1283	.1334	.1806	.2445	.2119
	$A_2$	-.0071	.0458	.0922	.1345	.1651	.1803	.2280	.1272	.0644
0.50	$A_0$	-.0076	.0088	.0243	.0387	.0292	.0452	.0596	.0371	.0370
	$A_1$	-.0066	.0292	.0786	.1380	.2155	.2203	.1863	.2210	.2191
	$A_2$	.0093	.0525	.1069	.1630	.2572	.2556	.1445	.1185	.0864
0.60	$A_0$	-.0058	.0062	.0136	.0247	.0238	.0340	.0445	.0419	.0353
	$A_1$	-.0163	.0433	.1131	.1708	.1976	.2139	.1972	.1912	.2334
	$A_2$	-.0008	.0636	.1383	.2043	.2196	.1667	.1175	.0579	.0925
0.70	$A_0$	-.0061	.0019	.0080	.0141	.0209	.0222	.0271	.0347	.0301
	$A_1$	-.0204	.0617	.1408	.1844	.2076	.2193	.2017	.1976	.2804
	$A_2$	-.0021	.0884	.1727	.2151	.1772	.1385	.0721	.0555	.0934
0.80	$A_0$	-.0065	-.0001	.0045						
	$A_1$	-.0460	.0672	.0932						
	$A_2$	.0365	.0172	.0885						

TABLE VII. FIRST THREE NONDIMENSIONAL GLAUERT COEFFICIENTS,  $\bar{A}_0$ ,  $\bar{A}_1$ ,  $\bar{A}_2$ , OBTAINED FROM MEASURED PRESSURE DIFFERENTIALS ON NACA 0012 AIRFOIL SECTION WITH TRAILING EDGE FLAP (THREE DEGREES FLAP ANGLE)

$M_\infty$	$\bar{A}_i$	$\alpha^\circ$								
		0	2	4	6	8	10	12	14	16
0.3	$\bar{A}_0$	.5672	.5512	.4985	.4900	.5287	.5530	.5730	.6133	.5057
	$\bar{A}_1$	.8657	.8976	1.0028	1.0199	.9427	.8940	.8541	.7734	.9886
	$\bar{A}_2$	.2888	2.8033	1.4905	1.3625	1.2263	1.1814	1.2081	1.1217	.2375
0.4	$\bar{A}_0$	.6036	.4717	.4456	.4645	.5195	.5922	.4876	.1916	.2965
	$\bar{A}_1$	.7929	1.0565	1.1088	1.0711	.9611	.8155	1.0215	1.6169	1.4071
	$\bar{A}_2$	-.6750	2.2617	1.5314	1.3687	1.2368	1.1023	1.2938	.8399	.4277
0.5	$\bar{A}_0$	.6965	.3727	.3819	.3593	.2134	.2910	.3902	.2513	.2525
	$\bar{A}_1$	.6069	1.2547	1.2362	1.2813	1.5733	1.4180	1.2196	1.4974	1.4950
	$\bar{A}_2$	-.8500	2.2522	1.6810	1.5133	1.8778	1.6452	.9458	.8028	.5899
0.6	$\bar{A}_0$	.4153	.2227	.1935	.2246	.1677	.2414	.0311	.3048	.2323
	$\bar{A}_1$	1.1694	1.5546	1.6131	1.5508	1.6646	1.5172	1.3782	1.3905	1.5354
	$\bar{A}_2$	.0538	2.2839	1.9721	1.8553	1.4204	1.3242	.8212	.4207	.6086
0.7	$\bar{A}_0$	.3759	.0579	.1016	.1329	.1940	.1684	.2115	.2600	.1769
	$\bar{A}_1$	1.2483	1.8441	1.7968	1.7341	1.6120	1.6632	1.5770	1.4801	1.6461
	$\bar{A}_2$	.1314	2.6987	2.2046	2.0228	1.7919	1.6507	.5638	.4153	.5485
0.8	$\bar{A}_0$	.2196	-.0378	.0882						
	$\bar{A}_1$	1.5608	2.0756	1.8236						
	$\bar{A}_2$	-1.2369	.5305	.9107						



TABLE VIII - Continued

$\alpha = 6^\circ$

$A_1$	$M_\infty$											
	.300	.400	.500	.550	.601	.626	.652	.678	.704	.731	.757	.784
$A_0$	.0701	.0687	.0688	.0678	.0838	.0943	.0743	.0667	.0604	.0534	.0507	.0431
$A_1$	.0540	.0532	.0751	.0815	.0589	.0463	.0717	.0682	.0622	.0647	.0650	.0520
$A_2$	.0965	.1094	.1230	.1251	.1554	.1250	.1314	.1237	.0946	.0848	.0701	.0509
$\bar{A}_0$	.7219	.6850	.647	.6250	.7401	.8029	.675	.6617	.6602	.6226	.6094	.6175
$\bar{A}_1$	.5561	.6300	.706	.7501	.5198	.3943	.651	.6767	.6796	.7549	.7812	.7649
$\bar{A}_2$	.9941	1.0911	1.1569	1.1520	1.3525	1.0647	1.1922	1.2273	1.0341	.9885	.8428	.8569
												.8841
												2.7043

$\alpha = 8^\circ$

$A_1$	$M_\infty$											
	.300	.400	.500	.526	.551	.576	.602	.629	.655	.682	.708	.735
$A_0$	.0802	.0968	.0840	.0537	.0598	.1090	.0940	.0839	.0887	.0689	.0603	.0604
$A_1$	.0922	.0850	.1138	.1649	.1623	.0861	.0850	.0879	.0991	.0872	.0876	.0800
$A_2$	.1254	.1443	.1885	.2406	.2104	.1250	.1361	.1257	.1261	.1002	.0346	.0784
$\bar{A}_0$	.6616	.6949	.5960	.3945	.4242	.7169	.6886	.6561	.5805	.6125	.5795	.6017
$\bar{A}_1$	.6768	.6101	.8080	1.2110	1.1516	.5663	.6229	.6878	.8391	.7750	.8409	.7967
$\bar{A}_2$	.8206	1.0365	1.3376	1.7672	1.4936	.2218	.9968	.9829	1.0675	.8902	.9088	.7805
												.8290
												.6624
												.7762
												.6201
												.7597
												.0553
												.0578
												.0591
												.6201
												.7597
												.6624
												.7762

TABLE VIII - Continued

$\alpha = 10^\circ$															
$A_i$	$M_\infty$														
	.300	.400	.501	.527	.553	.580	.606	.633	.659	.685	.712	.739	.766	.794	.824
$A_0$	.1314	.1563	.0509	.0627	0.0660	.0704	.0681	.0670	.0609	.0609	.0593	.0599	.0591	.0596	.0541
$A_1$	.0556	.0272	.1861	.1678	.1483	.1307	.1212	.1237	.1225	.1209	.1179	.1041	.0961	.0836	.0268
$A_2$	.1222	.0966	.2898	.2372	.1901	.1640	.1454	.1255	.1168	.1072	.0942	.0762	.0550	.0504	.0663
$\bar{A}_0$	.8255	.9199	.3534	0.4276	.4710	.5787	.5293	.5202	.4986	.5017	.5014	.5351	.5515	.5271	.4728
$\bar{A}_1$	.3490	.1603	1.2932	1.1448	1.0580	.9626	.9414	.9597	1.0028	.9965	.9973	.9298	.8969	.8244	.8543
$\bar{A}_2$	.7677	.5686	2.0134	1.6193	1.3570	1.2073	1.1292	.9736	.3562	.8840	.7968	.6803	.5128	.4974	.7010
$\alpha = 12^\circ$															
$A_i$	$M_\infty$														
	0.300	.401	.504	.530	.557	.583	.609	.635	.662	.689	.713	.743	.771	.804	.932
$A_0$	0.2325	.1987	.0890	.0638	.0734	.0684	.0605	.0617	.0613	.0722	.0549	.0518	.0505	.0514	.0548
$A_1$	-.0873	-.0138	.1212	.1169	.1284	.1320	0.1414	0.1344	.1316	.1028	.1214	.1387	.1320	.1344	.1474
$A_2$	.0221	.0293	.1278	.1075	.1043	.1093	.1278	0.1272	.1208	.0851	.0584	.0864	.0927	.0828	.0656
$\bar{A}_0$	1.2311	1.0360	.5955	.5893	.5336	.5090	.4610	.4786	.4822	.5841	.4750	.4279	.4318	.4481	.3957
$\bar{A}_1$	.4622	-.0713	.8091	.8214	.9328	.9820	1.0780	1.0428	1.0357	.8318	1.0500	1.1443	1.1363	1.1038	1.2086
$\bar{A}_2$	0.1170	0.153	.8552	.7556	.7581	.8133	.9742	.9865	.9506	.0517	.5048	.7129	.7922	.5328	.4736

TABLE IX. FIRST THREE NONDIMENSIONAL GLAUERT COEFFICIENTS, $\bar{C}_0$ , $\bar{C}_1$ , $\bar{C}_2$ , OBTAINED FROM H-34 FLIGHT DATA (0012 AIRFOIL SECTION)													
$\mu = 0.18 \quad r = 0.40$													
$\bar{C}_i$	$\gamma$												
	0	30	60	90	120	150	180	210	240	270	300	330	
$\bar{C}_0$	.8514	.8975	.8885	.8647	.8848	.8449	.8449	.8298	.7737	.6208	.6394	.7383	
$\bar{C}_1$	.2972	.2049	.2231	.2706	.2304	.2984	.3103	.3404	.4526	.7584	.7212	.5234	
$\bar{C}_2$	.0582	.0359	.0697	.0445	.0911	.1422	.1844	.1805	.2224	.2026	.1009	.0699	
$\mu = 0.18 \quad r = 0.85$													
$\bar{C}_0$	1.0272	.8053	.7518	.7381	.6950	.6950	.7661	.8172	.8844	.9824	.9549	1.0725	
$\bar{C}_1$	-.0545	.3895	.4965	.5237	.6099	.3655	.2311	.0352	.2311	.0870	.0914	.1449	
$\bar{C}_2$	.3370	.8777	1.1438	1.1470	1.1095	.8266	.6450	.4794	.2928	.3573	.3566	.1934	
$\mu = 0.18 \quad r = 0.90$													
$\bar{C}_0$	.8633	.7807	.7549	.5452	.6857	.7462	.8268	.8300	.8683	.9975	.8588	.9141	
$\bar{C}_1$	.2734	.4388	.4901	.9095	.6286	.5076	.3465	.3400	.433	.0050	.2824	.1718	
$\bar{C}_2$	.5165	.7417	.9161	1.1108	.9082	.707	.5598	.4530	.3904	.1891	.4037	.3753	
$\mu = 0.29 \quad r = 0.40$													
$\bar{C}_0$	1.2749	.9451	.9608	.819	.8559	.9018	.9307	1.3007	2.0670	2.6964	1.9333	1.3273	
$\bar{C}_1$	-.5493	.1098	.0734	.3007	.2882	.1963	.1385	-.6014	-.2134	-3.3927	-1.8665	-.6546	
$\bar{C}_2$	.0408	-.1260	-.1762	.1186	.0313	.0853	.0823	.2967	.1221	.0632	-.2724	.0692	
$\mu = 0.29 \quad r = 0.85$													
$\bar{C}_0$	1.0968	.9228	.7938	.9470	.9254	.7597	.8266	.9293	.9692	.0892	.9282	1.1145	
$\bar{C}_1$	-.1936	.1545	.4125	.1060	.1491	.4806	.3468	.1414	.0615	.2216	.1434	-.2901	
$\bar{C}_2$	.1369	.6083	1.0996	1.3232	.9208	.7929	.5850	.3384	.2645	.4170	.3711	.0470	
$\mu = 0.29 \quad r = 0.90$													
$\bar{C}_0$	1.0333	.8547	.7686	.8304	.7249	.6880	.7922	.8743	.9833	.8734	.8537	1.1353	
$\bar{C}_1$	-.0667	.2906	.4629	.3391	.5502	.6241	.4156	.2513	.0334	.2532	.2927	-.2707	
$\bar{C}_2$	.2215	.6262	.9862	1.2343	1.0727	.8353	.5794	.4250	.7054	.3841	.4113	.0227	

TABLE X. FIRST THREE NONDIMENSIONAL GLAUERT COEFFICIENTS,  $\bar{C}_0$ ,  $\bar{C}_1$ ,  $\bar{C}_2$ ,  
OBTAINED FROM UH-1A FLIGHT DATA (0015 AIRFOIL SECTION)

$\mu = 0.0 \quad \bar{r} = 0.40$												
$\bar{C}_i$	$\psi$											
	0°	30°	60°	90°	120°	150°	180°	210°	240°	270°	300°	330°
$\bar{C}_0$	1.0289	1.0682	1.1179	1.0643	1.0570	1.4073	1.0422	1.0576	1.0840	1.0138	1.0021	1.0055
$\bar{C}_1$	-.0579	-.1384	-.2357	-.1286	-.1140	-.0946	-.0845	-.1153	-.1681	-.0877	-.0043	-.0110
$\bar{C}_2$	.2299	.1357	.0708	.1772	.1821	.1859	.1791	.1588	.1368	.1657	.2141	.2624
$\mu = 0.0 \quad \bar{r} = 0.85$												
$\bar{C}_0$	.5292	.5008	.4979	.5184	.5432	.5274	.4890	.5390	.5338	.5499	.5505	.5545
$\bar{C}_1$	.9416	.9984	1.0042	.9632	.9136	.9451	1.022	.9219	.9324	.9003	.8989	.8931
$\bar{C}_2$	1.3031	1.3356	1.3300	1.2882	1.2252	1.2516	1.2769	1.2043	1.2255	1.2018	1.2561	1.2379
$\mu = 0.0 \quad \bar{r} = 0.90$												
$\bar{C}_0$	.7389	.7122	.7552	.7609	.6445	.6411	.7147	.6170	.6943	.7686	.6805	.7242
$\bar{C}_1$	.5221	.5757	.4897	.4783	.7109	.7179	.5706	.7661	.61134	.4629	.6390	.5516
$\bar{C}_2$	1.0890	1.0721	1.0052	.9926	1.2297	1.2744	1.0622	1.2693	1.0950	.9151	1.1773	1.0397
$\mu = 0.08 \quad \bar{r} = 0.40$												
$\bar{C}_0$	1.0726	1.0817	1.1233	1.1134	1.1109	1.0398	.8939	.9157	1.0384	1.0898	1.0821	1.0568
$\bar{C}_1$	-.1452	.1635	.2467	-.2269	.2218	.0795	.2122	.1686	-.0767	-.1796	-.1641	-.1136
$\bar{C}_2$	.1473	.1459	.1046	.0.957	.1229	.1718	.2371	.1749	.0699	.0628	.1533	.1789
$\mu = 0.08 \quad \bar{r} = 0.85$												
$\bar{C}_0$	.5103	.4936	.5483	.4723	.4532	.4635	.5338	.6115	.6407	.5971	.6272	.6367
$\bar{C}_1$	.9794	1.0329	.9033	1.0554	1.0936	1.0731	.9324	.7770	.7186	.8057	.7456	.7266
$\bar{C}_2$	1.3484	1.4520	1.5242	1.5152	1.5763	1.4451	1.2840	1.1045	1.0366	1.0204	1.0289	1.0594

TABLE X - Continued

$\mu = 0.08 \quad \bar{r} = 0.90$												
$\bar{c}_i$	$\psi$											
	0°	30°	60°	90°	120°	150°	180°	210°	240°	270°	300°	330°
$\bar{c}_0$	.7972	.7572	.7316	.5447	.7063	.7155	.7624	.8062	.8572	.8935	.8236	.8262
$\bar{c}_1$	.4056	.4856	.5368	.9105	.5873	.5691	.4752	.3877	.2856	.2131	.3528	.3476
$\bar{c}_2$	.9155	1.0288	1.2721	1.3654	1.1341	.9917	.9059	.7788	.6124	.5892	.7381	.7685
$\mu = 0.26 \quad \bar{r} = 0.40$												
$\bar{c}_0$	1.0209	1.1286	1.2309	1.1451	1.0927	1.0675	1.0389	1.1422	1.0785	.6906	.8960	.9891
$\bar{c}_1$	-.0417	-.2573	-.4618	-.2901	-.1855	-.1350	-.0777	-.2844	-.1570	.6184	.2080	.0218
$\bar{c}_2$	.2210	.1563	.0454	.1130	.1417	.1509	.1943	.0083	-.2137	-.1617	.3298	.1539
$\mu = 0.26 \quad \bar{r} = 0.85$												
$\bar{c}_0$	.2040	.4789	.6580	.6747	1.1293	.4899	.5014	.7889	.7039	.9017	.9394	.7396
$\bar{c}_1$	1.5920	1.0421	.6840	.6505	-.2587	1.0202	.9972	.4226	.5971	.1966	.1213	.5209
$\bar{c}_2$	1.8847	1.6054	1.4133	1.6892	1.1967	1.4887	1.3408	.7679	.9379	.3912	.1468	.9026
$\mu = 0.26 \quad \bar{r} = 0.90$												
$\bar{c}_0$	.4661	.4399	.6655	.6966	.7892	.4409	.7053	.9271	.8996	.9946	1.1171	1.0264
$\bar{c}_1$	1.0679	1.1203	.6690	.6068	.4216	1.1183	.5895	.1457	.2009	.0107	-.2342	-.0528
$\bar{c}_2$	1.5012	1.6773	1.2556	1.2164	1.4477	1.4627	.9254	.4992	.4540	.2834	-.3222	.3520



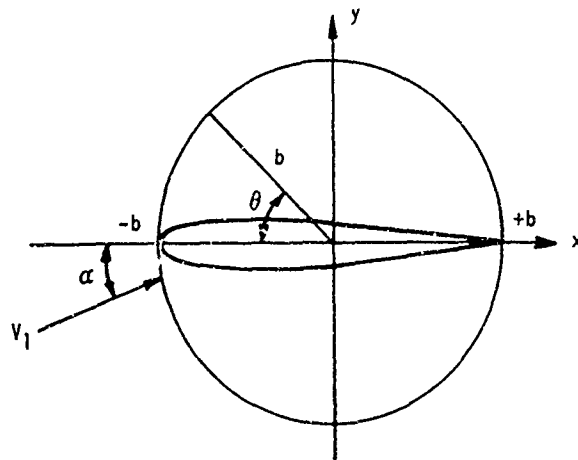


Figure 1. AIRFOIL CHORD POSITION REPRESENTATION IN CARTESIAN AND POLAR COORDINATES.

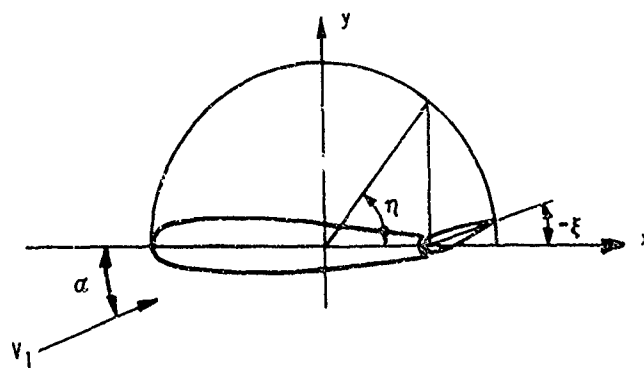


Figure 2. COORDINATES FOR AIRFOIL WITH A FLAP.

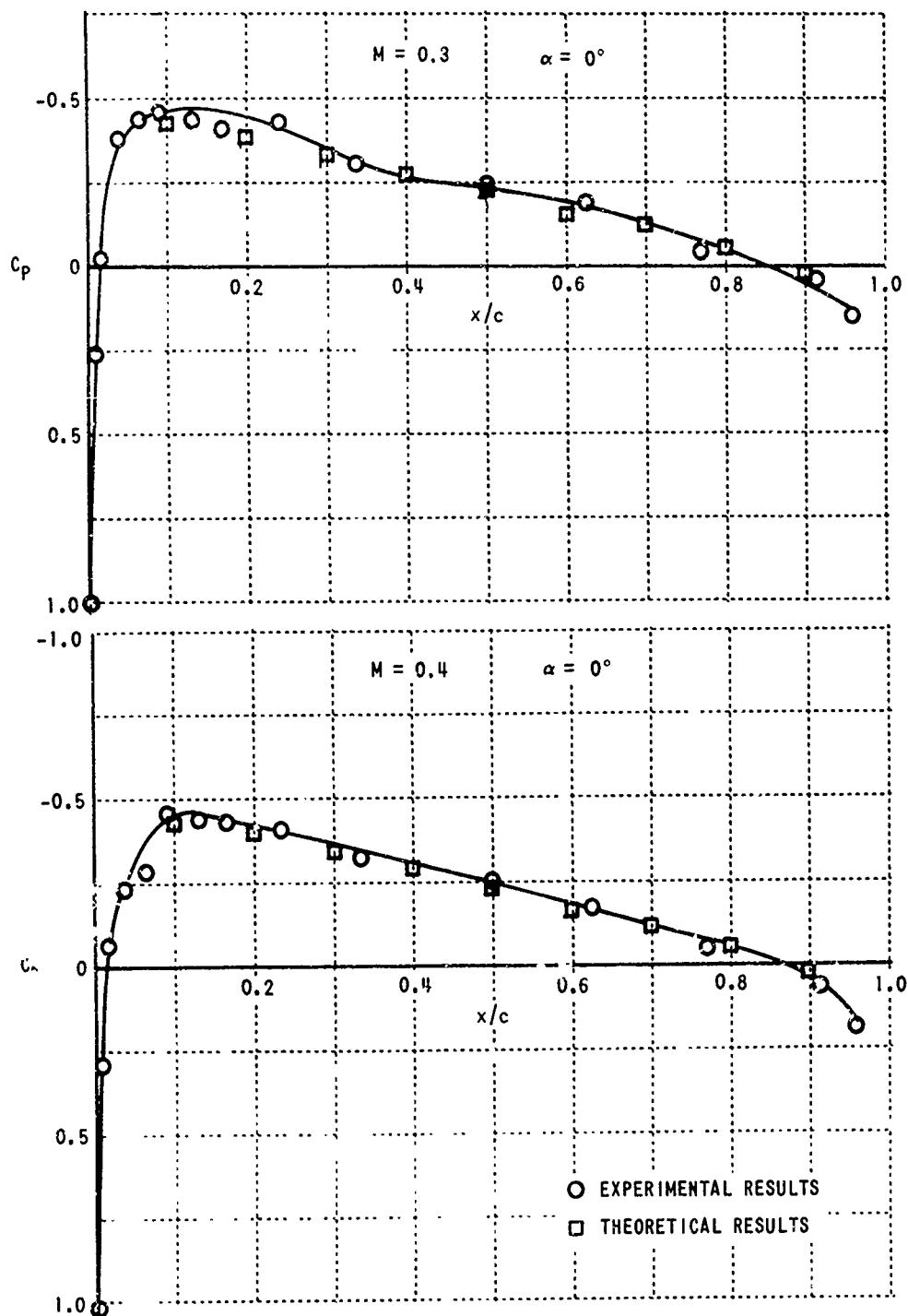


Figure 3. COMPARISON OF EXPERIMENTAL PRESSURE DISTRIBUTIONS (REFERENCE 4) WITH THEORETICAL RESULTS AT MACH NUMBERS 0.3 AND 0.4 TO ILLUSTRATE THICKNESS EFFECTS.

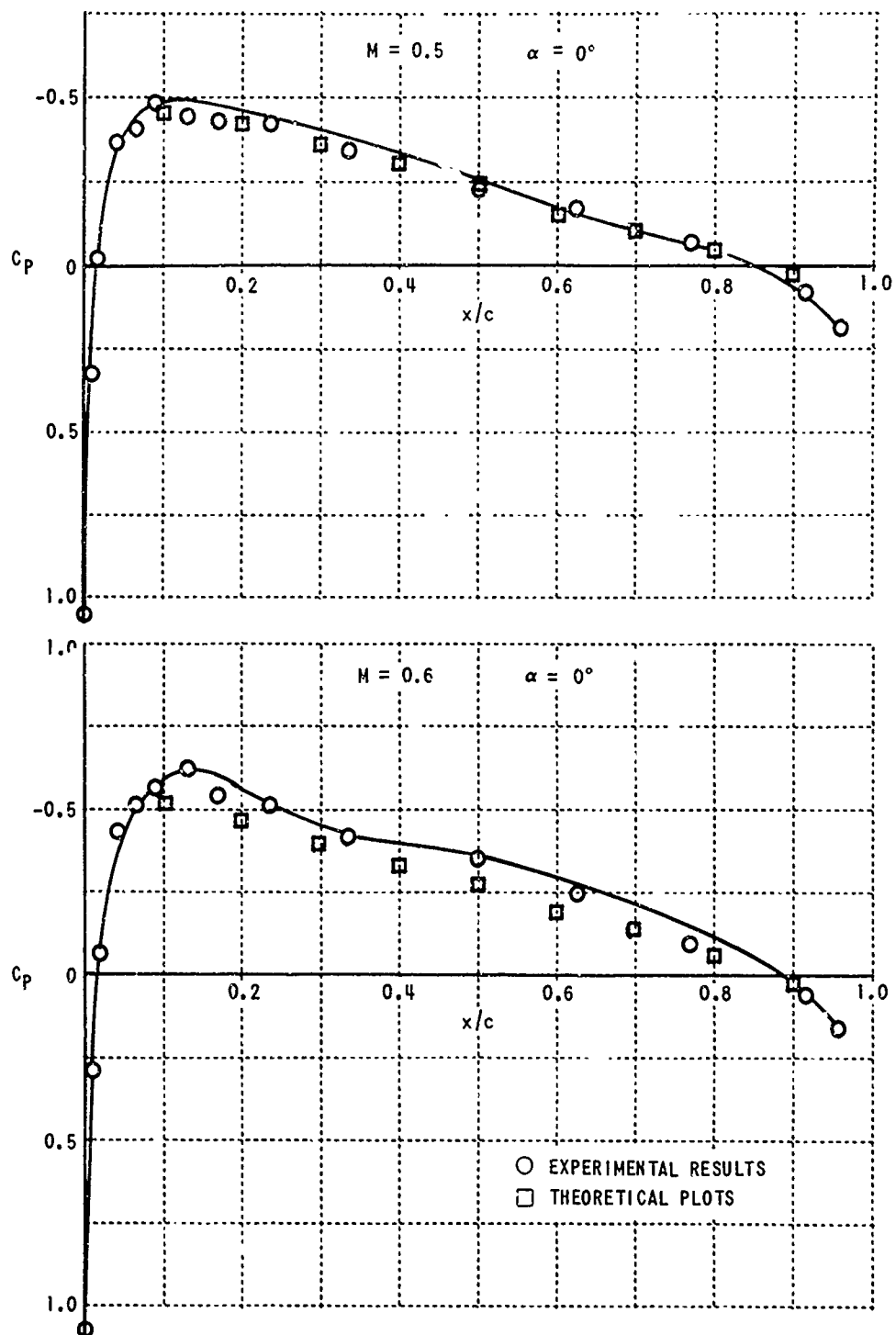


Figure 4. COMPARISON OF EXPERIMENTAL PRESSURE DISTRIBUTIONS (REFERENCE 4) WITH THEORETICAL RESULTS AT MACH NUMBERS 0.5 AND 0.6 TO ILLUSTRATE THICKNESS EFFECTS.

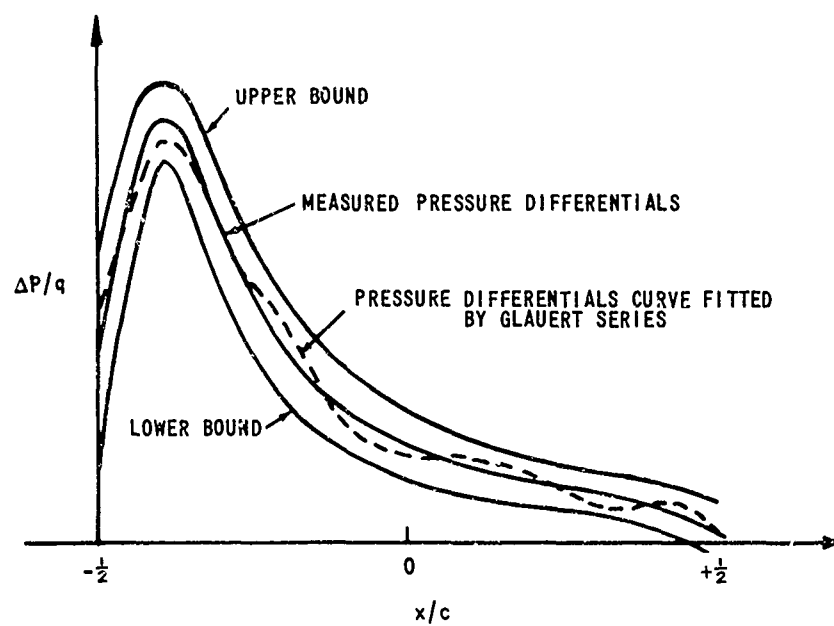


Figure 5. SCHEMATIC OF UPPER AND LOWER BOUNDS FOR MEASURED PRESSURE DIFFERENTIALS.

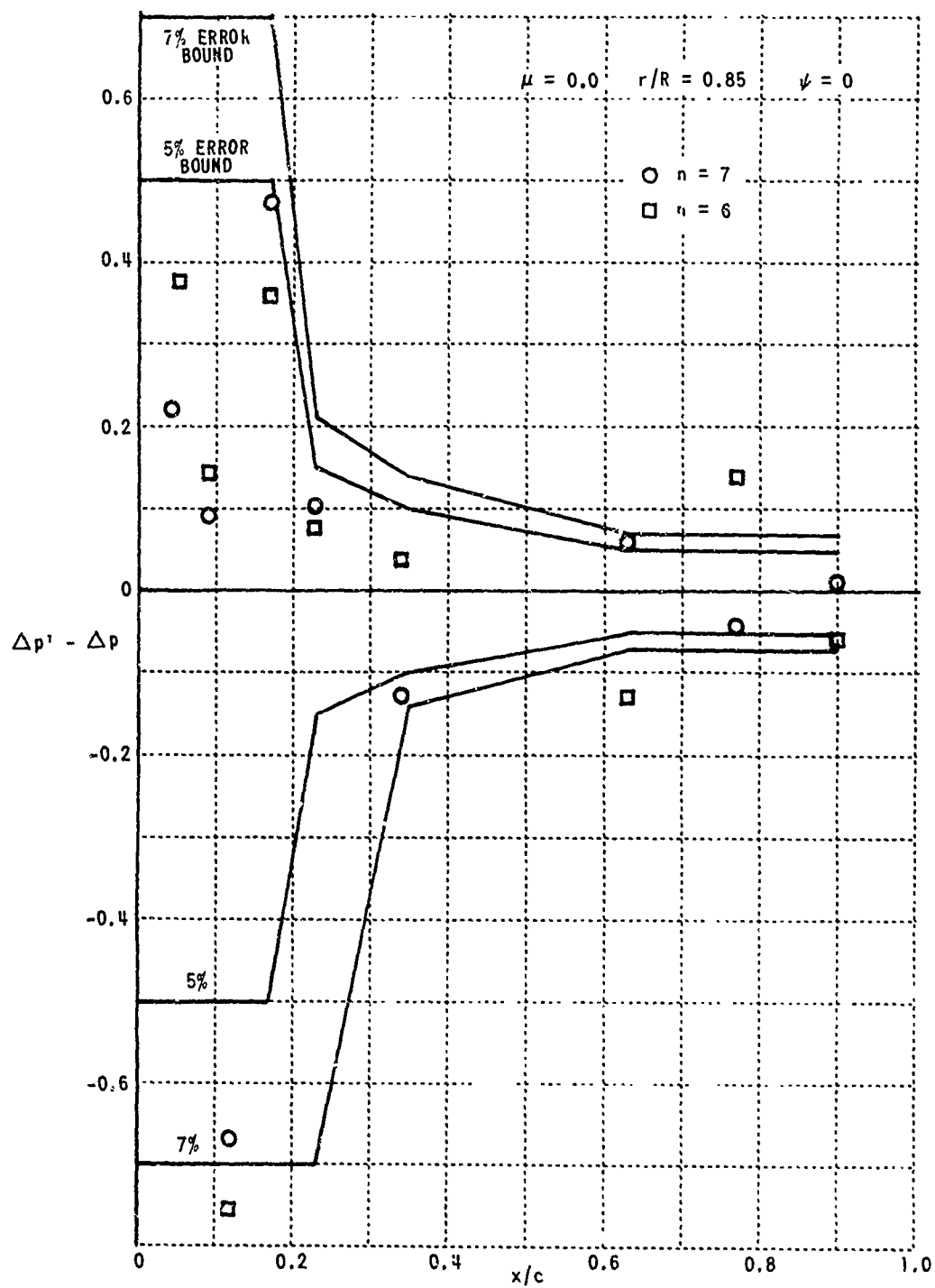


FIGURE 6. EFFECTS OF NUMBER,  $n$ , OF GLAUERT COEFFICIENTS ON THE DIFFERENCE BETWEEN COMPUTED AND MEASURED PRESSURES FOR UH-1A FLIGHT DATA AT  $\mu = 0$ ,  $r/R = 0.85$ , AND  $\psi = 0$ .

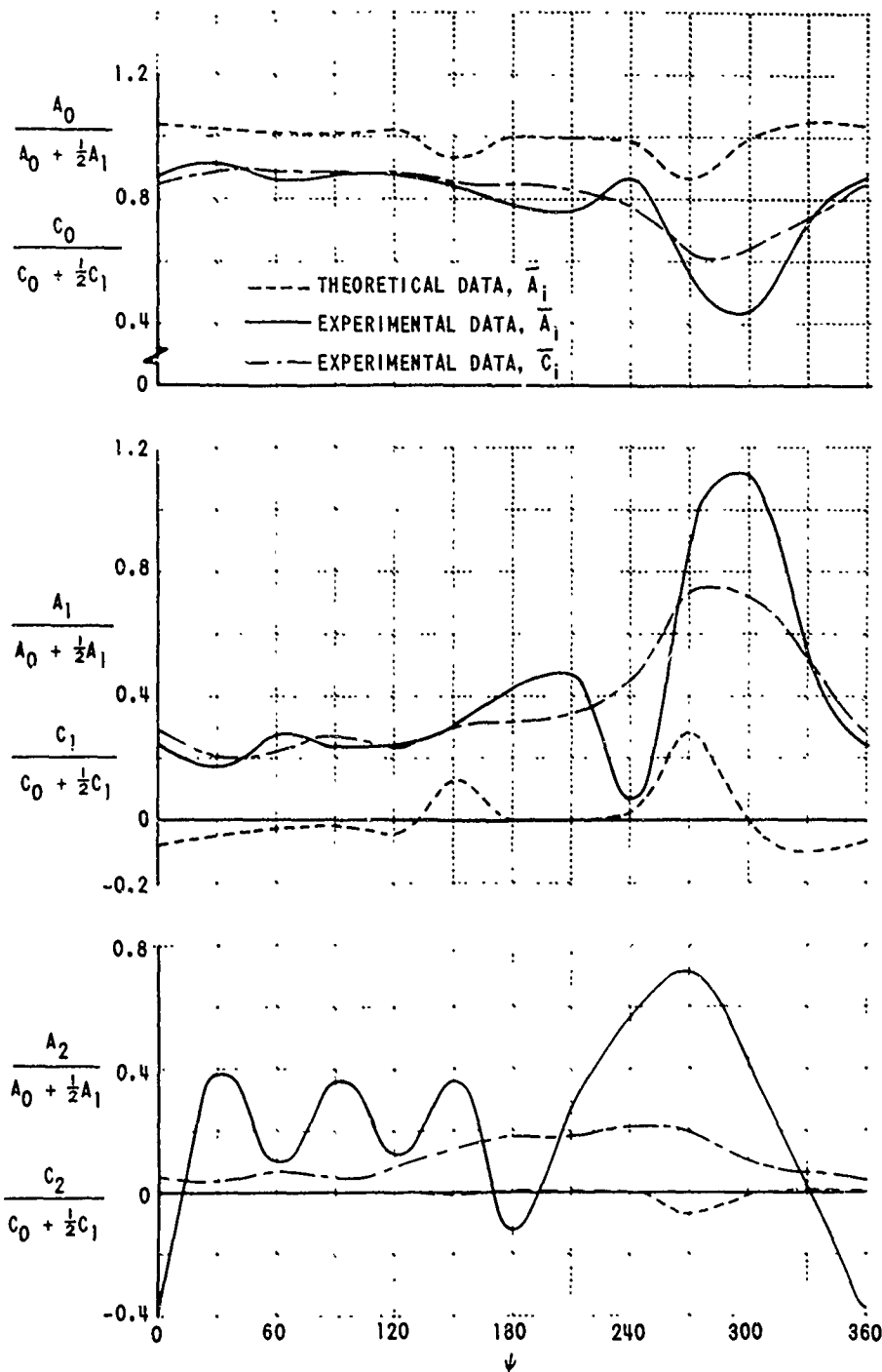


Figure 7. COMPARISON OF THEORETICAL NONDIMENSIONAL GLAUERT COEFFICIENTS WITH FLIGHT DATA FOR H-34 AT  $\mu = 0.18$ ,  $r/R = 0.40$ .

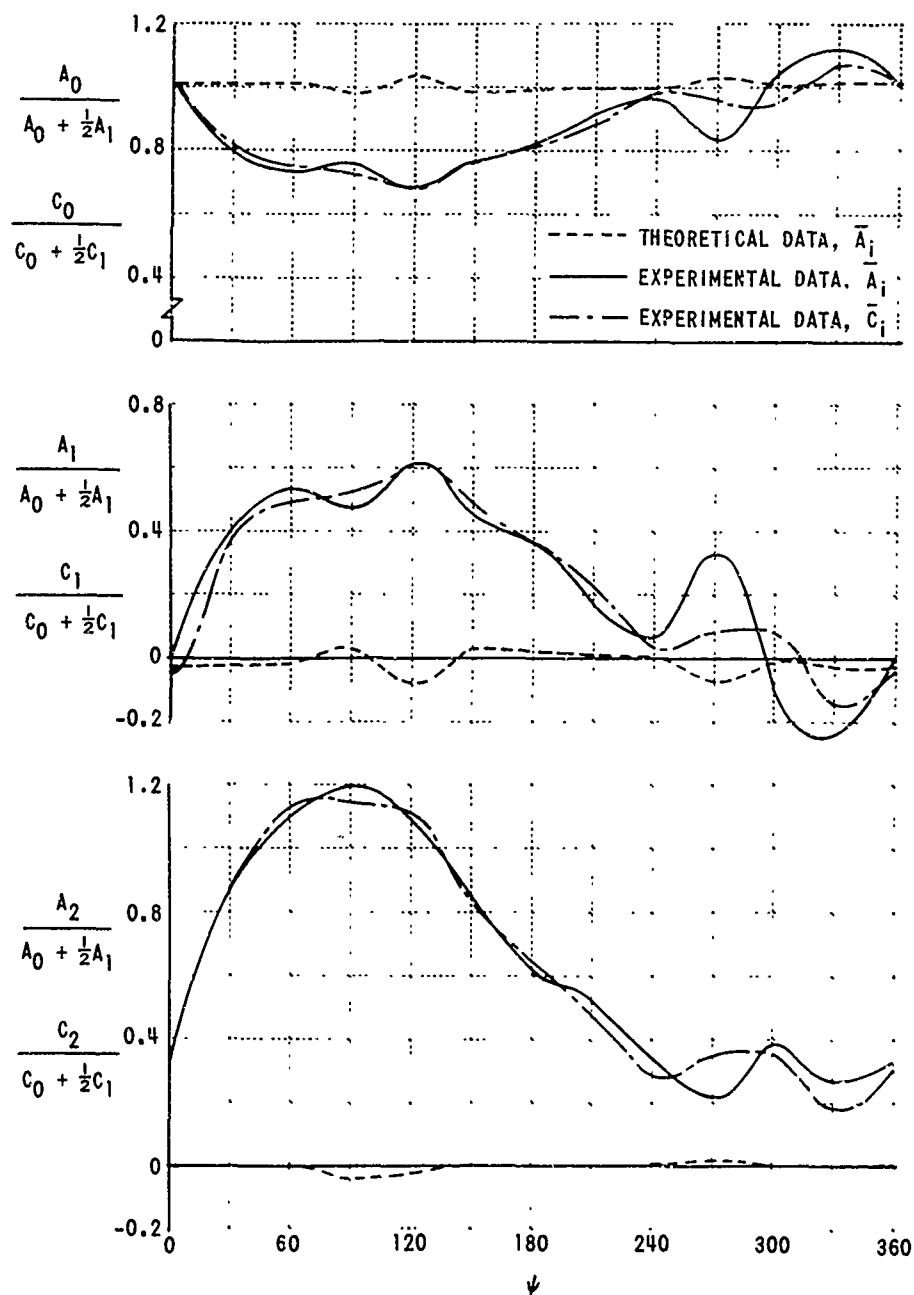


Figure 8. COMPARISON OF THEORETICAL NONDIMENSIONAL GLAUERT COEFFICIENTS WITH FLIGHT DATA FOR H-34 AT  $\mu = 0.18$ ,  $r/R = 0.85$ .

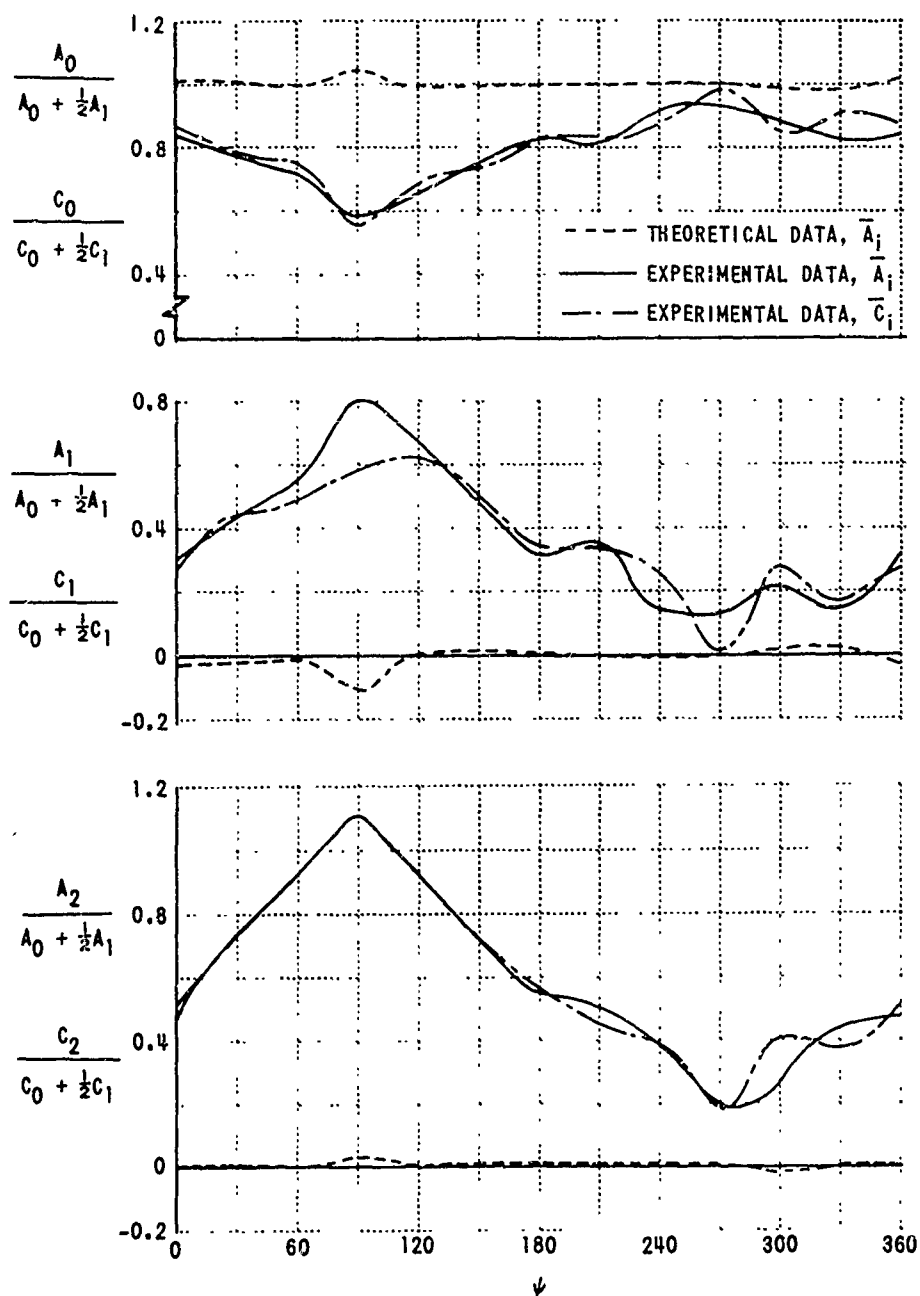


Figure 9. COMPARISON OF THEORETICAL NONDIMENSIONAL GLAUERT COEFFICIENTS WITH FLIGHT DATA FOR H-34 AT  $\mu = 0.18$ ,  $r/R = 0.90$ .



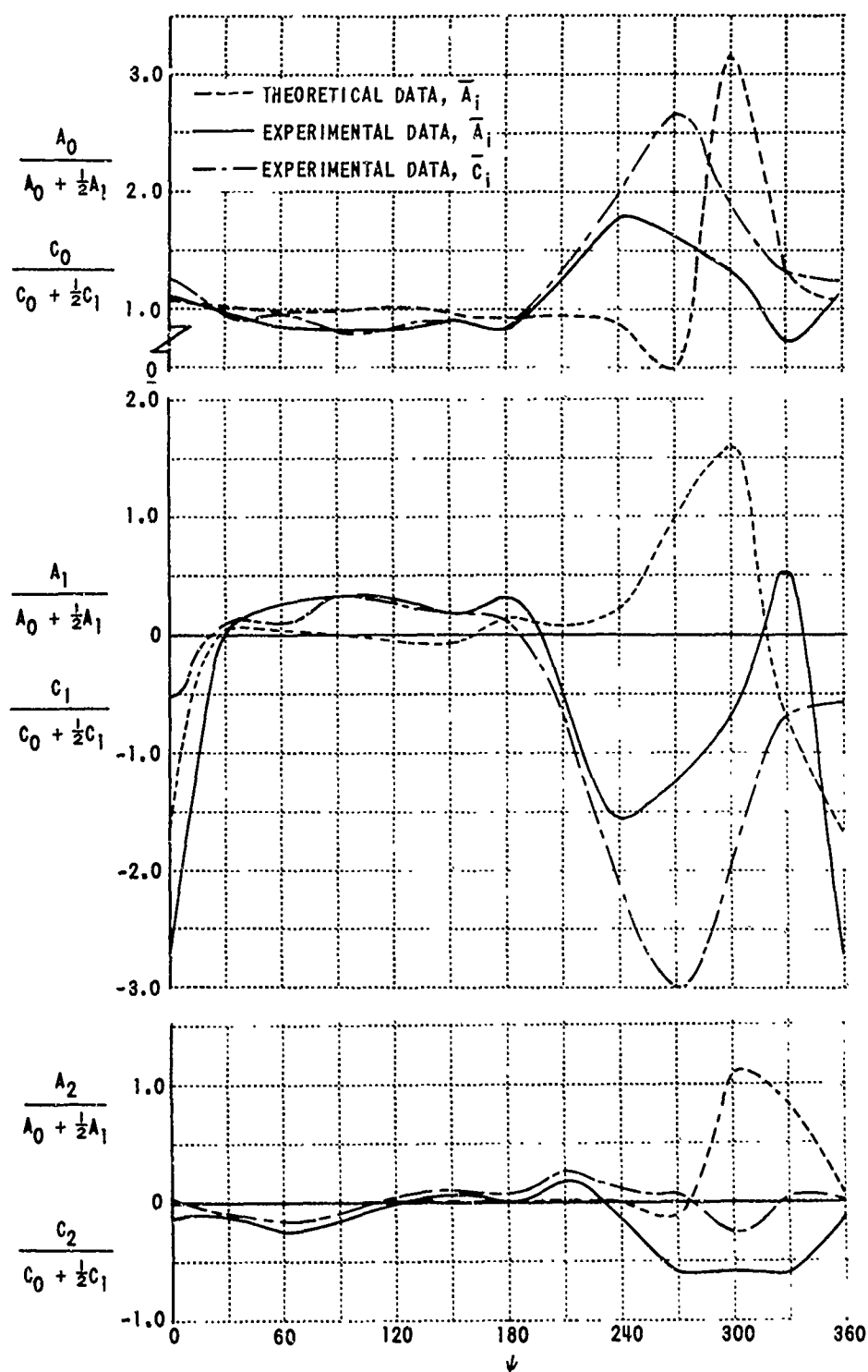


Figure 10. COMPARISON OF THEORETICAL NONDIMENSIONAL GLAUERT COEFFICIENTS WITH FLIGHT DATA FOR H-34 AT  $\mu = 0.29$ ,  $r/R = 0.40$ .

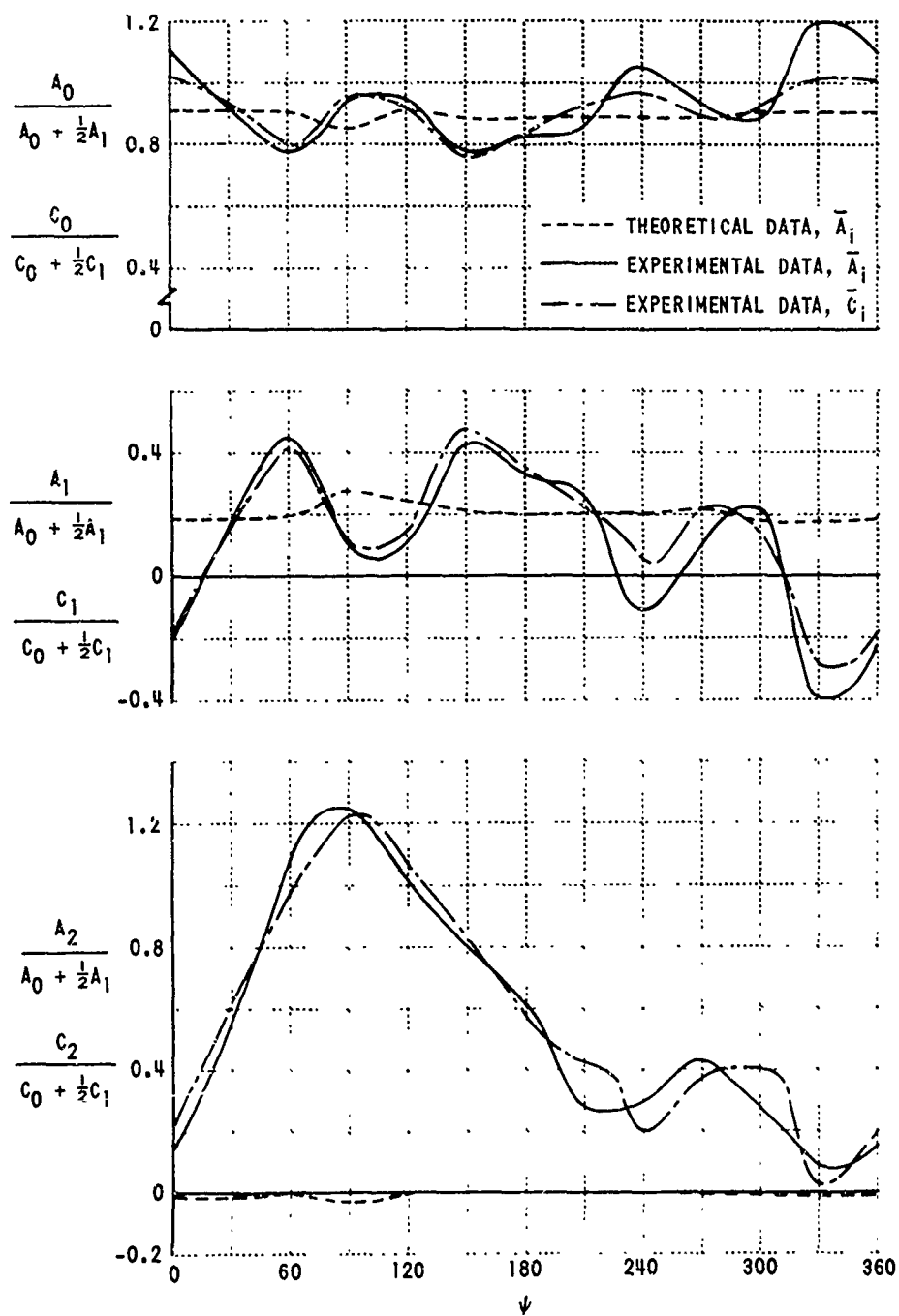


Figure 11. COMPARISON OF THEORETICAL NONDIMENSIONAL GLAUERT COEFFICIENTS WITH FLIGHT DATA FOR H-34 AT  $\mu = 0.29$ ,  $r/R = 0.85$ .

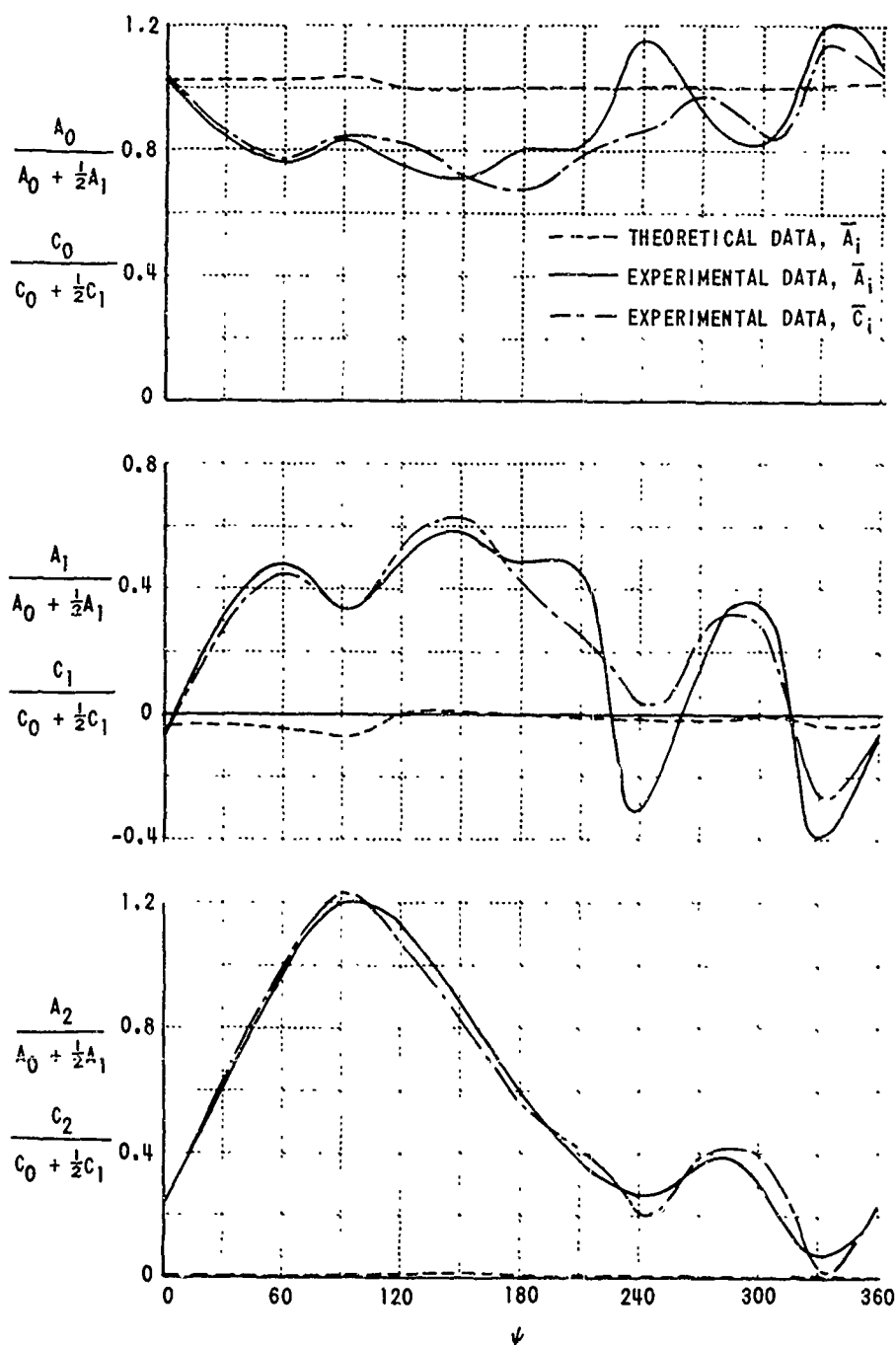


Figure 12. COMPARISON OF THEORETICAL NONDIMENSIONAL GLAUERT COEFFICIENTS WITH FLIGHT DATA FOR H-34 AT  $\mu = 0.29$ ,  $r/R = 0.90$ .

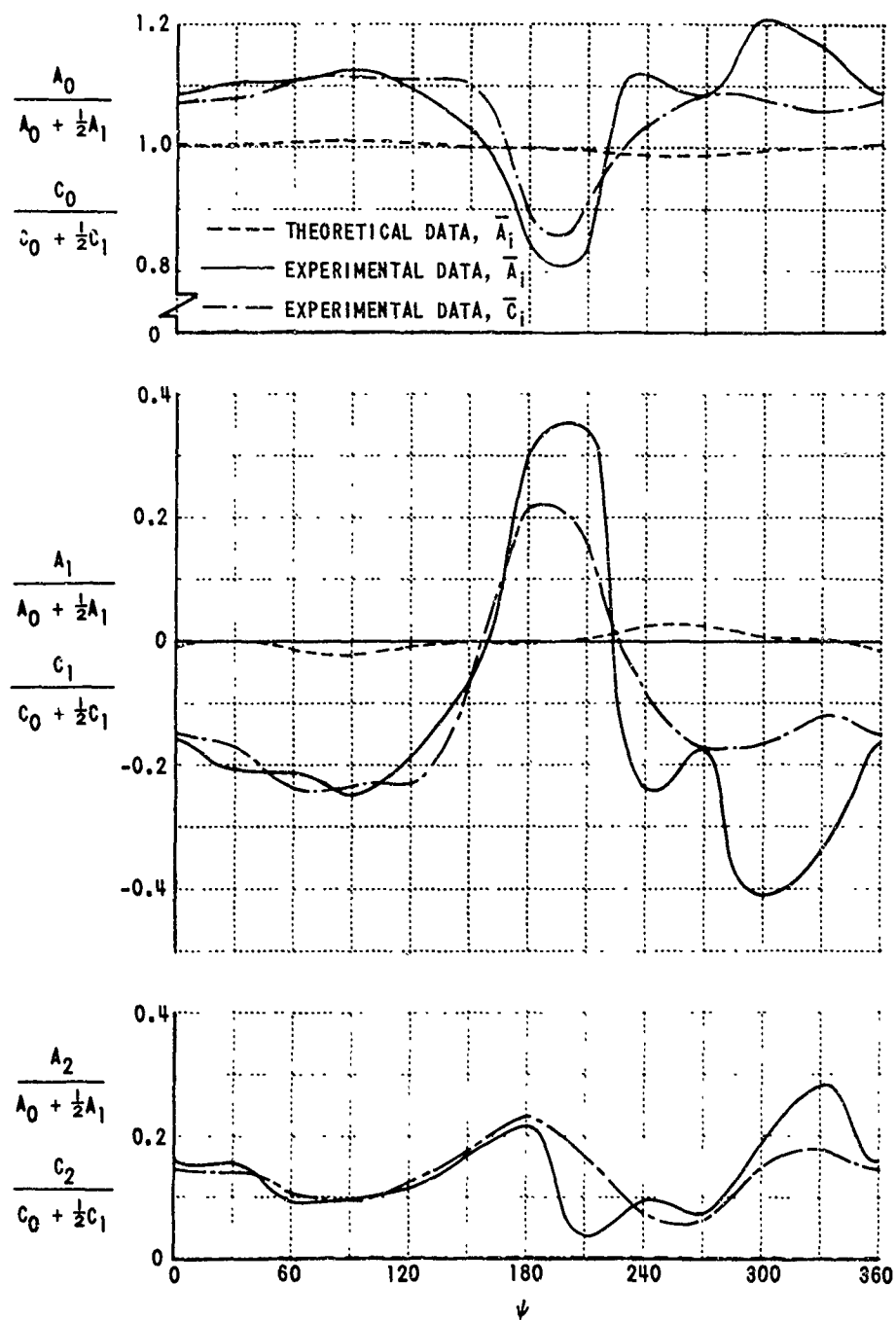


Figure 13. COMPARISON OF THEORETICAL NONDIMENSIONAL GLAUERT COEFFICIENTS WITH FLIGHT DATA FOR UH-1A AT  $\mu = 0.08$ ,  $r/R = 0.40$ .

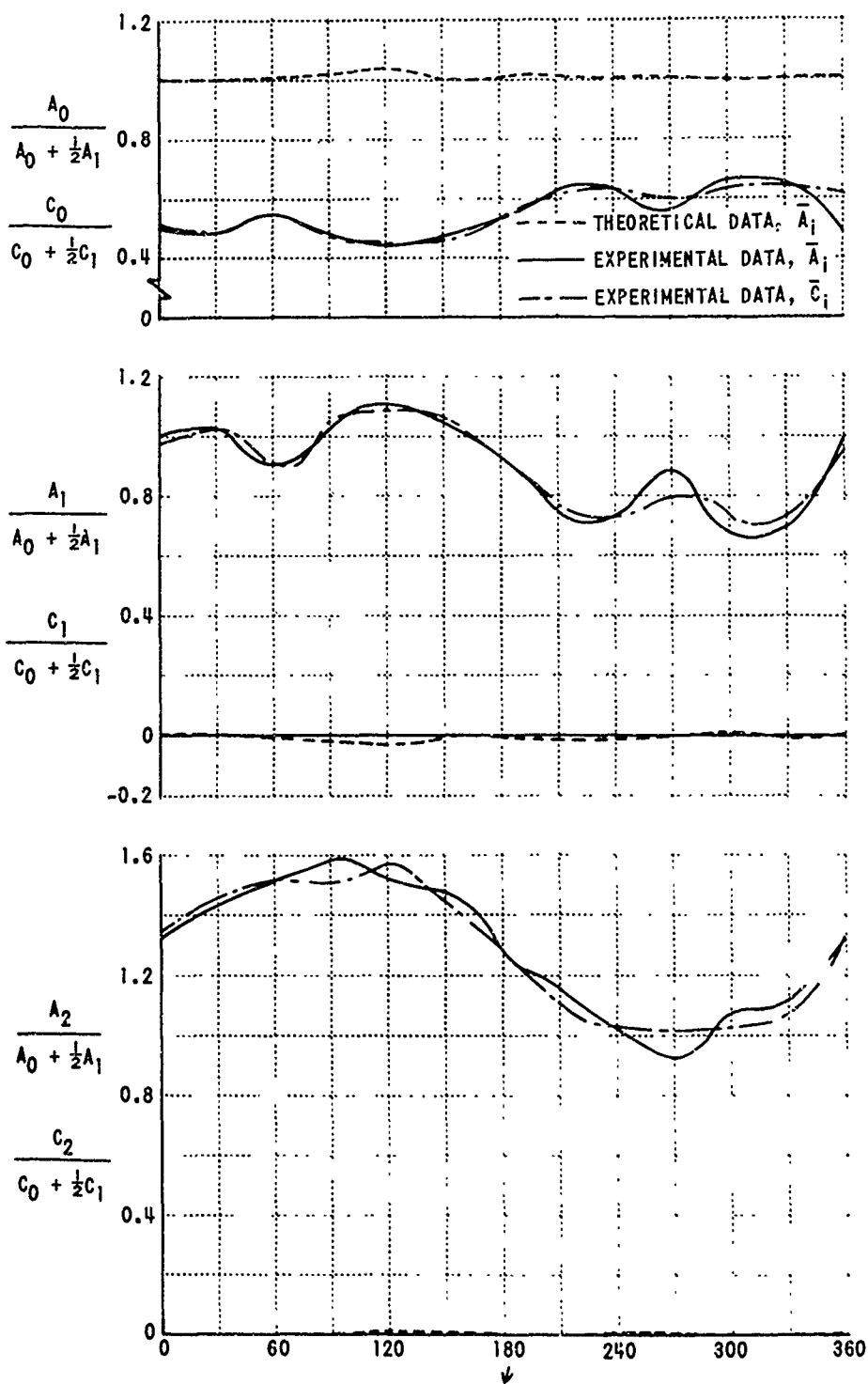


Figure 14. COMPARISON OF THEORETICAL NONDIMENSIONAL GLAUERT COEFFICIENTS WITH FLIGHT DATA FOR UH-1A AT  $\mu = 0.08$ ,  $r/R = 0.85$ .

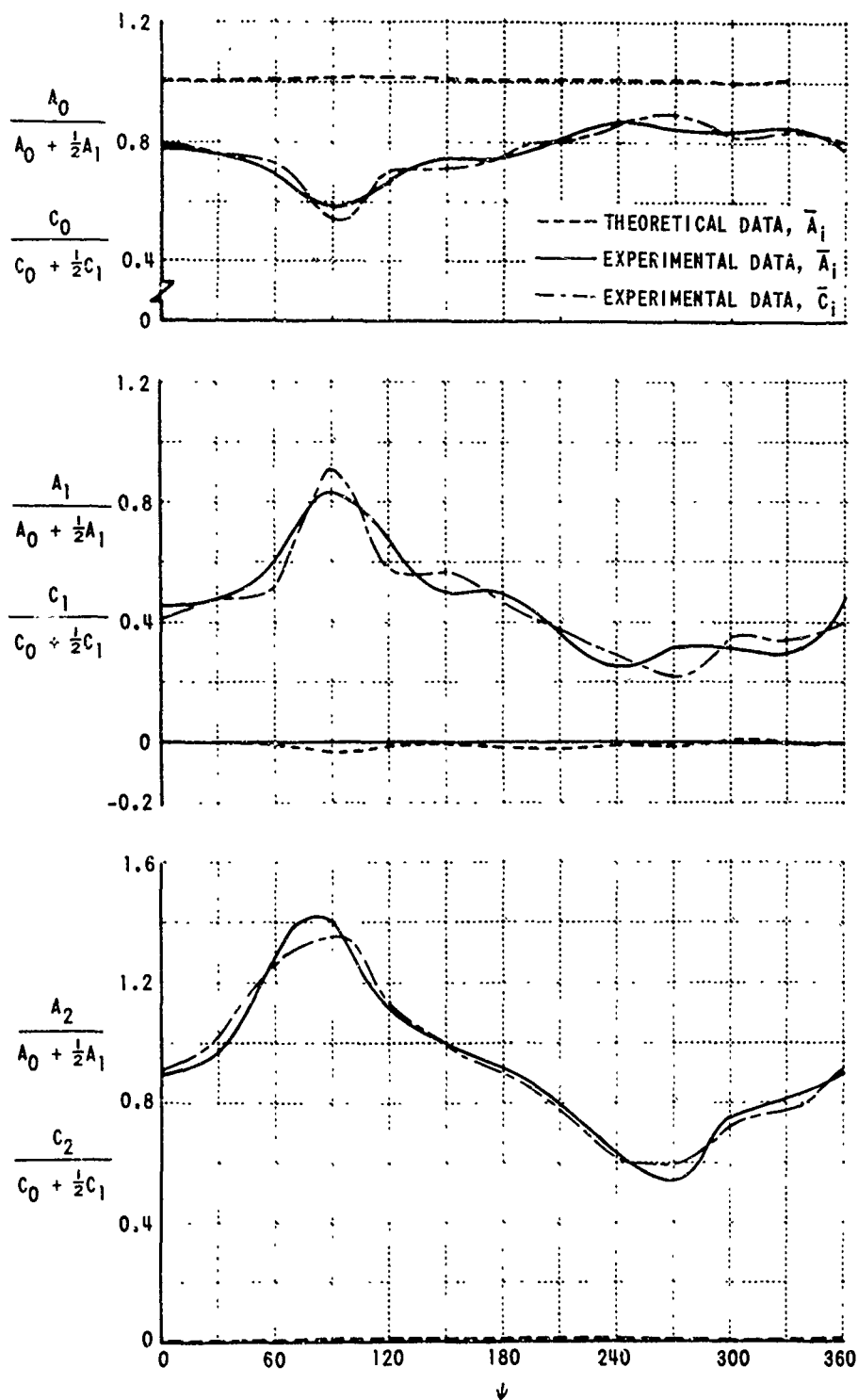


Figure 15. COMPARISON OF THEORETICAL NONDIMENSIONAL GLAUERT COEFFICIENTS WITH FLIGHT DATA FOR UH-1A AT  $\mu = 0.08$ ,  $r/R = 0.90$ .

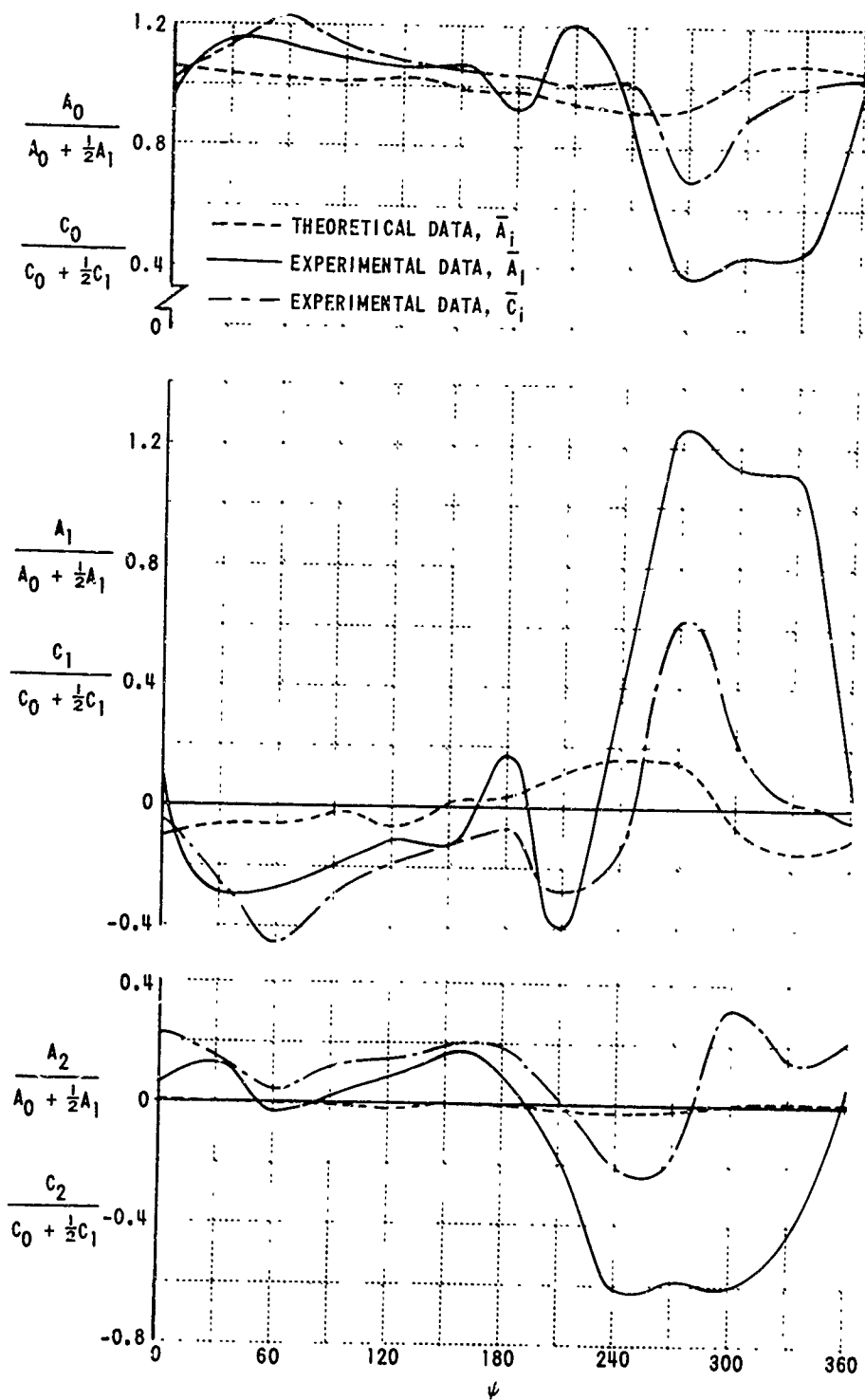


Figure 16. COMPARISON OF THEORETICAL NONDIMENSIONAL GLAUERT COEFFICIENTS WITH FLIGHT DATA FOR UH-1A AT  $\mu = 0.26$ ,  $r/R = 0.40$ .

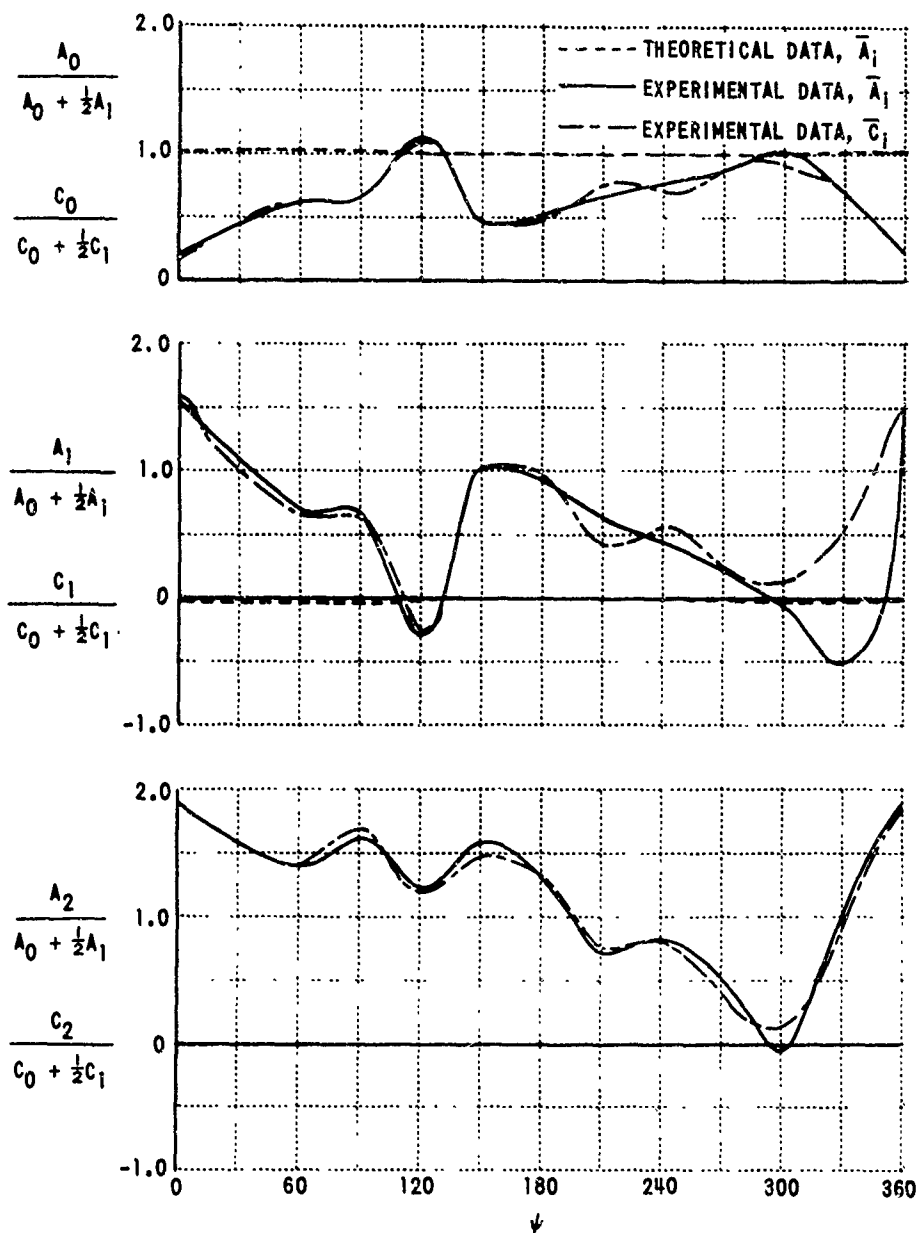


Figure 17. COMPARISON OF THEORETICAL NONDIMENSIONAL GLAUERT COEFFICIENTS WITH FLIGHT DATA FOR UH-1A AT  $\mu = 0.26$ ,  $r/R = 0.85$ .



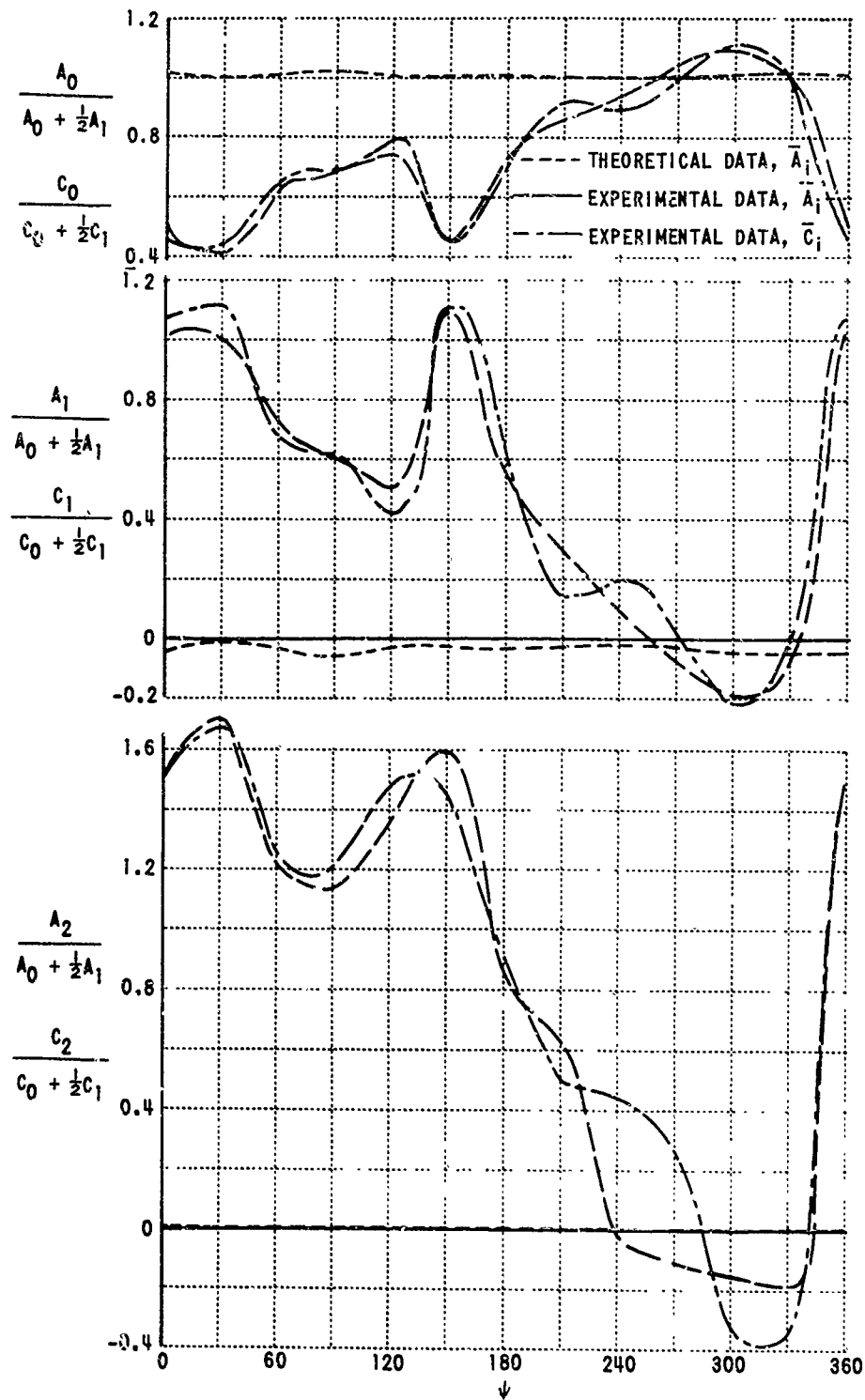


Figure 18. COMPARISON OF THEORETICAL NONDIMENSIONAL GLAUERT COEFFICIENTS WITH FLIGHT DATA FOR UH-1A AT  $\mu = 0.26$ ,  $r/R = 0.90$ .

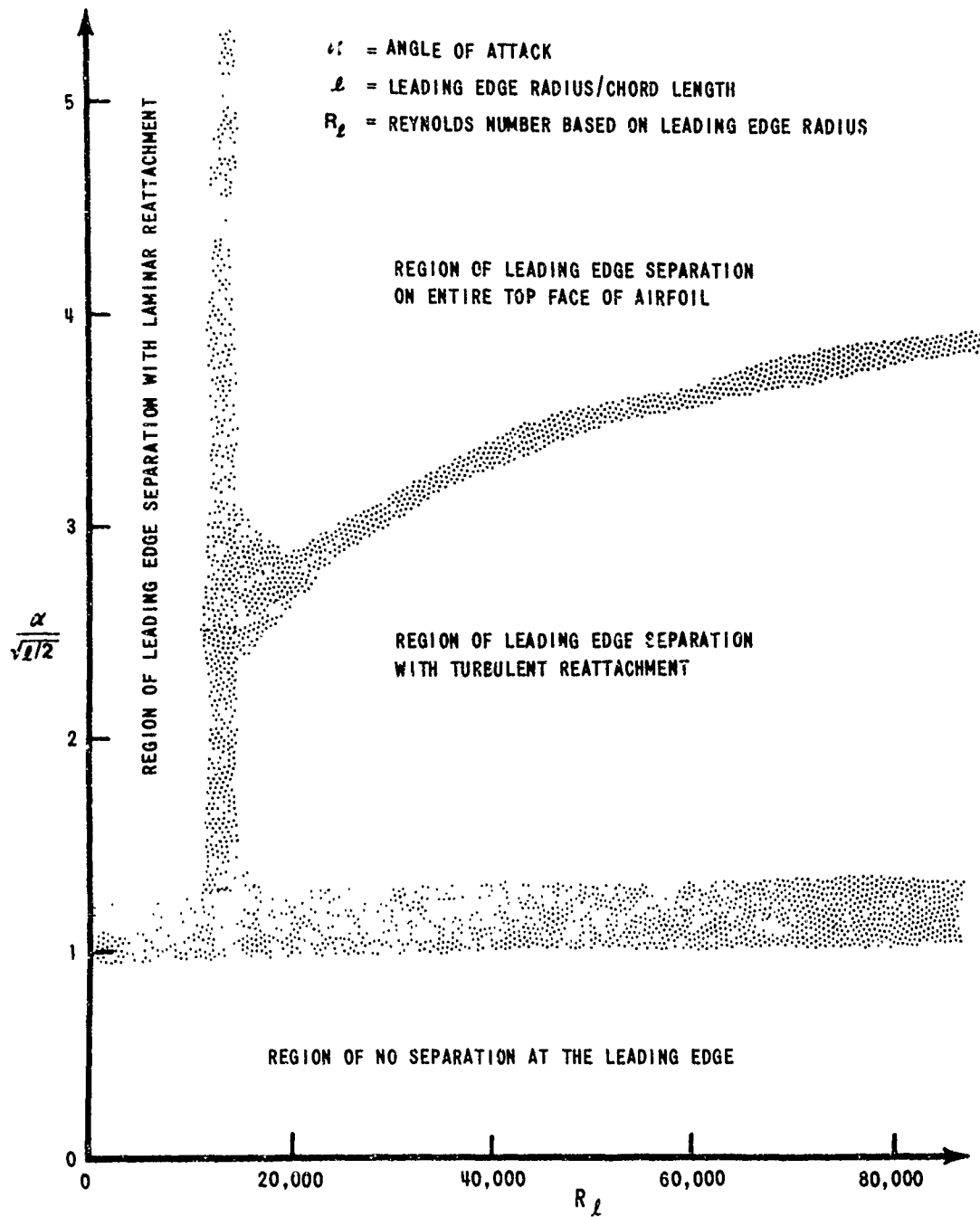


Figure 19. AIRFOIL LEADING EDGE SEPARATION CHARACTERISTICS (FROM REFERENCE 13).

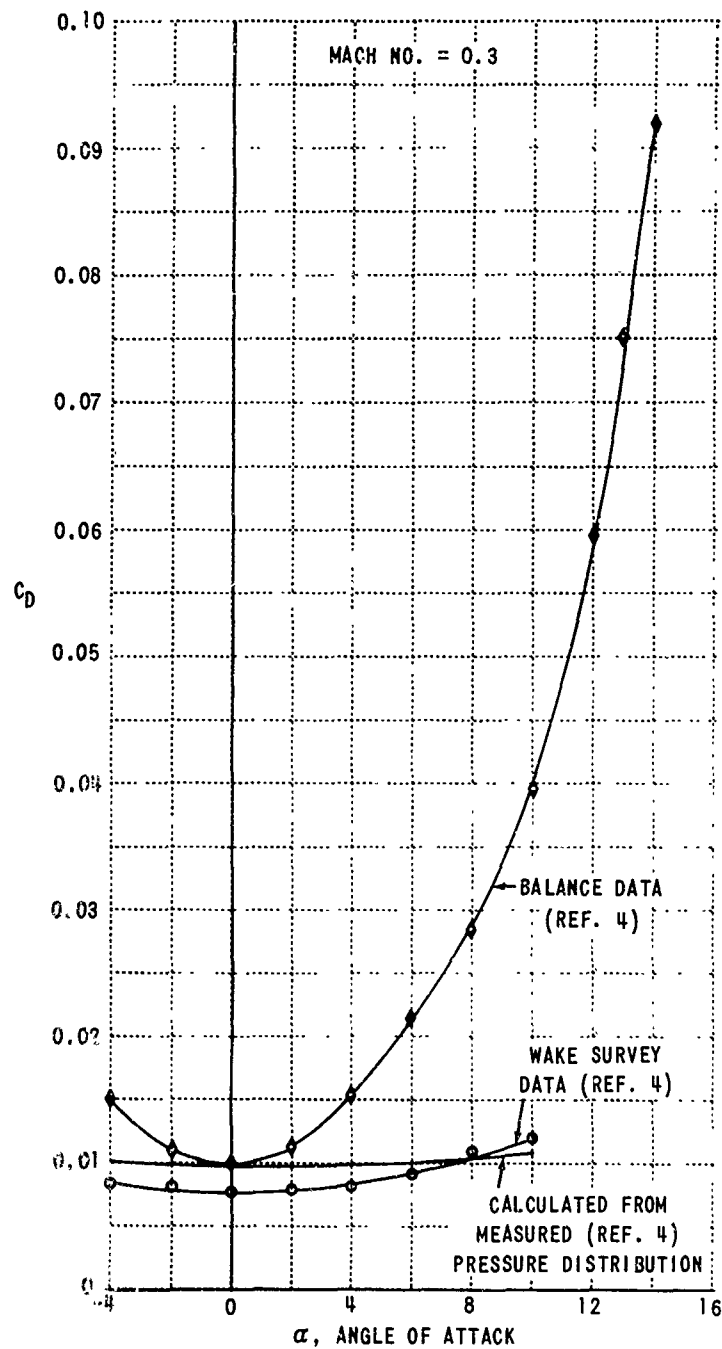


Figure 20. COMPARISON OF MEASURED AND CALCULATED DRAG COEFFICIENTS FOR NACA 0012 AIRFOIL SECTION AT MACH NUMBER 0.3.

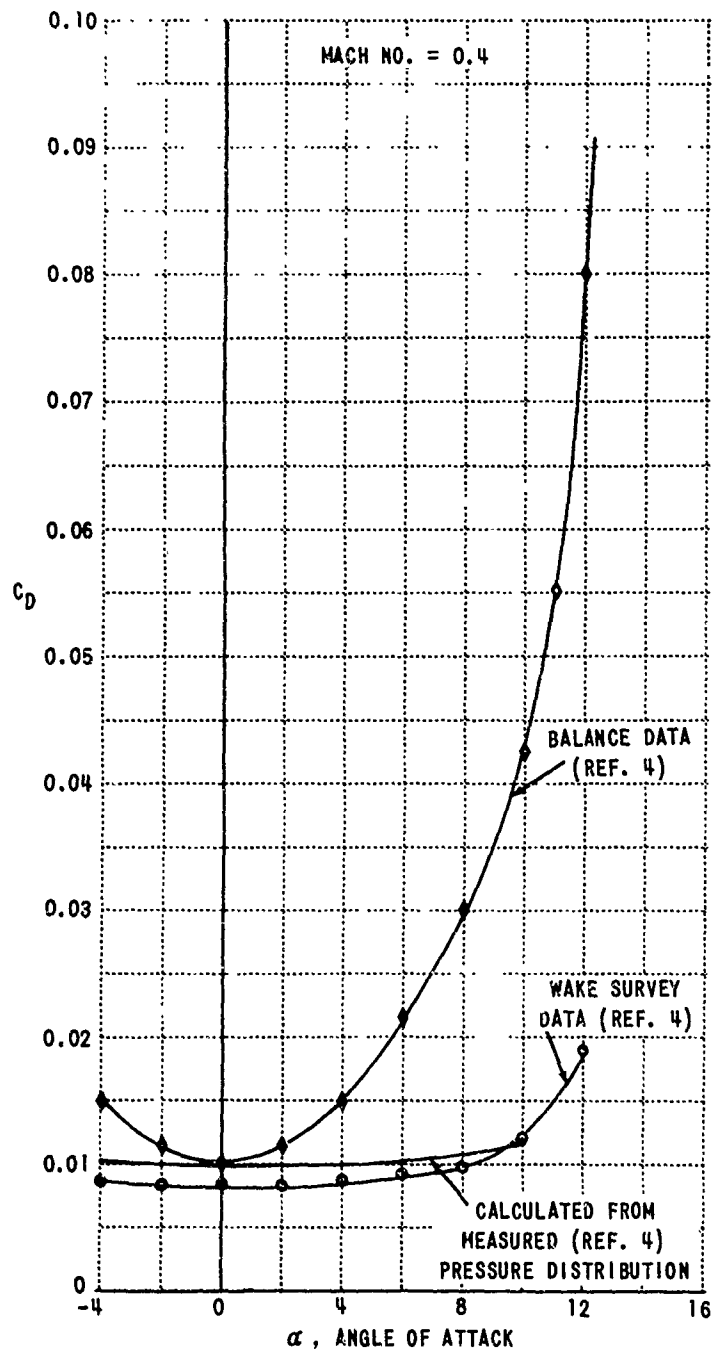


Figure 21. COMPARISON OF MEASURED AND CALCULATED DRAG COEFFICIENTS FOR NACA 0012 AIRFOIL SECTION AT MACH NUMBER 0.4.

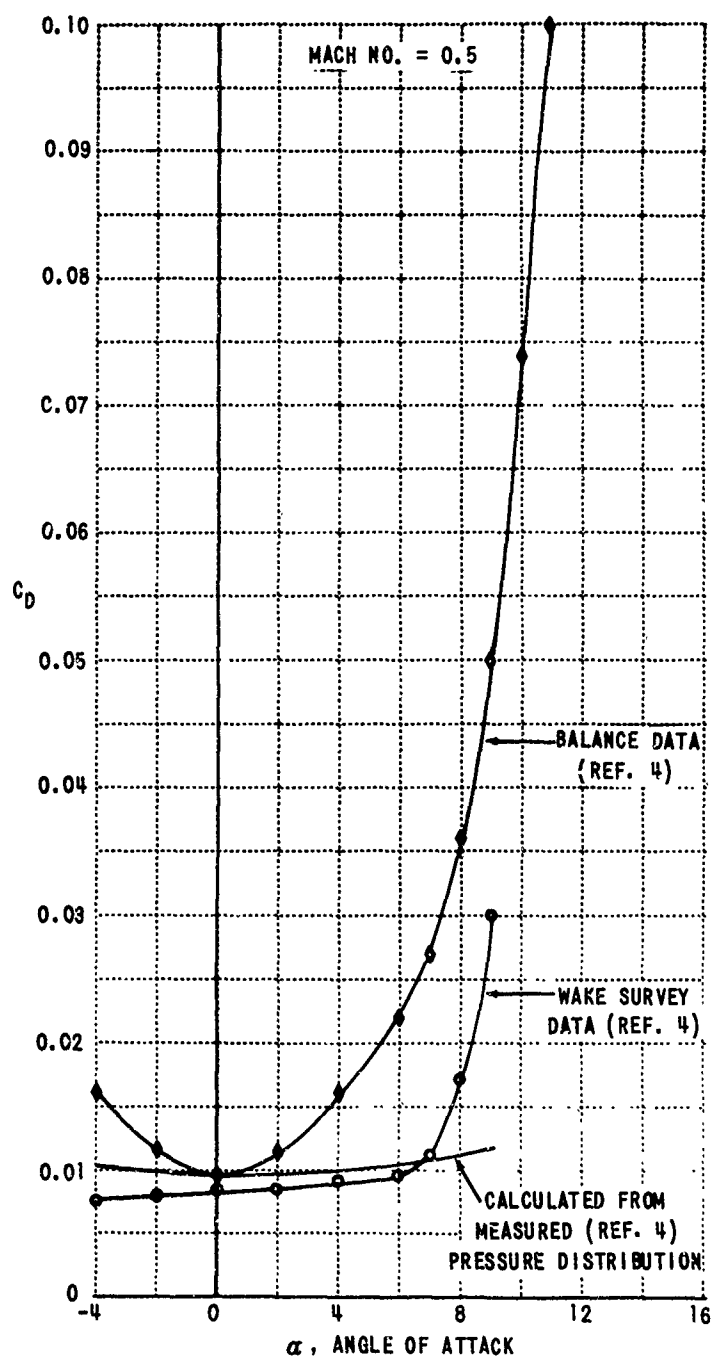


Figure 22. COMPARISON OF MEASURED AND CALCULATED DRAG COEFFICIENTS FOR NACA 0012 AIRFOIL SECTION AT MACH NUMBER 0.5.

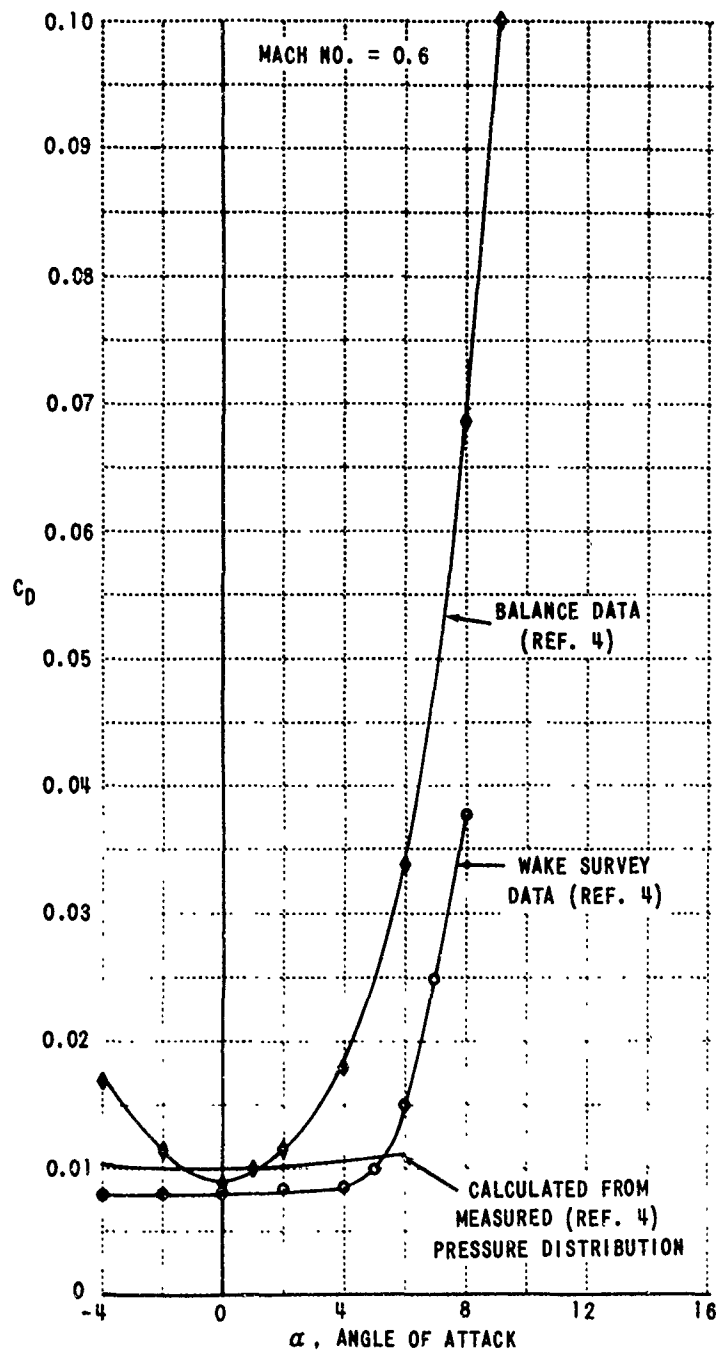


Figure 23. COMPARISON OF MEASURED AND CALCULATED DRAG COEFFICIENTS FOR NACA 0012 AIRFOIL SECTION AT MACH NUMBER 0.6.

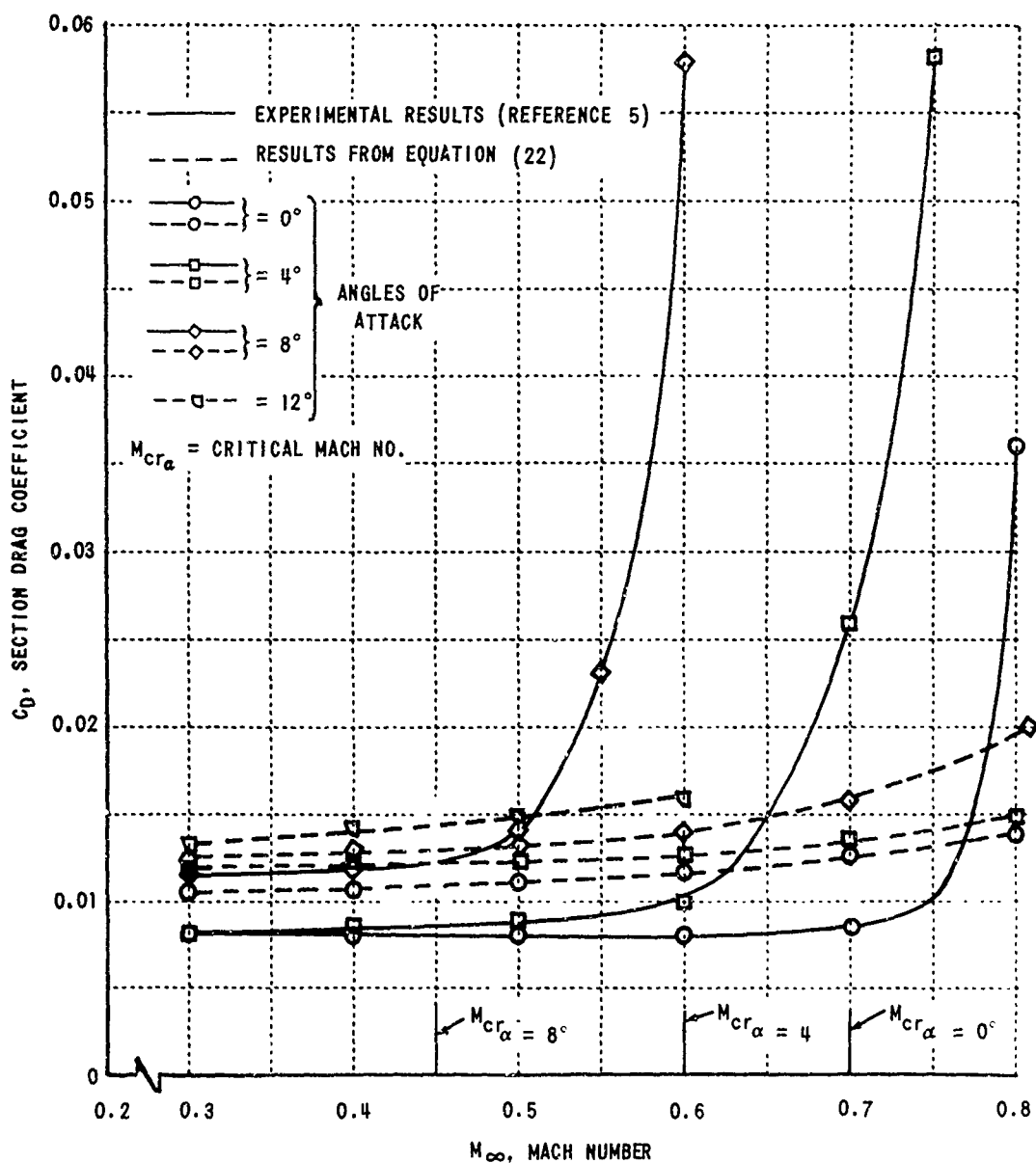


Figure 24. COMPARISON OF MEASURED AND CALCULATED DRAG COEFFICIENTS FOR NACA 0015 AIRFOIL SECTION AT MACH NUMBERS 0.3 TO 0.88.

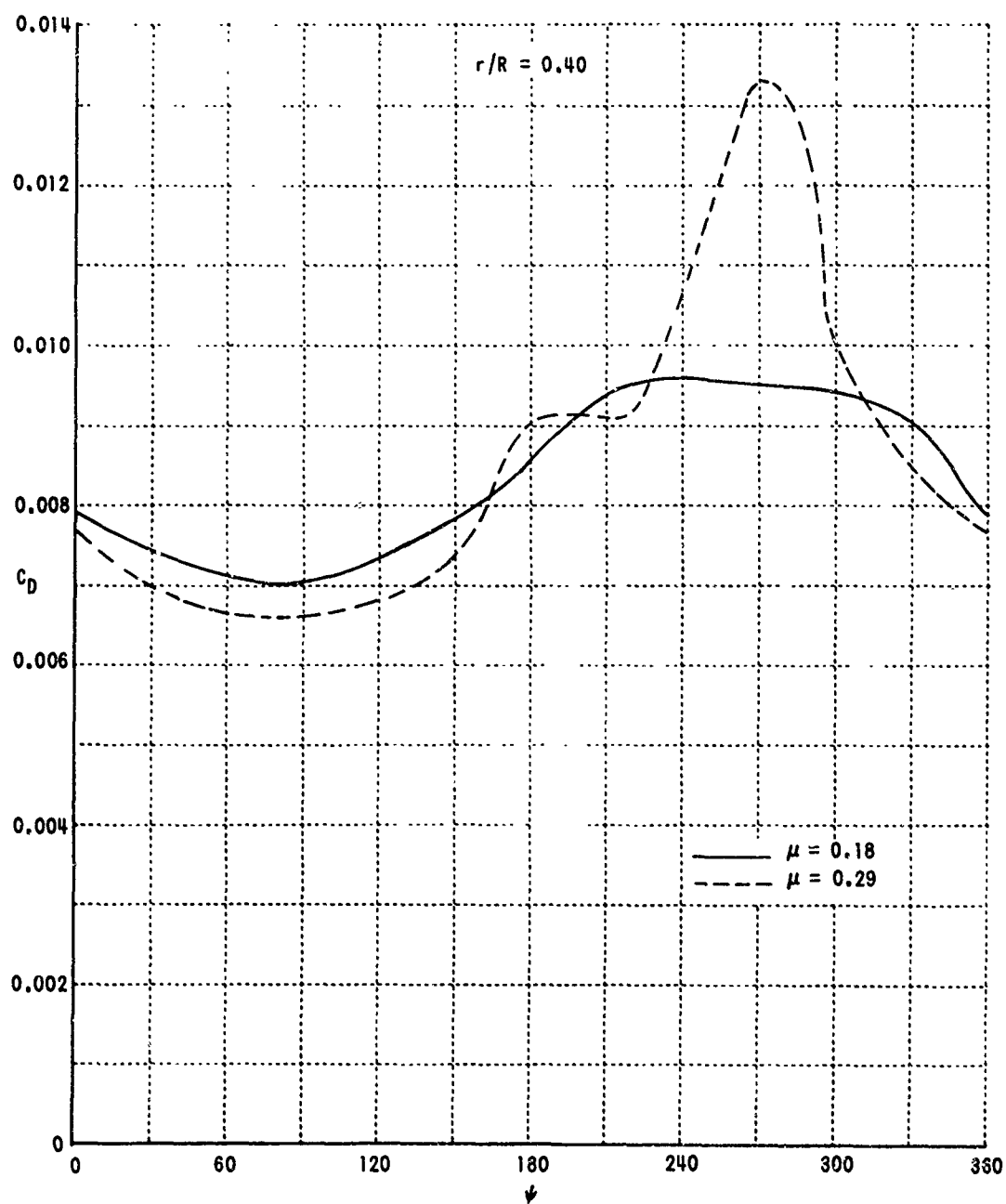


Figure 25. VARIATION OF CALCULATED DRAG COEFFICIENTS WITH AZIMUTHAL ANGLE  $\psi$  FOR H-34 AT  $r/R = 0.40$ ,  $\mu = 0.18$  AND  $0.29$ .



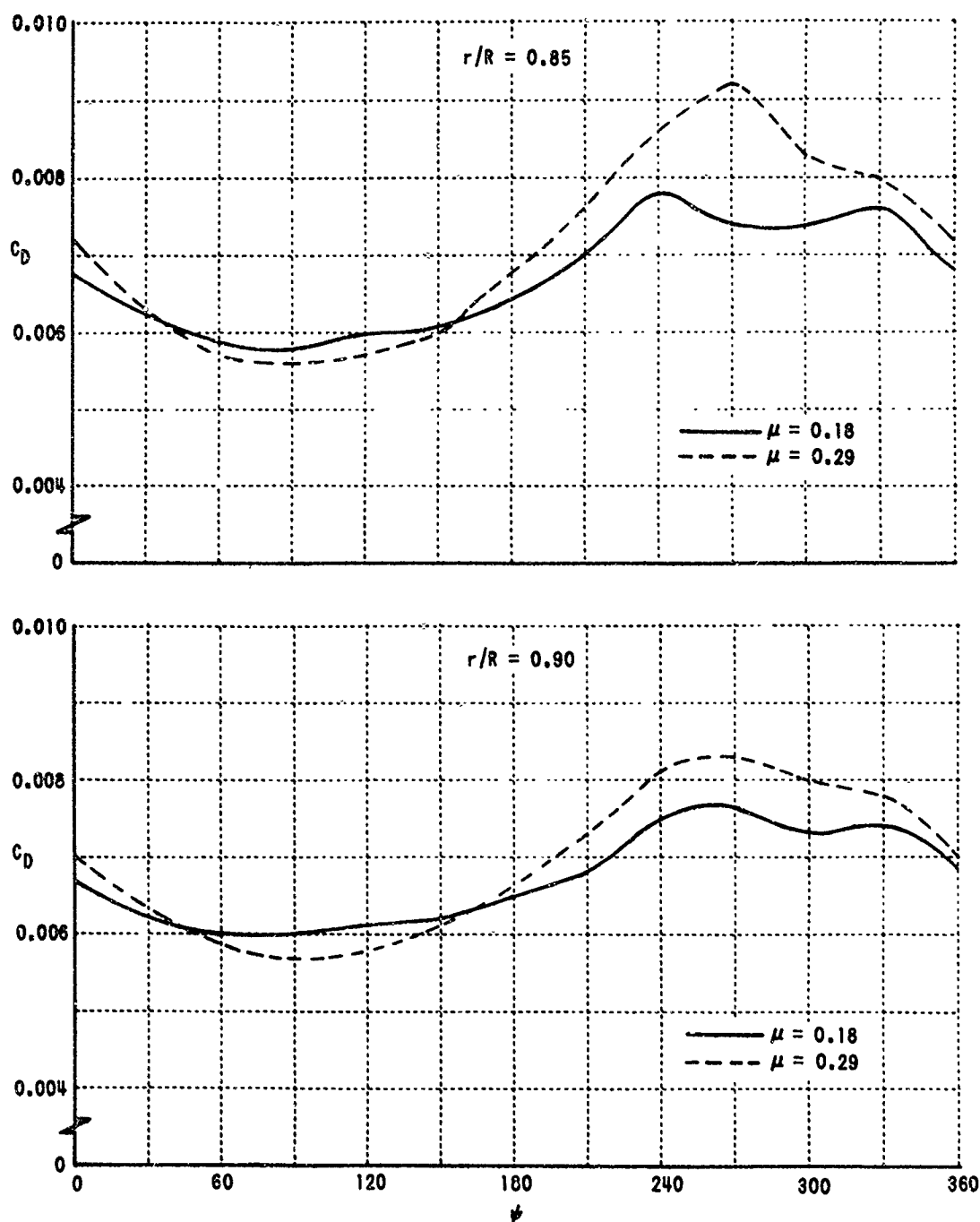


Figure 26. VARIATION OF CALCULATED DRAG COEFFICIENTS WITH AZIMUTHAL ANGLE  $\psi$  FOR H-34 AT  $r/R = 0.85$  AND  $0.90$ ,  $\mu = 0.18$  AND  $0.29$ .

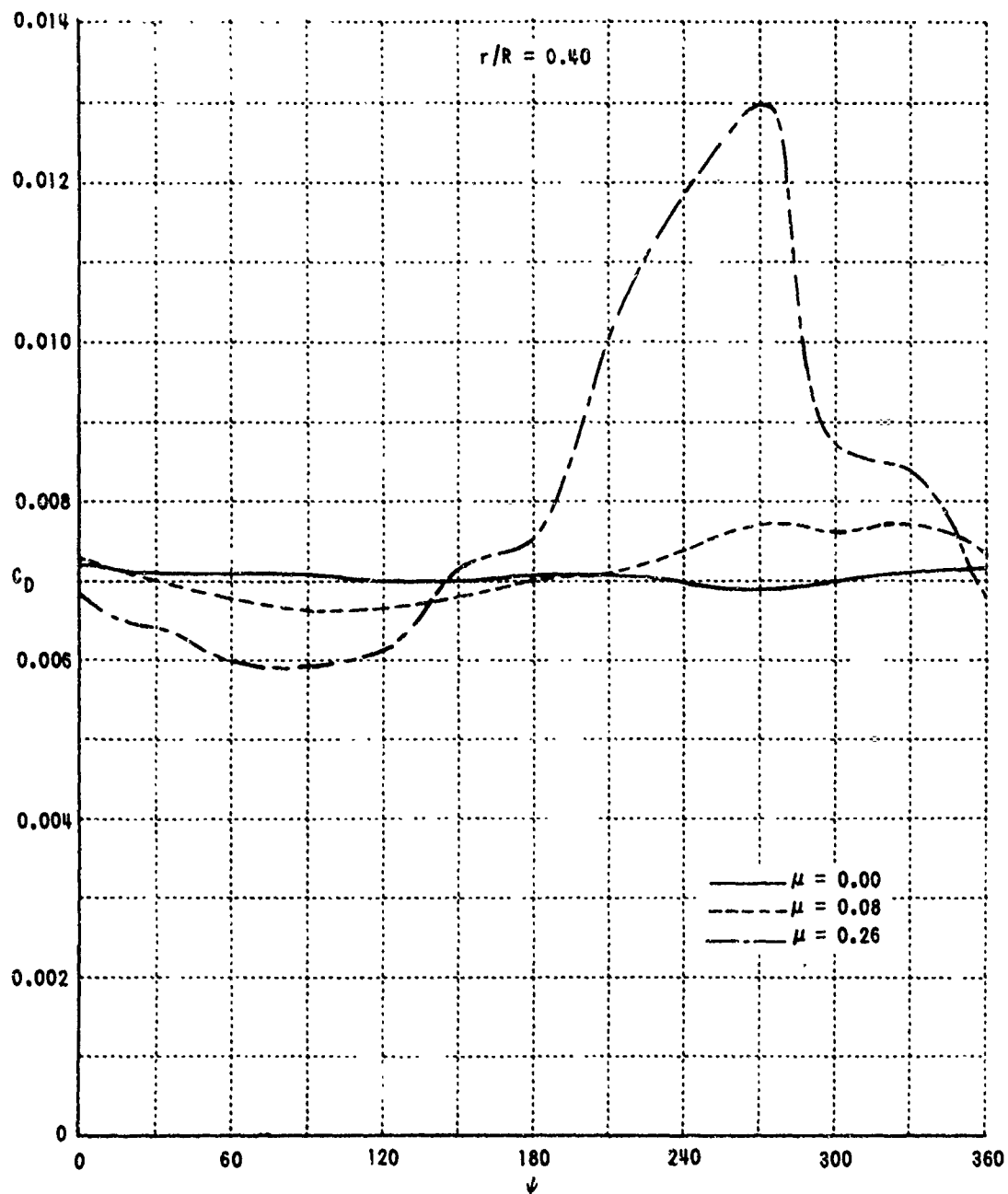


Figure 27. VARIATION OF CALCULATED DRAG COEFFICIENTS WITH AZMMUTHAL ANGLE  $\psi$  FOR UH-1A AT  $r/R = 0.40$  AND  $\mu = 0.0, 0.08$ , AND  $0.26$ .

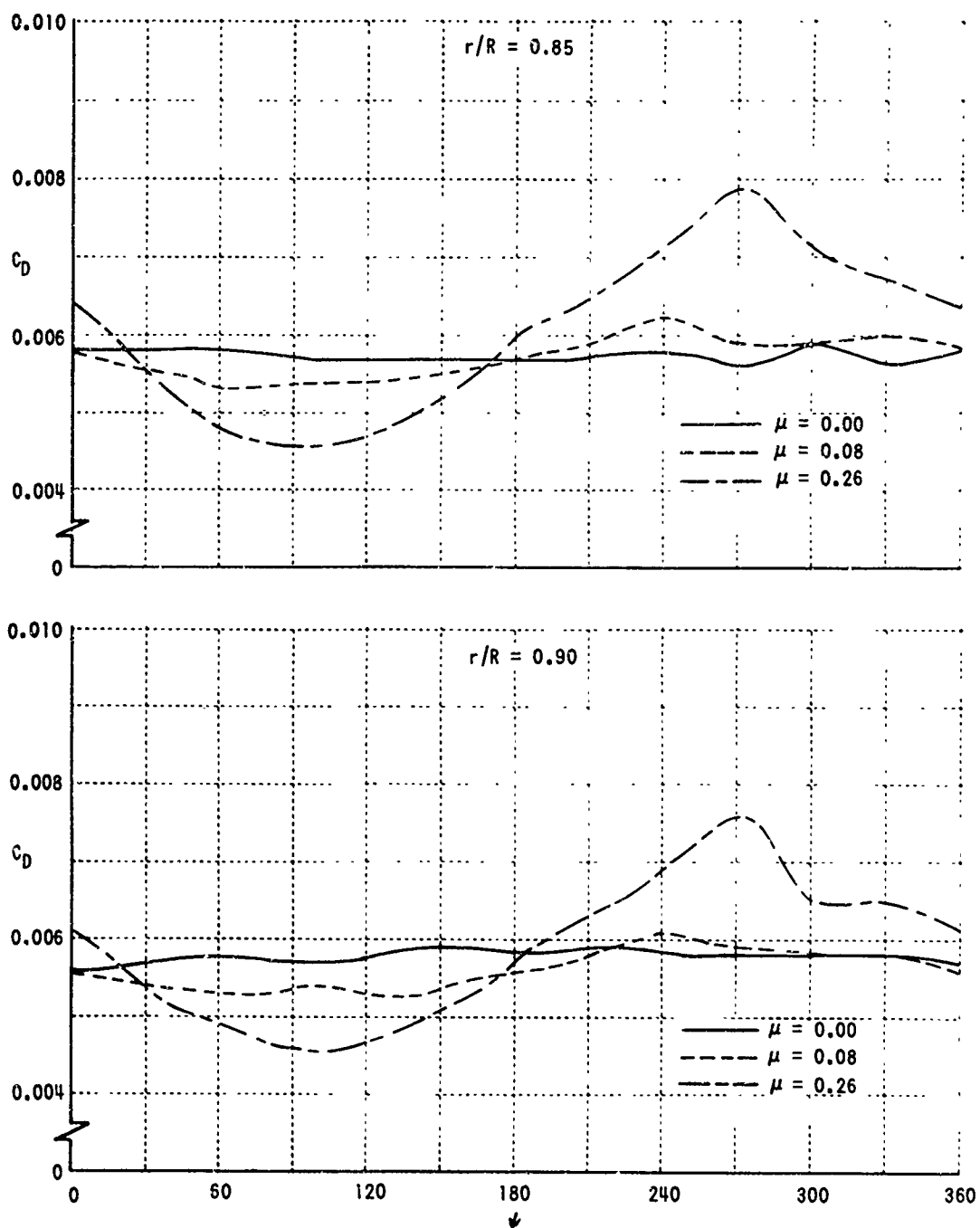


Figure 28. VARIATION OF CALCULATED DRAG COEFFICIENTS WITH AZIMUTHAL ANGLE  $\psi$  FOR UH-1A AT  $r/R = 0.85$  AND  $0.90$  AND  $\mu = 0.00, 0.08$ , AND  $0.26$ .

APPENDIX I  
LEAST-SQUARE POLYNOMIAL APPROXIMATION

If a function  $f(x)$  approximated by the form

$$f(x) = \sum_{k=0}^n a_k \phi_k(x) \quad (29)$$

is to hold over a set of  $N+1$  points  $x_0, x_1, \dots, x_{N+1}$ , where  $N \geq n$ ,  $a_k$  = unknown constants, and  $\phi_k(x)$  = known function of  $x$ , and the sum weighted square error is to be a minimum

$$\sum_{i=0}^N w(x_i) \left[ f(x_i) - \sum_{k=0}^n a_k \phi_k(x_i) \right]^2 = \text{minimum} \quad (30)$$

where  $w(x_i)$  = weighting function at  $x_i$ , ( $w(x_i) = 1$  for all  $i$  if all the data are of equal significance), then the normal equations require that

$$\frac{\partial}{\partial a_r} \left\{ \sum_{i=0}^N w(x_i) \left[ f(x_i) - \sum_{k=0}^n a_k \phi_k(x_i) \right]^2 \right\} = 0,$$

$$\text{or} \quad \sum_{i=0}^N w(x_i) \phi_r(x_i) \left[ f(x_i) - \sum_{k=0}^n a_k \phi_k(x_i) \right] = 0, \quad (31)$$

$$\text{or} \quad a_0 \sum_{i=0}^N w(x_i) \phi_r(x_i) \phi_0(x_i) + a_1 \sum_{i=0}^N w(x_i) \phi_r(x_i) \phi_1(x_i) + \dots +$$

$$a_n \sum_{i=0}^N w(x_i) \phi_r(x_i) \phi_n(x_i) = \sum_{i=0}^N w(x_i) \phi_r(x_i) f(x_i)$$

$$(r = 0, 1, 2, \dots, n)$$

Equation (31) is a set of  $n+1$  linear algebraic equations for  $n+1$  unknowns (i.e.,  $a_0, a_1, \dots, a_n$ ).

Suppose  $w(\chi_i) = 1$ ,  $f(\chi) = \Delta p(\theta)$  with  $\chi = -\frac{1}{2} \cos \theta$ ,  $N+1 =$  total number of pressure measurements, and

$$\sum_{k=0}^n a_k \phi_k(\chi) = A_0 \cot \frac{\theta}{2} + \sum_{k=1}^n A_k \sin k\theta$$

Then Equation (31) is reduced to

$$\sum_{k=0}^n \left[ \sum_{i=1}^N \phi_r(\theta_i) \phi_k(\theta_i) \right] a_k = \sum_{i=1}^N \phi_r(\theta_i) f(\theta_i), \quad (r = 0, 1, 2, \dots, n)$$

or

$$\begin{bmatrix} \sum_{i=0}^N \cot \frac{\theta_i}{2} \cot \frac{\theta_i}{2} & \sum_{i=0}^N \cot \frac{\theta_i}{2} \sin \theta_i & \dots & \sum_{i=0}^N \cot \frac{\theta_i}{2} \sin n \theta_i \\ \sum_{i=0}^N \sin \theta_i \cot \frac{\theta_i}{2} & \sum_{i=0}^N \sin \theta_i \sin \theta_i & \dots & \sum_{i=0}^N \sin \theta_i \sin n \theta_i \\ \sum_{i=0}^N \sin 2 \theta_i \cot \frac{\theta_i}{2} & \sum_{i=0}^N \sin 2 \theta_i \sin \theta_i & \dots & \sum_{i=0}^N \sin 2 \theta_i \sin n \theta_i \\ \vdots & \vdots & \ddots & \vdots \\ \sum_{i=0}^N \sin n \theta_i \cot \frac{\theta_i}{2} & \sum_{i=0}^N \sin n \theta_i \sin \theta_i & \dots & \sum_{i=0}^N \sin n \theta_i \sin n \theta_i \end{bmatrix} \begin{bmatrix} a_0 \\ a_1 \\ a_2 \\ \vdots \\ a_n \end{bmatrix}$$

$$= \begin{bmatrix} \sum_{i=0}^N \cot \frac{\theta_i}{2} f(\theta_i) \\ \sum_{i=0}^N \sin \theta_i f(\theta_i) \\ \sum_{i=0}^N \sin 2 \theta_i f(\theta_i) \\ \vdots \\ \sum_{i=0}^N \sin n \theta_i f(\theta_i) \end{bmatrix}$$

(32)

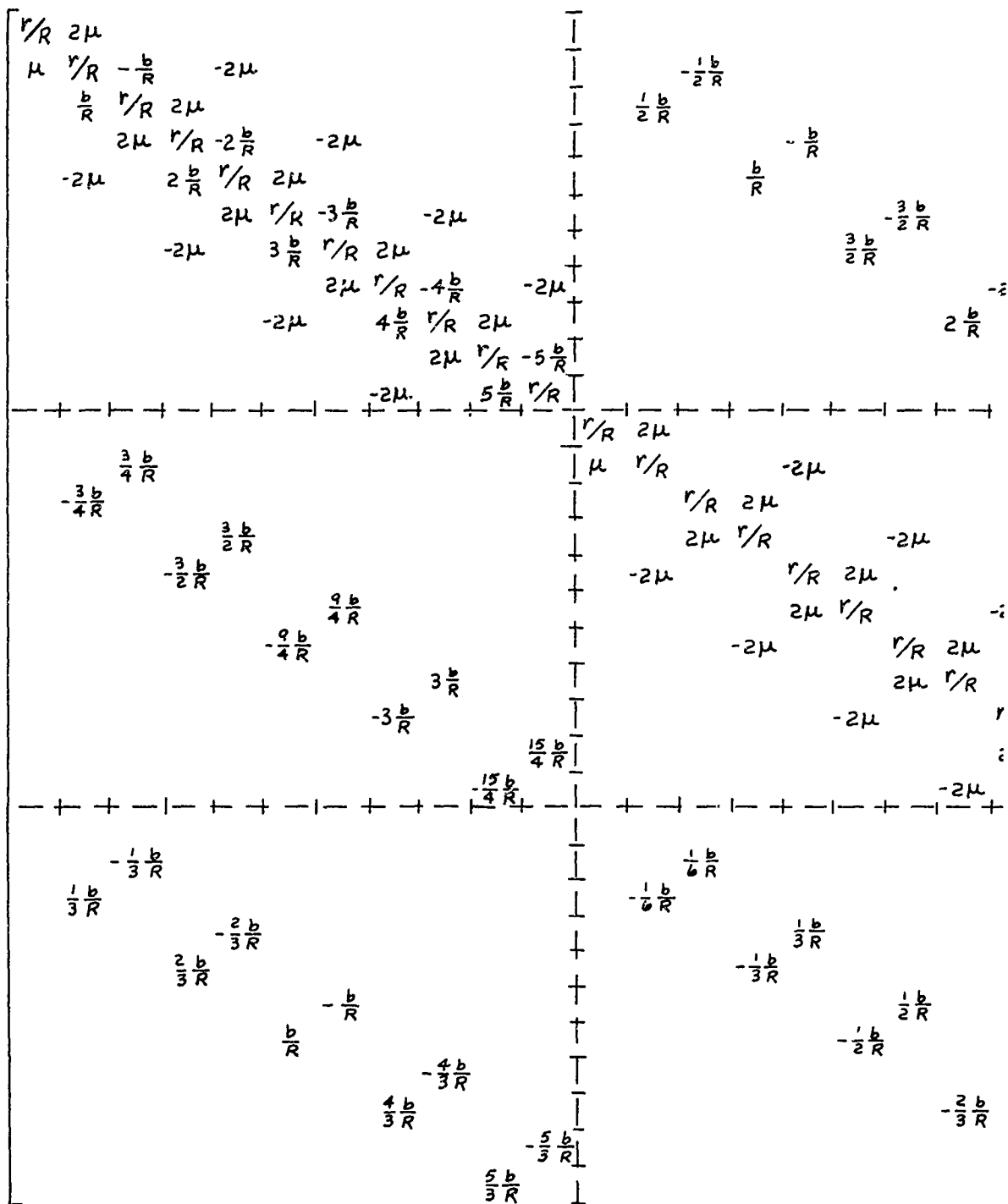
It should be noticed that all the pressure differentials (  $N+1$  pressure taps) are used to provide  $n+1$  Glauert coefficients (  $A_0$  through  $A_n$  ) with  $n \neq N$  . Equation (32) can be solved by the standard sub-routine of the solution of the  $n$  linear simultaneous algebraic equations. Once the  $A_i$  's are calculated, quantities like

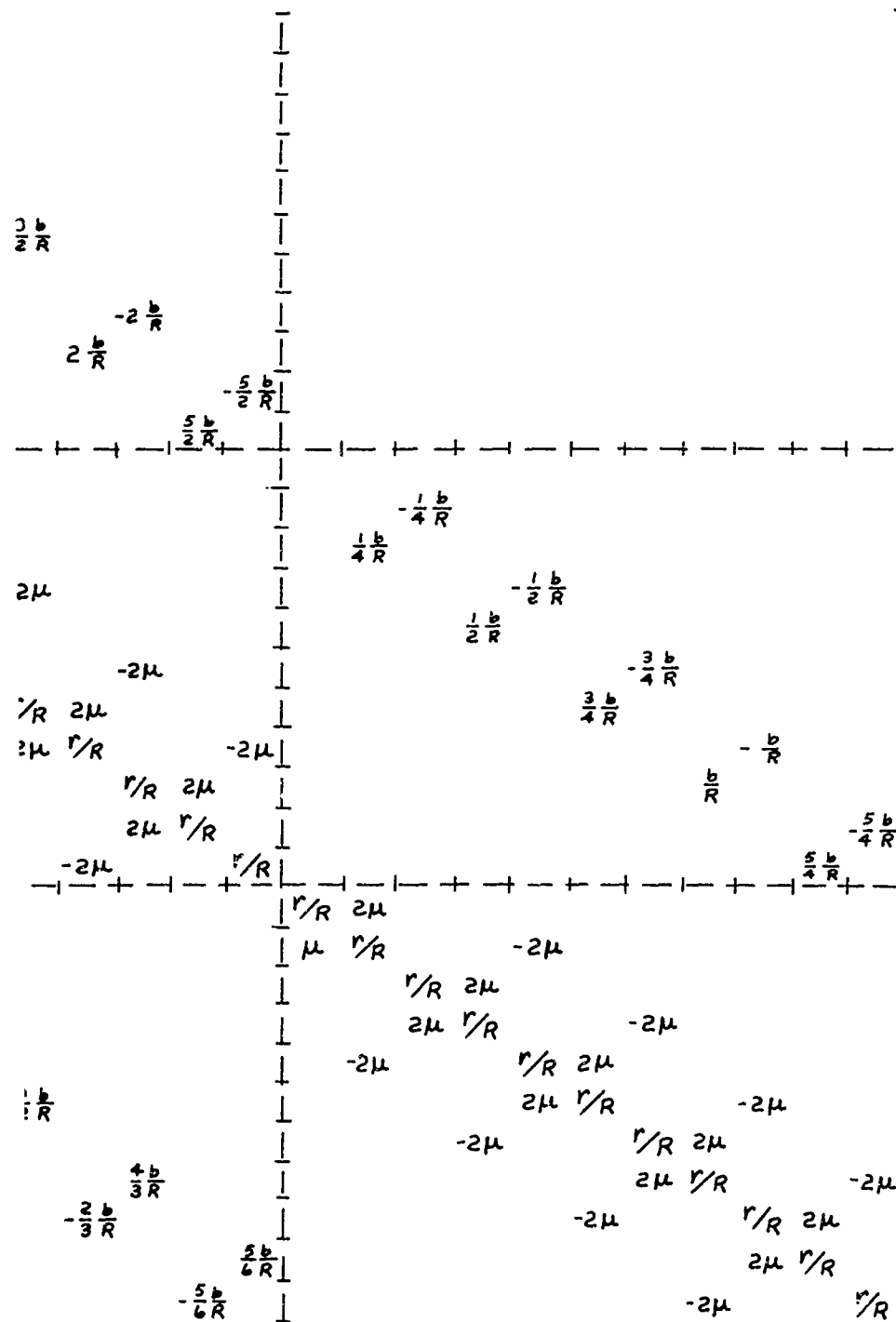
$$\Delta p'(\theta_i) = A_0 \cot \frac{\theta_i}{2} + \sum_{k=1}^n A_k \sin k \theta_i, \quad i = 0, 1, \dots, N, \quad \Delta p' - \Delta p,$$

$$\left| \frac{\Delta p' - \Delta p}{\Delta p} \right|, \quad \text{and} \quad \epsilon = \sqrt{\frac{\sum_{i=0}^N (\Delta p' - \Delta p)^2}{N}}$$

can be obtained as the output of the program.

APPENDIX II  
GOVERNING EQUATIONS FOR A's





$A_1^0$	$\frac{r}{R} C_0^0 + 2\mu C_{11}^1$
$A_{11}^1$	$\frac{r}{R} C_{11}^1 + \mu C_{11}^0 - 2\mu C_{12}^2 + \frac{3b}{R} C_{02}^1$
$A_{12}^1$	$\frac{r}{R} C_{12}^1 + 2\mu C_{11}^2 - \frac{3b}{R} C_{01}^1$
$A_{11}^2$	$\frac{r}{R} C_{11}^2 + 2\mu (C_{12}^1 - C_{12}^3) + \frac{6b}{R} C_{02}^2$
$A_{12}^2$	$\frac{r}{R} C_{12}^2 - 2\mu (C_{11}^1 - C_{11}^3) - \frac{6b}{R} C_{01}^2$
$A_{11}^3$	$\frac{r}{R} C_{11}^3 + 2\mu (C_{12}^2 - C_{12}^4) + \frac{9b}{R} C_{02}^3$
$A_{12}^3$	$\frac{r}{R} C_{12}^3 - 2\mu (C_{11}^2 - C_{11}^4) - \frac{9b}{R} C_{01}^3$
$A_{11}^4$	$\frac{r}{R} C_{11}^4 + 2\mu (C_{12}^3 - C_{12}^5) + \frac{12b}{R} C_{02}^4$
$A_{12}^4$	$\frac{r}{R} C_{12}^4 - 2\mu (C_{11}^3 - C_{11}^5) - \frac{12b}{R} C_{01}^4$
$A_{11}^5$	$\frac{r}{R} C_{11}^5 + 2\mu C_{12}^4 + 15 \frac{b}{R} C_{02}^5$
$A_{12}^5$	$\frac{r}{R} C_{12}^5 - 2\mu C_{11}^4 - 15 \frac{b}{R} C_{01}^5$
$A_2^0$	$\frac{r}{R} C_0^0 + 2\mu C_{21}^1$
$A_{21}^1$	$\frac{r}{R} C_{21}^1 + \mu C_{22}^0 - 2\mu C_{22}^2 - \frac{b}{R} C_{02}^1$
$A_{22}^1$	$\frac{r}{R} C_{22}^1 + 2\mu C_{21}^2 + \frac{b}{R} C_{01}^1$
$A_{21}^2$	$\frac{r}{R} C_{21}^2 + 2\mu (C_{22}^1 - C_{22}^3) - \frac{2b}{R} C_{02}^2$
$A_{22}^2$	$\frac{r}{R} C_{22}^2 - 2\mu (C_{21}^1 - C_{21}^3) + \frac{2b}{R} C_{01}^2$
$A_{21}^3$	$\frac{r}{R} C_{21}^3 + 2\mu (C_{22}^2 - C_{22}^4) - \frac{3b}{R} C_{02}^3$
$A_{22}^3$	$\frac{r}{R} C_{22}^3 - 2\mu (C_{21}^2 - C_{21}^4) + \frac{3b}{R} C_{01}^3$
$A_{21}^4$	$\frac{r}{R} C_{21}^4 + 2\mu (C_{22}^3 - C_{22}^5) - \frac{4b}{R} C_{02}^4$
$A_{22}^4$	$\frac{r}{R} C_{22}^4 - 2\mu (C_{21}^3 - C_{21}^5) + \frac{4b}{R} C_{01}^4$
$A_{21}^5$	$\frac{r}{R} C_{21}^5 + 2\mu C_{22}^4 - \frac{5b}{R} C_{02}^5$
$A_{22}^5$	$\frac{r}{R} C_{22}^5 - 2\mu C_{21}^4 + \frac{5b}{R} C_{01}^5$
$A_3^0$	$\frac{r}{R} C_0^0 + 2\mu C_{31}^1$
$A_{31}^1$	$\frac{r}{R} C_{31}^1 + \mu C_{32}^0 - 2\mu C_{32}^2 + \frac{2}{3} \frac{b}{R} C_{02}^1$
$A_{32}^1$	$\frac{r}{R} C_{32}^1 + 2\mu C_{31}^2 - \frac{2}{3} \frac{b}{R} C_{01}^1$
$A_{31}^2$	$\frac{r}{R} C_{31}^2 + 2\mu (C_{32}^1 - C_{32}^3) + \frac{4}{3} \frac{b}{R} C_{02}^2$
$A_{32}^2$	$\frac{r}{R} C_{32}^2 - 2\mu (C_{31}^1 - C_{31}^3) - \frac{4}{3} \frac{b}{R} C_{01}^2$
$A_{31}^3$	$\frac{r}{R} C_{31}^3 + 2\mu (C_{32}^2 - C_{32}^4) + 2 \frac{b}{R} C_{02}^3$
$A_{32}^3$	$\frac{r}{R} C_{32}^3 - 2\mu (C_{31}^2 - C_{31}^4) - 2 \frac{b}{R} C_{01}^3$
$A_{31}^4$	$\frac{r}{R} C_{31}^4 + 2\mu (C_{32}^3 - C_{32}^5) + \frac{8}{3} \frac{b}{R} C_{02}^4$
$A_{32}^4$	$\frac{r}{R} C_{32}^4 - 2\mu (C_{31}^3 - C_{31}^5) - \frac{8}{3} \frac{b}{R} C_{01}^4$
$A_{31}^5$	$\frac{r}{R} C_{31}^5 + 2\mu C_{32}^4 + \frac{10}{3} \frac{b}{R} C_{02}^5$
$A_{32}^5$	$\frac{r}{R} C_{32}^5 - 2\mu C_{31}^4 - \frac{10}{3} \frac{b}{R} C_{01}^5$



Unclassified

Security Classification

DOCUMENT CONTROL DATA - R & D		
(Security classification of title, body of abstract and indexing annotation must be entered when the overall report is classified)		
1. ORIGINATING ACTIVITY (Corporate author)		2a. REPORT SECURITY CLASSIFICATION
Cornell Aeronautical Laboratory, Inc. Buffalo, New York		Unclassified
		2b. GROUP
3. REPORT TITLE		
ANALYSIS OF MEASURED HELICOPTER ROTOR PRESSURE DISTRIBUTIONS		
4. DESCRIPTIVE NOTES (Type of report and inclusive dates)		
Final Report		
5. AUTHOR(S) (First name, middle initial, last name)		
Chee Tung and Frank A. DuWaldt		
6. REPORT DATE	7a. TOTAL NO. OF PAGES	7b. NO. OF REFS
September 1970	93	13
8a. CONTRACT OR GRANT NO.	8b. ORIGINATOR'S REPORT NUMBER(S)	
DAAJ02-69-C-0076	USAAVLABS Technical Report 70-47	
a. PROJECT NO.	8c. OTHER REPORT NO(S) (Any other numbers that may be assigned this report)	
Task 1F162204A14231	CAL No.	
c.	BB-2803-S-1	
d.		
10. DISTRIBUTION STATEMENT		
This document is subject to special export controls, and each transmittal to foreign governments or foreign nationals may be made only with prior approval of U.S. Army Aviation Materiel Laboratories, Fort Eustis, Virginia 23604.		
11. SUPPLEMENTARY NOTES		12. SPONSORING MILITARY ACTIVITY
		U. S. Army Aviation Materiel Laboratories Fort Eustis, Virginia
13. ABSTRACT		
<p>The purpose of this research was to determine a rational basis for interpretation of the aerodynamic force characteristics of helicopter rotors. The approach consisted of three elements. The first was the parallel development of series expressions for: flight measurements of rotor differential pressure distributions; corresponding two-dimensional wind tunnel pressure distributions for the same airfoil geometry; and theoretical pressure distributions for the two-dimensional airfoil. Second, there was a comparison between pressure differential distribution components determined from flight measurements and pressure distribution components computed by an approximate, unsteady, three-dimensional theory developed previously at CAL for the U. S. Army. Third, the sensitivity of the airfoil drag characteristics to variations in the pressure differential distributions was investigated on the basis of two-dimensional steady boundary layer theory.</p> <p>The fundamental technique employed was a curve-fitting process based on an expansion of the pressure distributions in terms of Glauert coefficients. Glauert coefficients derived from rotor pressure differentials measured in flight had many of the characteristics of the Glauert coefficients derived from measured two-dimensional pressure distributions.</p>		

DD FORM 1473

REPLACES DD FORM 1473, 1 JAN 64, WHICH IS OBSOLETE FOR ARMY USE.

Unclassified

Security Classification

Unclassified

Security Classification

14.	KEY WORDS	LINK A		LINK B		LINK C	
		ROLE	WT	ROLE	WT	ROLE	WT
	Helicopter rotor pressure distributions H-34 helicopter UH-1A helicopter Helicopter rotor unsteady aerodynamics Rotor airloads						

Unclassified

Security Classification